Alma Mater Studiorum – Università di Bologna

DOTTORATO DI RICERCA IN

GEOFISICA

Ciclo XXVII

Settore Concorsuale di afferenza: 04/A4

Settore Scientifico disciplinare: GEO/10

TOWARDS THE 3D ATTENUATION IMAGING OF ACTIVE VOLCANOES: METHODS AND TESTS ON REAL AND SIMULATED DATA

Presentata da: **VINCENZO SERLENGA**

Coordinatore Dottorato **Relatore**

Prof. Michele Dragoni **dott. Salvatore de Lorenzo**

Correlatori

Prof. Aldo Zollo

Dott. Guido Russo

Esame finale anno 2015

"One thing that most seismologist agree upon is that
Q measurements are inherently difficult"
(Brian Mitchell, 2010)

Mitchell, B., 2010b. Epilogue. Pure and Applied Geophysics, 167, 1581; doi: 10.1007/s00024-010-0235-5.

A nonna Titina, zio Michele e nonna Lucia.

CONTENTS

Introduction 1

1 The anelastic attenuation of seismic waves 3

1.1 Introduction 3
1.2 The quality factor 4
1.3 The quality factor physical significance 7
1.4 Frequency dependence of Q and dispersion effect related to anelastic attenuation 11
1.5 Measurements techniques of the quality factor 13
1.5.1 Rise time method 14
1.5.2 The spectral ratio method 17
1.5.3 The spectral decay method 19

2 Data analysis: validation of spectral ratio method through synthetic tests 22

2.1 Introduction 22
2.2 Synthetic tests 25
2.2.1 Sensitivity of the method to V(z) models 27
2.2.2 Sensitivity of the method to the source function 39
2.2.3 Sensitivity of the method to the selected time window 41
2.3 Deconvolution procedure 43
2.3.1 Application of deconvolution procedure 45

3 Data analysis: application of spectral ratio method to an active seismic database 48

3.1 Introduction 48
3.2 The SERAPIS experiment 49
3.3 The analysis of SERAPIS dataset 50
3.3.1 Signal analysis processing. 51
3.3.2 The choice of the reference station. 54
3.3.3 Spectral ratio computation. 55
3.3.4 dt^* measurement selection. 57

4 Tomographic inversion procedure and synthetic tests 60

4.1 Introduction. 60
4.2 Principles of the tomographic problem. 60
4.2.1 The attenuation tomography. 61
4.2.2 Representation of the velocity and attenuation structure and formulation of the attenuation tomographic problem. 63
4.2.3 The formulation of the attenuation tomographic problem for differential attenuation measurements. 65
4.3 The inversion method. 67
4.3.1 Damping and smoothing parameters. 68
4.4 Description of the tomographic procedure. 70
4.5 Validation of the code and of tomographic procedure: synthetic tests. 71

5 The attenuation tomography of Campi Flegrei caldera, Southern Italy 75

5.1 Introduction 75
5.2 The inversion strategy 82
5.2.1 The starting model 83
5.2.2 The grid spacing and regularization parameters 88
5.3 The three dimensional attenuation model 93
5.4 Resolution study 95
5.4.1 DWS, RDE and Spread function 96
5.4.2 Synthetic tests: fixed geometry and checkerboard tests 99
5.5 Discussion and interpretation of results 104

Conclusions 108

References 110

Aknowledgments/Ringraziamenti 124

INTRODUCTION

Among the most interesting and fascinating natural phenomena, certainly we have to include volcanic eruptions. Besides the undeniable appeal of such natural sight, the associated hazard must be considered. The risk does not only depend on the eruptive style of volcanoes, but also on the high exposure due to people living in the proximity of volcanoes. Actually, since ancient times, people choose to live in volcanic areas in order to exploit the agricultural productivity of volcanic soils.

In order to reduce and to manage any natural risk, as for example the volcanic one, scientific community should gain a deep understanding of the concerned phenomenon. In this regard, an in-depth knowledge of the volcanic area and of its deep system is necessary. In particular, a model of the subsurface structure of a volcano and of its magmatic system can facilitate the understanding of physical processes governing its eruptive and pre-eruptive activity.

To this purpose, the most commonly used technique is the seismic travel-time tomography (Chouet, 2003). It allows to obtain an image of the subsurface in terms of elastic properties of the medium.

In the past, a lot of tomographic studies have been carried out in volcanic areas (e.g. Toomey and Foulger, 1989; Benz et al., 1996; Judenherc and Zollo, 2004; Rowlands et al., 2005; Brenguier et al., 2006; Sherburn et al., 2006; Battaglia et al., 2008). However, from a seismological point of view, volcanoes are very complex structures. Actually, the strong heterogeneity in the medium properties can be due to several factors: 1) presence of solidified intrusions; 2) volumes containing molten rocks; 3) hydrothermal areas; 4) geothermally altered rocks; 5) highly fractured rocks; 6) thermal convection phenomena; 7) intricate deposits of different shapes, thicknesses and compositions; 7) volumes rich in gases.

Due to the nature of such strong complexity, in most cases the knowledge of elastic properties like the propagation velocity of P and S waves is not sufficient for a complete description of the medium. In fact, a better characterization of the investigated volcanic area can be achieved by building an attenuation image of the subsurface in terms of 3D variation of the quality factor $\boldsymbol{Q}$ or of its reciprocal value $\boldsymbol{Q^{-1}}$.

Actually, the attenuation of elastic waves is more sensitive than elastic parameters to temperature, porosity, permeability and presence of fractures permeated by aqueous, magmatic or gas fluids. These factors are very important in the physical characterization of the rocks and of the volcanic system.

For this reason, several tomographic works (Evans and Zucca, 1988; Clawson et al., 1989; Ponko and Sanders, 1994; Zucca et al., 1994; Sanders et al., 1995; Sanders and Nixon, 1995; de Lorenzo et al., 2001; De Gori et al., 2005; De Siena et al., 2010) have been done in the past in order to provide an attenuation imaging of different volcanic and geothermal areas around the world. It has been shown that the imaging of the quality factor, in combination with elastic images, is very useful for defining the extension of melt bodies in volcanic areas, too.

In this study the problem of achieving an attenuation imaging in active volcanic areas has been faced. The thesis is organized in five chapters. The first chapter deals with the physics of the anelastic attenuation and the effects of anelasticity on seismic signals. Furthermore a description of most commonly used techniques to retrieve informations on anelastic properties of the propagation medium will be provided. In the second chapter a deep investigation on the accuracy of data measurement technique has been tackled by means of synthetic tests. In particular, the sensitivity of spectral ratio method to three different parameters has been studied: 1) the velocity model; 2) the selected signal time window; 3) the selected frequency range used for the spectral analysis. Furthermore, a refined approach for the application of spectral ratio method has been developed and tested on synthetic data. In the third chapter the application of data measurement technique to a real dataset will be described. The formulation of the inverse problem, the description of the tomographic inversion strategy and characteristics of the tomographic code will be described in the fourth chapter. Moreover, some synthetic tests which have been carried out to validate the tomographic inversion code are described. In the fifth chapter, the application of tomographic inversion procedure to a real dataset, relative to Campi Flegrei caldera, will be described. In particular, the retrieved three dimensional compressional attenuation model will be provided. By means of synthetic tests and the study of resolution matrix and ray coverage in the propagation medium, the quality of retrieved solution will be discussed. Finally a brief interpretation of the tomographic results will be provided.

CHAPTER 1

The anelastic attenuation of seismic waves

1.1 Introduction

If we look at two seismic signals recorded at two different distances, the most clear effect which we could notice is the difference in the amplitudes; the farther is the receiver, the lower is the recorded amplitude.

The decrease in the maximum peak which characterizes the seismic waves during their propagation is caused by the attenuation phenomenon, which can be distinguished into different types.

The most intuitive one is the geometric attenuation, which is related to the geometric expansion of the wave front. For body waves, characterized by a spherical wave front, the amplitude decreases as a function of distance with the relation

$A \propto 1/r$.

Surface waves, instead, characterized by cylindrical wave front, are subjected to an amplitude decrease with the square root of the distance, that is

$A \propto 1/\sqrt{r}$.

Another attenuation mechanism is the scattering, which depends on spatial changes in the physical properties of the medium. If the heterogeneity size is greater than the wavelength, the ray path is distorted by multipathing; the principal effect is the scattering and redistribution in all directions of seismic energy.

Another important factor, which greatly influences the amplitude decrease of seismic waves as a function of the distance, is the anelasticity of the Earth.

The energy driven by elastic waves generated by an earthquake or an artificial source (shots, nuclear explosions, …) is not only spent in elastic deformation processes; as a

matter of fact, part of the kinetic energy is lost to heat by permanent deformation of the medium, both at large and at a smaller scale.

The large-scale, or macroscopic term for this process is represented by internal friction.

Among microscopic mechanisms that may cause the over mentioned energy dissipation, defects in minerals, frictional sliding on crystals, grain boundaries, vibration of dislocations and the flow of hydrous fluids take on an important role.

Since these mechanisms depend on the nature of the materials through which waves propagate, this process is often denoted as "intrinsic attenuation", to distinguish it from the scattering attenuation, which instead depends on the spatial heterogeneities of the medium.

1.2 The quality factor

The seismological parameter which is commonly used to describe the anelastic properties of the Earth is the adimensional **quality factor**. In isotropic dissipative media, Q is a positive, dimensionless, scalar quantity, independent of the direction of the wave propagation.

We can define the quality factor Q(*f*) as a function of frequency in the form:

$$\frac{1}{Q(f)} = -\frac{\Delta E}{2\pi E}. \qquad (1.1)$$

In the previous relation, the term ΔE represents the energy fraction dissipated during a cycle of harmonic motion of frequency f by a wave, because of imperfections in the elasticity of the material in which the signal propagates; the term E, instead, describes the peak strain energy stored in the volume of the material (Udias, 1999).

The quality factor Q is inversely related to the strength of the attenuation: it means that *low-Q* regions are more attenuating than *high-Q* regions.

For this reason, attenuation of seismic waves is often discussed in terms of Q^{-1}. Actually, it has the advantage that its values are directly proportional to the damping. On the other hand, by describing attenuation in terms of Q, the range of variability of Q values better allows to distinguish between high and and low attenuating bodies. To this purpose, based on Q values, McCann et al. (1997) distinguished two types of

propagation medium: Q < 25 identifies a poor propagator whereas Q > 100 a good propagator.

The estimation of the quality factor is a very important issue in the determination of anelastic properties of rocks. Equation 1.1, unfortunately, is rarely of direct use, since only in special experiments it is possible to measure directly the quantities appearing in the formulation 1.1.

Therefore, a different strategy should be used in order to retrieve anelastic information on the propagation medium.

Even if some of the most common methods for inferring Q measurements will be in detail explained in the following, in this paragraph a brief overview on the principle that is commonly adopted for Q estimations will be given.

In experimental seismology, the mathematical relationship between the amplitude of the ground motion recorded by a receiver at a given distance from the source and the quality factor is commonly used. Actually, the spatial decay of amplitude in a propagating wave at a fixed frequency is generally observed (Aki and Richards, 1980).

In a medium with a weak anelasticity, it is possible to suppose that the attenuation effect on a transient signal can be reproduced studying the effect on each frequency component.

Let us consider a monochromatic wave, characterized by only one frequency component.

Wave amplitude is proportional to $E^{1/2}$, that is

$$E \propto A^2 . \tag{1.2}$$

Differentiating (1.2), we have

$$\frac{dE}{dA} = 2A \Rightarrow dE = 2AdA . \tag{1.3}$$

Then, taking into account (1.2),

$$\frac{dE}{E} = \frac{2AdA}{A^2} \Rightarrow \frac{dE}{E} = \frac{2dA}{A} \tag{1.4}$$

and therefore, for finite increments, taking into account the relation between the quality factor and the fraction of energy (1.1):

$$\frac{\Delta E}{E} = \frac{2\Delta A}{A} = -\frac{2\pi}{Q} . \tag{1.5}$$

Finally,

$$\boxed{\frac{\Delta A}{A} = -\frac{\pi}{Q}}. \qquad (1.6)$$

Equation (1.6) describes the amplitude variation of a monochromatic wave in a dissipative medium and, as a consequence, the factor *1/Q* represents the ratio between the decrease in amplitude during one period and the initial amplitude.

As previously said, a way to retrieve estimations of the quality factor Q is to observe the spatial decay of the amplitude as a function of the distance.

To this purpose, a ground amplitude variation law as a function of the distance and of quality factor has to be determined.

First, it is important to underline that the quantity ΔA in relation (1.6) represents the amplitude variation for a wave cycle, that is on a distance equal to λ.

In order to retrieve the amplitude variation $\Delta A(r)$ on a distance Δr, the following relation can be used (taking into account also relation 1.6) :

$$\frac{\Delta A(r)}{\Delta r} \approx \frac{dA}{dR} = \frac{\Delta A}{\lambda} = -\frac{A\pi}{\lambda Q} \Rightarrow \frac{1}{Q} \approx -\frac{1\lambda dA}{\pi A dr} \qquad (1.7)$$

The quantity dA/λ is the amplitude variation of wavelength unity.

From (1.7) it follows that

$$\frac{dA}{A} = -\frac{\pi}{\lambda Q} dr\,. \qquad (1.8)$$

Integrating both members of (1.8), we have

$$\int_{A_0}^{A} \frac{dA}{A} = -\frac{\pi}{Q\lambda} \int_0^r dr\,, \qquad (1.9)$$

where the integration extremes of the integral at the first member, A_0 and A, represents the amplitude at the source and the amplitude at a given distance r from the source, respectively.

Solving the integral (1.9) we have

$$\ln \frac{A}{A_0} = -\frac{\pi r}{Q\lambda} \Rightarrow A = A_0 e^{-\frac{\pi r}{Q\lambda}}. \qquad (1.10)$$

Since $\lambda = \frac{2\pi c}{\omega}$, equation (1.10) can be written as

$$A = A_0 e^{-\frac{\pi r \omega}{Q 2\pi}} \Rightarrow A = A_0 e^{-\frac{\omega t}{2Q}} \quad . \qquad (1.11)$$

In equation (1.11), the term ω is the signal pulsation, the expression $t=r/c$ is the travel time, whereas the velocity propagation of the phase which we are studying is represented by the term c.

Equation (1.11) is very useful in order to understand the main effects of the anelastic attenuation on a seismic signal and the differences respect to the geometric attenuation.

At a fixed pulsation ω and quality factor Q, the signal amplitude decrease is governed by an exponential law: for this reason, at greater distances the anelastic attenuation effect is prevalent on the geometric attenuation effect.

An important element characterizing the anelastic attenuation phenomenon and clearly visible from (1.11) is the presence of a frequency dependent term which is responsible of the dispersion effect caused on seismic signals because of anelastic attenuation phenomenon.

Moreover, at a fixed distance and quality factor value, high frequencies are more attenuated than lower frequencies.

All these properties are really important in the seismic signals interpretation and analysis oriented to a better understanding of anelastic properties of the propagating medium (Zollo and Emolo, 2010).

1.3 The Quality Factor physical significance

Most of the physical mechanisms that have been proposed to explain intrinsic attenuation (grain boundaries processes, crystal defects sliding, fluid-filled cracks) can be parameterized in terms of standard linear solid: it is a simple viscoelastic model which has intermediate properties between those of elastic and viscous bodies.

It can be understood in terms of one-dimensional mechanical models consisting in the combination of spring and dashpots (either a Maxwellian Body or a Kelvin-Voigt body: in the former the spring and dashpot are mounted in series, in the latter they are mounted in parallel (figure 1.1)). The spring describes the elastic properties of the medium, whereas the dashpot represents the viscous element.

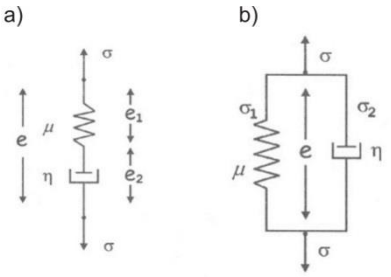

***Figure 1.1**: A combination of a spring and dashpots to represent viscoelastic bodies; a) Maxwell body, b) Kelvin – Voigt body (After Udias, 1999).*

In order to better understand the response of an anelastic body to the application of a stress (for example due to the passage of a seismic wave inside the crust), the behaviour of both a Maxwellian body and a Kelvin-Voigt body will be described.

At the beginning, let us consider a Maxwellian body.

It is well known that in an elastic body, the stress σ and the strain ε are related by:

$$\sigma = \mu\varepsilon, \tag{1.11}$$

where the term μ represents the elasticity coefficients of the spring.

In a viscous body, the relation between stress and strain is

$$\sigma = \eta\frac{de}{dt} = \eta\dot{e}; \tag{1.12}$$

the term η is the viscosity coefficient.

Therefore, if a stress σ is applied in a Maxwellian Body, the two elements respond with two different deformations:

$$\sigma = \mu e_1, \tag{1.13}$$

$$\sigma = \eta\frac{de_2}{dt} = \eta\dot{e}_2. \tag{1.14}$$

The total deformation of the system is $e = e_1 + e_2$, and its strain rate is given by:

$$\dot{e} = \frac{\dot{\sigma}}{\mu} + \frac{\sigma}{\eta}. \tag{1.19}$$

Let us apply an harmonic stress

$$\sigma = \sigma_0 sen(ft) \tag{1.20}$$

to a Maxwellian body. In the above expression, the term *f* represents the frequency of the harmonic stress.

By substituting equation (1.20) into (1.19) and integrating in a time interval [0-t],

$$e(t) = \frac{f\sigma_0}{\mu}\int_0^t \cos(ft)dt + \frac{\sigma_0}{\eta}\int_0^t sen(ft)dt \Rightarrow$$

$$\Rightarrow e(t) = \frac{\sigma_0}{\mu} sen(ft) - \frac{\sigma_0}{\eta f}[\cos(ft) - 1] \Rightarrow$$

$$\Rightarrow e(t) = \frac{\sigma_0}{\mu}\left[sen(ft) - \frac{\mu}{\eta f}\cos\ ft + \frac{\mu}{\eta f}\right].$$

Let us consider that $\tan\left[\arctan\left(\frac{\mu}{\eta f}\right)\right] = \frac{\mu}{\eta f}$ and let us introduce $\theta = \arctan\frac{\mu}{\eta f}$.

Then, it follows:

$$e(t) = \frac{\sigma_0}{\mu}\left[\frac{sen(ft-\theta)}{\cos\theta} + \frac{\mu}{\eta f}\right].$$

Since $\frac{1}{\cos\theta} = \sqrt{1+\left(\frac{\mu}{\eta f}\right)^2}$,

$$e(t) = \frac{\sigma_0}{\mu}[sen(ft-\theta)]\sqrt{1+\left(\frac{\mu}{\eta f}\right)^2} + \frac{\mu}{\eta f}. \qquad (1.21)$$

In the case of a perfect elastic body, the response, instead, is:

$$e(t) = \frac{\sigma_0}{\mu} sen(ft). \qquad (1.22)$$

Comparison of (1.21) and (1.22) reveals that the main difference between the two responses consists in the presence of the factor $\frac{\mu}{\eta f}$ that can be defined as $\frac{1}{Q}$.

Therefore, equation (1.22) changes into

$$\boxed{e(t) = \frac{\sigma_0}{\mu}\left[sen(ft-\theta)\sqrt{1+\left(\frac{1}{Q^2}\right)} + \frac{1}{Q}\right]}. \qquad (1.23)$$

Then, the factor *1/Q*, where the term *Q* is the quality factor previously defined, represents how much the response of a Maxwellian body differs from that of a perfectly elastic one. In particular, it is possible to observe that the presence of an attenuating term represented by the factor *1/Q* not only modifies the amplitude of the deformation response, but also introduces a phase shift between the application of the stress and the resulting deformation (Udias, 1999).

However, as previously said, the effect of anelasticity of the Earth can be better described considering a damped harmonic motion applied to a Kelvin – Voigt body.

Then, let us suppose to apply a force $F=ma$ on a mass m suspended by a spring of elastic coefficient μ, with a dissipating element of viscosity η mounted in parallel, as for Kelvin-Voigt body configuration.

The displacement of the mass, therefore, is not simply proportional to the applied force, since also a friction force proportional to the velocity of the system has to be taken into account.

Then, the resulting equation which describes equation of the motion is:

$$m\frac{d^2u(t)}{dt^2}+\eta\frac{du(t)}{dt}+\mu u(t)=0\,, \tag{1.24}$$

where the term u is the displacement, the second addend describes the dissipation produced by the dashpot, whereas the third addend the restoring force of the spring.

Representing the damping effect caused by the dashpot with the coefficient $Q=\eta/(mf_0)$ and dividing by m both members of (1.24), above equation changes into

$$\frac{d^2u(t)}{dt^2}+\frac{f_0}{Q}\frac{du(t)}{dt}+f_0^2u(t)=0 \qquad . \tag{1.25}$$

The term f_0 represents the natural frequency at which the mass would move back and forth in an undamped oscillation.

The solution of (1.25) for the damped harmonic motion, representing the response of a damped system to an impulse at time zero, is:

$$u(t)=A_0e^{-\frac{f_0t}{2Q}}\cos ft \tag{1.26}$$

and it clearly differs from that one of a frictionless system represented by

$$u(t)=A_0\cos f_0t\,. \tag{1.27}$$

Moreover, the frequency term in the equation (1.26) is related to the natural frequency f_0 of the undamped system through the relation

$$f=f_0\sqrt{\left(1-\frac{1}{4Q^2}\right)}\,. \tag{1.28}$$

Two main differences emerge by comparing (1.26) and (1.27) and by considering relation 1.28:

1) The exponential term describes the decay of the signal envelope, which is superimposed on the harmonic oscillation given by cosine term;
2) the frequency of the harmonic oscillation is changed from the natural one by an amount depending on the quality factor: the lower the Q value is, the greater the frequency change is from its undamped value.

The time at which the amplitude decays to 1/e of its original value is called relaxation time, and it is expressed by

$$t_{1/e} = 2Q / f_0 \tag{1.29}$$

(Stein and Wysession, 2003; Shearer 2009).

1.4 Frequency dependence of Q and dispersion effect related to anelastic attenuation

Since 1914, with the pioneering study by Lindsay, the dependency of the quality factor on the frequency has been analysed and debated by the seismological community.

Since that time, there have been a significant number of laboratory experiments on different types of materials (both metals and rocks) which have tried to give a shared answer to this issue (Birch, 1942; Zemanek and Rudnik, 1961, Peselnick and Outerbridge, 1961).

In particular, Knopoff (1964) concluded that the quality factor varies as first power of frequency in liquids, whereas it is substantially independent of frequency in solids, especially in the frequency range of seismic waves (10^{-3}-100 Hz).

Recently, Morozov has published a lot of papers (Morozov, 2008; Morozov et al., 2008; Morozov, 2009; Morozov, 2010) in which he concludes that there is no reason for which to think to a Q dependent on frequency. In particular he argues that the Q frequency dependence is, in fact, a distorted representation of geometrical attenuation effects, which are not completely described by the geometrical-spreading law $|r|^{-\nu}$ or by other simplified models. These conclusions have met with significant criticism (e.g. Xie and Fehler, 2009; Xie, 2010) to the extent that a special forum has been led in Pure and Applied Geophysics (Mitchell, 2010a; Mitchell, 2010b).

However, the theory gives a very clear answer to this issue, taking into account also the phenomenon of physical dispersions of seismic waves as a consequence of the anelastic

attenuation. Theory suggests that in order to follow causality principle, a dispersive behaviour both of quality factor and of phase velocity of the wave must be taken into account.

A better understanding of this concept can be achieved studying and describing what happens to a delta function propagating through a homogeneous anelastic medium with intrinsic velocity c and Q independent on frequency (fig.1.2).

As previously explained, the attenuation both cause an amplitude reducing on the signal and it acts as a low pass filter, preferentially removing high frequencies.

Through a Fourier analysis involving the attenuation spectrum and the delta function spectrum, we can obtain that at a given distance x, the resulting signal has been modified from the original one and can be expressed by (Aki and Richards, 1980)

$$u(x,t) = \frac{1}{\pi} \frac{\frac{x}{2cQ}}{\left[\left(\frac{x}{2cQ} \right)^2 + \left(\frac{x}{c} - t \right)^2 \right]} \quad . \tag{1.30}$$

Previous equation has been obtained by considering the complete absence of the dispersion and a quality factor independent of frequency.

As it can be seen on figure 1.2, the broadening of the pulse because of the removal of high frequencies cause the signal to arrive at a time instant before x/c, violating the causality principle.

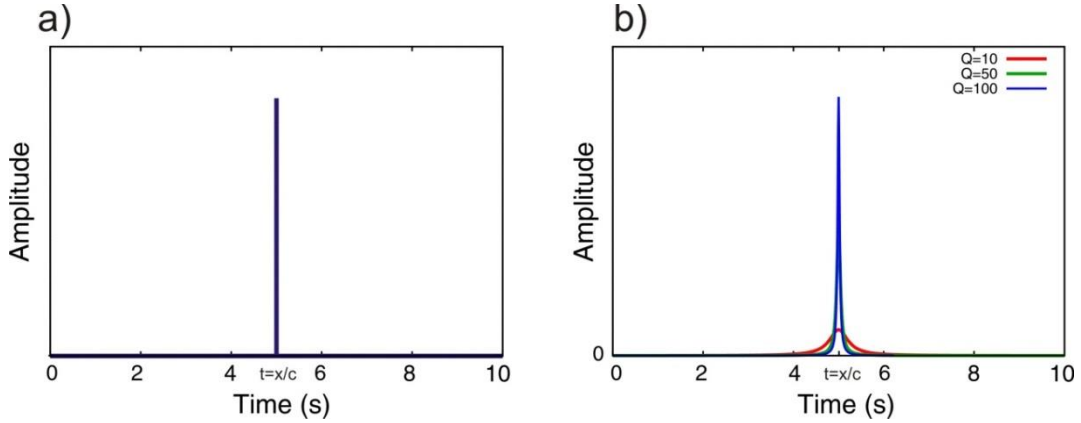

Figure 1.2: a) *A propagating wave pulse composed of a delta function. With no dispersion, all frequencies arrive at the same time.* ***b)*** *"The delta function after broadening by attenuation, showing that energy arrives before the high-frequency arrival time" (cfr. Stein and Wysession, 2003). The different colors refer to different values of quality factor. The lower the Q value is, the lower the amplitude peak is and the greater the pulse broadening is.*

Thus, the physical mechanisms that cause attenuation in the earth must prevent all frequencies to travel at the same velocity. Therefore, in order to follow causality principle, it is necessary that lower frequencies travel at lower speed than both the intrinsic velocity of the medium and higher frequencies.

In particular, this phenomenon acts on the phase velocity of a seismic wave instead that on the group velocity.

The law which describes the phase velocity and its dispersion relation as a function of frequency is the Azimi's attenuation law (Azimi et al., 1968) :

$$c(f) = c_0\left[1+\frac{1}{\pi Q}\ln\left(\frac{f}{f_0}\right)\right] \quad . \tag{1.31}$$

In the above equation, the term c_0 is a reference velocity corresponding to a reference frequency f_0, which, for example is the Nyquist frequency.

The equation (1.31), in its formulation, suggests two similar conclusions, depending on the frequencies values that we are considering:

- at very low frequencies, the logarithmic function has very high negative values: it cause a negative value of *c(f)*, too;
- at very high frequencies ($f \to \infty$), the logarithmic function has very high values: it means that *c(f)* tends to an infinite value.

Considering the unreliability of *c(f)* values in these two extreme conditions, a *Q* dependent on frequency has to be theoretically considered.

This final consideration is in contrast with the laboratories evidences previously mentioned; for this reason, based on different study cases, a preliminary analysis on which is the best model to be adopted (Q dependent on frequency *vs* Q independent of frequency) should be carried out before doing any type of considerations (e.g. de Lorenzo et al., 2010, Zollo et al., 2014).

1.5 Measurement techniques of the Quality factor

Since geophysicists have become increasingly interested in the anelastic properties of rocks, several methods have been developed to compute the quality factor from the analysis of the seismic signals.

Generally, attenuation properties of the medium are measured indirectly, taking advantage of the strong amplitude variations above described.

In particular, Q estimations methods can be divided in two types: time domain analysis and frequency domain analysis methods.

Most of this techniques give information on the quality factor through the measurement of seismological parameter t^* (or through a differential estimation of it): it is defined, in some way, as accumulated Q^{-1} along the ray path and it is mathematically described as

$$t^* = \int_{ray} \frac{ds}{Q(s)V(s)} \tag{1.32}$$

where the term *ds* is a ray path element whereas *Q(s)* and *V(s)* represent the quality factor and the velocity along the ray path, respectively.

In next paragraphs, the principles of some of the most used methods for Q measurements will be described; in particular, the rise time method, the spectral ratio method and the spectral decay method will be discussed.

1.5.1 Rise time method.

The rise time method is a time domain technique, and its theoretical background was derived by Kjartansson (1979). Its application for retrieving Q estimates is based on the broadening effect produced by anelastic attenuation on the seismic signals as a function of the distance.

Different definitions of rise time τ have been proposed in the literature. Gladwin and Stacey (1974), for example, defined it as the maximum amplitude divided by the maximum slope on the seismogram. Zollo and de Lorenzo (2001), on the other side, define the rise time in a velocity signal as the interval between the arrival time and the first zero crossing time (fig.1.3).

Irrespective of definition, the rise time value is expected to increase with the distance travelled by the wave; in particular, Kjartansson demonstrated that, when considering the propagation of a pulse of a Dirac's delta throughout an anelastic medium characterized by an exactly constant *Q*, the relation between τ and t^* is completely linear:

$$\tau = \tau_0 + C(Q)t^*. \tag{1.33}$$

In the above equation, τ_0 is the rise time at the source, whereas the slope *C(Q)*, is a function of *Q*. About this term, a lot of studies have been carried out in the past: Gladwin and Stacey (1974) have experimentally found a constant value of *C* to be equal to 0.5.

Blair and Spathis, (1982), on the other hand, for Q>30 have found different *C* values depending on the type of records: in particular values of 0.485, 0.298 and 0.217 for displacement, velocity and acceleration records have been found, respectively; de Lorenzo (1998), furthermore, in accordance with Blair and Spathis (1998) conclusions, suggested the *C* dependency on the shape of the source time function. In particular de Lorenzo (1998) demonstrated that the linearity between τ and t^* remains only at a corner frequency of the source greater than 10 Hz. In all other case, the dependence of *C(Q)* on source spectrum implies that the classical rise time method can lead to biased estimates of attenuation when applied to earthquake data.

The greater advantage of this method is that, with respect to spectral techniques, it is not affected by subjective windowing criteria; furthermore, because the method is principally based on the observation of the first pulse broadening in the signal, it allows to discard the secondary contributions coming from heterogeneities inside the propagation medium.

On the other hand, "the greatest limit of the technique is that it completely neglects the directivity effect of the seismic radiation generated by a finite dimensional seismic source" (cfr. Tselentis, 2011). However, Zollo and de Lorenzo (2001) proposed in this case a method to deal with the nonlinearity between the rise time and the travel time and to account for directivity of the seismic source. In the case of an active seismic source, obviously, the directivity effect can be neglected. Furthermore, spectral ratio method can be susceptible to bias from noise, so that only high S/N ratio traces can be considered in the analyses.

By means of this method, an estimation of Q in the approximation of an homogeneous medium can be retrieved.

To this purpose, the relation (1.33) has to be considered; in particular, the rise time measurements (τ) on seismic signals contain the undesired source term, which is totally independent of the anelastic attenuation.

For this reason, for each event the different source contribution has to be removed from rise time measurements.

This can be achieved by fitting, for any individual event, the distribution of measured rise times as a function of the travel time *T*: the point where the best fit line intersects with the rise-time axes is τ_0, that is the rise time at the source (fig. 1.4 c). This retrieved value has to be subtracted from the measured rise times, obtaining the so called "reduced rise time" (Tselentis et al., 2010).

In this way, a common distribution of rise time measurements as a function of travel time is obtained, including all the analysed events (fig. 1.4 b). By fitting the distribution and by assuming the term *C(Q)* as a constant, the slope of the best fit line will directly give a first estimation of the mean value of the quality factor in the propagation medium.

This method has been widely used in literature for attenuation tomography works (e.g. Zucca et al., 1994; de Lorenzo et al., 2001; Tselentis et al., 2010).

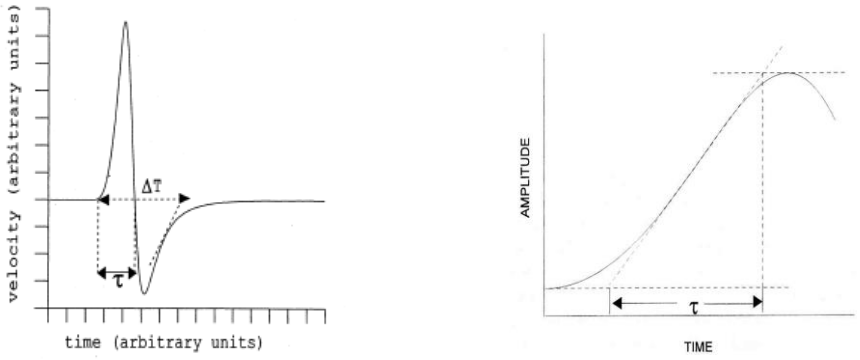

Figure 1.3. Left: *Rise time as defined and measured by Zollo and de Lorenzo (2001) in velocity seismograms (after Zollo and de Lorenzo, 2001) .* ***Right:*** *Rise time definition by Gladwin and Stacey (1974) (after de Lorenzo, 1998).*

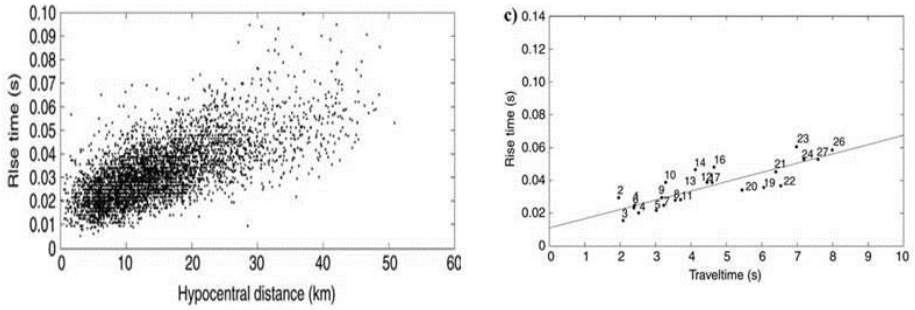

Figure 1.4. Left: *Increasing rise with hypocenter distance.* ***Right***: *Plot of measured rise times for a selected event in order to estimate* τ_0 *(after Tselentis et al., 2011).*

1.5.2 The Spectral ratio method

The spectral ratio method was originally proposed and formulated by Teng in the 1968; Teng (1968) studied the variations of the quality factor in the deeper part of the mantle analysing earthquake data.

An observed P wave amplitude spectrum can be expressed as the product of a source function $S(f,\theta,\phi)$ with a number of transfer function each for an appropriate portion of the transmitting medium.

$$A(f) = S(f,\theta,\phi)C(f)G(t)I(f)\exp(-\pi f t^*), \quad (1.34)$$

where the site effects are accounted by *C(f)*, the path geometrical spreading is represented by *G(t)*, whereas the instrumental response by *I(f)*.

The anelastic attenuation effect is represented by the exponential term $\exp(-\pi f t^*)$.

Before facing in detail the principles of the method, two basic assumptions necessary for its application when considering earthquake sources must be underlined:

1) the normalized source spectrum is not a function of spatial coordinates;
2) the attenuation function can be expressed in terms of a frequency-independent Q over the frequency band by the exponential quantity $\exp(-\pi f t^*)$.

According to the first assumption, the source term $S(f,\theta,\phi)$ can be separated in two terms, a spatial and a temporal part, giving the expression

$$S(f,\theta,\phi) = S_t(f)S_s(\theta,\phi). \quad (1.35).$$

Among all the terms appearing in the (1.34), only the exponential quantity has to be considered in attenuation studies.

The spectral ratio method allows very easily to overcome the common problem of ignoring and removing the contributions of factors different from the one we are interested to, as the source effect and the instrumental response. This is achieved by the computation of the ratio of the amplitude spectra recorded by two receivers located at different distances, x_2 and x_1, from the source. (fig. 1.5).

The station respect to which the spectral ratio is computed is the so called *reference station*. Its choice can be arbitrary, but sometimes closest station to the source can be chosen as reference receiver: it would allow to neglect the attenuation contribution and to consider the respective signal as an approximate representation of the source signal.

Fig. 1.5: *Simple scheme of source-stations configuration for the application of spectral ratio method.*

Then, taking the spectral ratio with respect to the reference receiver, station 1, at the distance $x_{1,}$:

$$\frac{A_i(f,x_2)}{A_j(f,x_1)} = \frac{S_t(f)S_s^2(\theta,\phi)C(f,x_2)G(t,x_2)I(f)\exp\left(-\pi t_2^* f\right)}{S_t(f)S_s^1(\theta,\phi)C(f,x_1)G(t,x_1)I(f)\exp\left(-\pi t_1^* f\right)}. \tag{1.36}$$

It is evident that for a common shot gather with an explosive source and with stations using the same type of instrument (that is the same response curve), quantities $S_t(f)$ and I(f) for both spectral signals cancel out.

By making the assumption that site responses at the two different receivers are equal, $C(f,x_1)$ and $C(f,x_2)$ in (1.36) approximately cancel out, and the equation will take the form

$$\frac{A(f,x_2)}{A(f,x_1)} = \frac{G(x_2)S_s^2(\theta,\phi)\exp\left(-\pi t_2^* f\right)}{G(x_1)S_s^1(\theta,\phi)\exp\left(-\pi t_1^* f\right)}. \tag{1.37}$$

Taking the logarithm of the equation (1.37), we can deduce the expression

$$\ln\frac{A(f,x_2)}{A(f,x_1)} = \ln\frac{G(x_2)S_s^2(\theta,\phi)}{G(x_1)S_s^1(\theta,\phi)} - \pi f\left(t_2^* - t_1^*\right), \tag{1.38}$$

with a linear slope *c* equal to $\pi f(t^*_2 - t^*_1)$ (Matheney and Nowack, 1995). It is retrieved by fitting in the sense of least-squares method the logarithm of the spectral amplitude ratio. The term $(t^*_2 - t^*_1)$ is called *differential attenuation term* and contains the whole information concerning the difference of wave attenuation along two different rays.

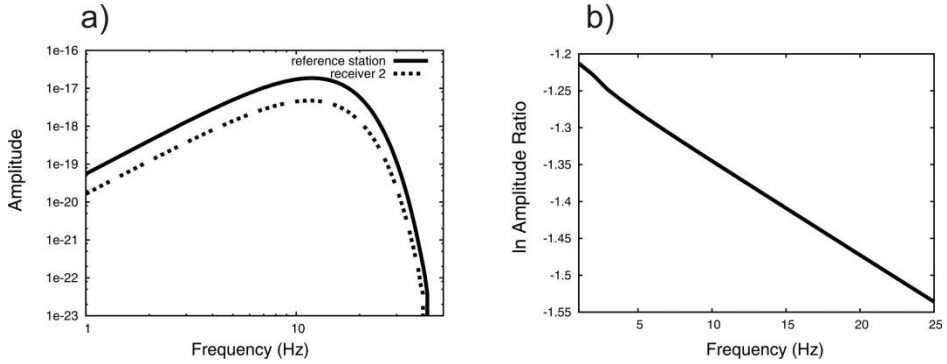

Figure 1.6 *Example of the application of spectral ratio technique on synthetic signals produced in an homogeneous model, both in elastic and anelastic properties.*
a) *Amplitude spectra recorded at two different distances from a point source located at a depth of 3 km; dashed line: farther receiver; solid line: reference station.* ***b)*** *Spectral ratio computed between the two amplitude spectra represented in figure* ***a)****. The computed spectral ratio is perfectly linear, because of absence of noise in synthetic signals and homogeneous elastic and anelastic properties.*

1.5.3 The spectral decay method

The spectral decay method theory is based on the description of the displacement spectra already presented in equation (1.34).

In particular, this measurement technique is based also on the a priori knowledge of the source function. Source theories for earthquakes predict a spectral shape similar to that given by the theories for explosions: a constant long period level, $\Omega_{0,}$ (proportional to the seismic moment M_0), followed by a decay above the corner frequency f_c. Generally the decay is described by an exponential function f^{-n}, where n is a value between 2 and 3 and is defined as high frequency spectral fall-off parameter (Cormier, 1982). Mathematically, the temporal part of the source spectrum is defined as

$$S_t(f) = \frac{\Omega_0}{1+\left(\frac{f}{f_c}\right)^n} . \qquad (1.37)$$

One of the greatest problems in estimating anelastic attenuation properties from earthquake spectra is the existing trade-off between Q measurements and source parameters (in particular the corner frequency and the high frequency spectral fall off).

In fact, Q affects the spectral shape at frequencies smaller than the corner frequency, whereas at frequencies higher than the corner frequency both n and Q control the spectrum (Zollo et al., 2014).

It means that at frequencies higher than the corner frequency the decay will be proportional to f^{-n} times the exponential factor $\exp\left(-\pi t^{*} f\right)$ describing the anelastic attenuation.

However, for low magnitude earthquakes ($M_L \leq 1$) the corner frequency is shifted toward highest frequency values: it means that, in presence of anelastic attenuation, low frequencies should show a spectral decay proportional to anelastic properties of the medium (together with the contribution of site effect and instrumental response).

By removing these undesired contribution (actually, regarding the site effect, this procedure is not so trivial (cfr. de Lorenzo et al., 2010)), and computing the natural logarithm of the amplitude spectrum we have

$$\ln A_{ij}(f) = \ln k - \frac{\pi t}{Q} f \,, \tag{1.38}$$

where the indexes *i* and *j* represent the source and the receiver indexes, respectively.

From (1.38), the slope of the best fit line of the logarithm of the amplitude spectrum in an established frequency range is proportional to the quantity t^{*} (Wittlinger et al., 1983).

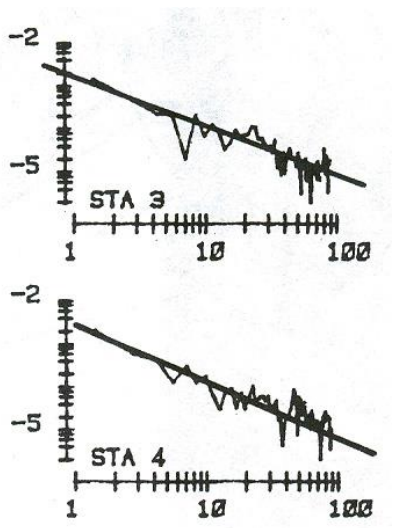

Figure 1.7 *An example of the application of spectral decay method in order to retrieve t* measurements. The slope of the linear trend gives a rough idea of the attenuation influence (after Wittlinger et al, 1983).*

A similar approach can be followed in the case of a point explosive source, whose spectrum can be assimilated to the Dirac function's one.

On the other hand, for earthquakes of magnitude greater than 1, the corner frequency is shifted toward lower frequencies. It means that it is not possible to retrieve so easily the

t* parameter without taking into account the existing trade-off between Q and source parameters. Different techniques have been developed in the past year; they, in particular, consist in iterative procedures in which, at different steps, different inversion parameters (f_c, Ω_0, t^*) are retrieved (Edwards et al., 2008; Zollo et al., 2014).

CHAPTER 2

Data analysis: validation of spectral ratio method through synthetic tests.

2.1 Introduction

As described in the previous chapter, different techniques for estimating anelastic properties have been developed and used in literature in order to obtain attenuation images of the Earth.

In my PhD thesis, the spectral ratio method has been used and its applicability to our purposes has been tested.

This method has been chosen because source contribution and the instrumental response may be removed from the amplitude spectra of the signal. In spite of this advantage, spectral ratio method has met with lot of criticisms because of its instability.

The first aspect which causes the method to be instable is common to all spectral methods: the necessity to isolate a proper time window.

In fact, in order to retrieve informations on the anelastic effect on an established seismic phase (P or S wave), the respective portion of signal has to be isolated from the seismic trace.

Actually, the risk to include other phases than the one we are interested to must be avoided. Sometimes, these complications may be due to the presence of multiple arrivals after the phase we are looking at. As the seismic waves spread away from the source, the different component of the wavefields interact with crustal structure in a variety of ways. These interactions may lead to quite complex behavior, causing elongated wavetrains and complexities in the waveforms. These signal features can be originated by different factors: 1) the scattering produced by heterogeneities in the propagation medium; 2) the thin layering generating multiple reflections and converted phases at shallow depths; 3) a strong velocity gradient. The selection of the proper time window is, therefore, an important issue. In fact, a short time window generally allows

to remove and to neglect all the secondary arrivals. Clearly, the selected time window has to start from the arrival time of the phase whose spectrum has to be computed. On the other hand, a too short time window determines a low resolution at low frequencies and a low spectral resolution. This is reflected in few points over which to fit the spectral ratio. In these conditions it has been seen that the resulting spectral ratio becomes highly variable (Goldberg et al., 1984; Sams and Goldberg, 1990), having a trend far from a linear trend. Sams and Goldberg (1990), furthermore, confirmed the results of Ingram et al., (1985): they found that errors introduced by windowing are minimized when the window duration is long. White (1992), furthermore, showed that the variance in differential measurements by spectral ratios method is inversely proportional to the time window length used in the spectral amplitude computation.

Obviously, the best compromise between duration of the time window and spectral resolution must be found. Actually, too long time windows more likely will contain seismic phases different from the interest one.

Matheney and Nowack (1995) faced the problem of the choice of a proper time window by selecting a variable window length. In particular, they chose a duration equal to three times the first arrival time to envelope peak. This selection criterion was tested both on spectral ratio method and on instantaneous frequency matching method. It was demonstrated that this procedure is able to effectively isolate the first arrival without selecting a too short time window which makes unstable the spectral ratio.

An intrinsic problem linked to the windowing has to be considered, too: the selection of a portion of the signal is obtained by the product of a box function for the seismic trace. In the frequency domain, this operation corresponds to the convolution of the seismic signal FFT with a sinc function. The effects of this mathematical computation introduces nodes and peaks in the windowed spectra. However, the main concept is that by computing the ratio, the effects produced by the convolution with a sinc function at both the spectra do not cancel out. This aspect, unavoidably, introduces further complications and irregularities in the resulting spectral ratio which may only be damped by applying a smoothing procedure to spectra.

Another element renders difficult Q measurements through spectral ratio technique. Actually, in spectral ratio method attenuation measurements are conducted using seismic amplitudes: for this reason noise disturbances have to be taken into account in the analysis of the signal.

Furthermore, seismic amplitudes are strongly affected by the Earth's complex velocity structures and by other factors: among them, the free surface effects on the wave field may be mentioned. Generally, these elements are not taken into account in the modelization of the amplitude spectrum. Actually, the path effect is usually simply described as the product of the geometrical spreading with the attenuation factor. The geometrical divergence is commonly described in the very simple exponential formulation $|r|^{-\nu}$. In the previous formula the distance is expressed by r and the term ν is a factor depending on the wave type (ν=0.5 and ν=1 for surface and body waves, respectively). Naturally, in complex velocity structures, in particular in the near surface, this description is a rather simple approximation to use in order to describe amplitude variations of the seismic signals.

Concerning this, Sams and Goldberg (1990), in a borehole data study, concluded that a such simple geometrical divergence model was one of the causes of their bad Q estimations. In particular they obtained more reliable attenuation measurement by numerically estimating the divergence term and deconvolving it from experimental amplitude spectra. Practically, it means to compute through numerical simulations the elastic Green's function in a medium without attenuation. To this purpose, elastic properties of the medium, that is velocity and density model, have to be known. Actually, the Green's function term will include effects of complex interactions, energy partitioning among various wave types along layer boundaries, as well as focusing/defocusing effects. All these phenomena may generate inhomogeneous waves or leaky modes and are completely neglected by the geometrical spreading factor: this aspect, therefore, can affect the resulting Q measurements.

Then, the greater is the knowledge of the heterogeneity of the medium, the more accurate will be the retrieved elastic Green's function with respect to the real unknown medium structure. As a consequence, Q measurements will be closer to real attenuation values.

Based on all these considerations, a preliminary phase of study has been carried out. It was aimed to test the validity of the spectral ratio method and the reliability of the consequent dt^* measurements.

Synthetic tests have been performed in order to know the sensitivity of the spectral ratio method to different factors, that is: 1) velocity model; 2) selected signal time window; 3) frequency range over which the spectral ratios are computed and fitted.

Although, theoretically, through spectral ratio the source contribution is completely deleted from the spectrum, also the sensitivity of the method to two different types of sources has been investigated.

Finally, a method to take into account the complexities of the medium and to remove their effects from seismic signals has been tested on synthetic signals.

This methodological study has been aimed at the elaboration of a procedure for the dt^* computation on real data.

2.2 Synthethic tests

Synthetic tests have been performed on synthetic seismograms, which in turn have been obtained computing the Green's function by means of AXITRA (Coutant, 1989). It is a numerical code which implements the discrete wave-number Bouchon's (1981) theory in conjunction with reflectivity method (Kennet, 1983). The computation of Green's functions takes as input a 1D layered model of velocity, density and attenuation, as well as earthquake/shot position, source origin time and stations locations.

In detail, ten synthetic seismograms have been generated at progressively increasing distances from the 300 m shallow explosive source. In particular the receivers are located at the free-surface at epicentral distances from 1 km to 10 km, with an inter-receiver distance of 1 km (fig. 2.1). The source depth of 300 m has been chosen in order to simulate a surface source: actually, the numerical code does not allow to position both receivers and source on the free surface. Furthermore, an initial test using a 3 km depth source has been performed. Synthetic signals are characterized by a time sampling of 0.004 s. It corresponds to a Nyquist Frequency equal to 125 Hz and a maximum anti-aliasing frequency equal to 62.5 Hz.

The computed Green's functions in most tests have been convolved with a 0.2 s duration Ricker source; the unique closest station to the source (epicentral distance equal to 1 km) has been used as reference receiver. In other tests, Green's elastic function have been convolved with a 0.2 triangular source, too. All the following tests have been conducted only on P waves.

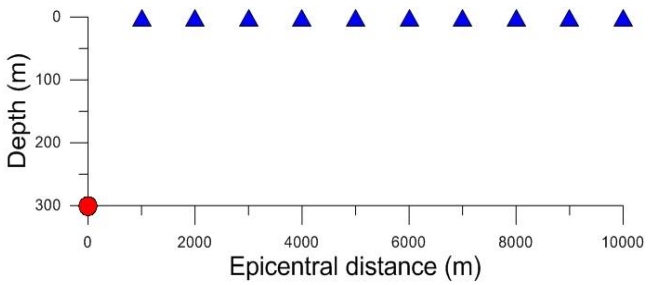

Figure 2.1. *Source-receivers configuration used in synthetic tests. The red point represents the source, the blue triangles the stations. The receivers are located at the free surface, at epicentral distances from 1 km to 10 km, with an inter-receiver distance of 1 km. The source is located at a depth of 300 m.*

In order to test on synthetic signals the reliability of dt^* measurements, these have been compared with theoretical dt^* values. Except for the trivial example of an homogeneous model both in elastic and in anelastic properties, the theoretical dt^* have been computed through the direct part of the tomographic inversion code TOMO_QDT. It is the adapted version to the case of the attenuation of the tomographic inversion code TOMO_TV.

A complete description of the numerical code will be given in the fourth chapter of this thesis, in which also the details about the modification that we brought to the code will be provided. In this paragraph, instead, the way in which the theoretical dt^* are computed is briefly described.

The forward problem of dt^* computation has been faced through the computation of absolute t^*. First, the propagation medium is modelled by means of a tridimensional inversion grid of nodes, at whose correspondence a quality factor (Q_P) and a velocity value (V_P) is assigned. Actually, only 1D velocity and attenuation models have been considered, so that at each depth the grid nodes have all the same value of quality factor and velocity.

Since t^* values depend on the ray paths, the ray tracing has been previously performed.

Ray paths depend only on velocity model and they have been retrieved by solving the Eikonal equation with a finite difference algorithm (Podvin and Lecomte, 1991). For this computation, a grid finer than the inversion grid is required; the velocity values of each node of this finer grid are obtained through a trilinear interpolation of the tomographic inversion grid. Podvin and Lecomte (1991) algorithm allows for each source-station couple to obtain a first estimation of travel time at each node of the fine

grid. Therefore, it is possible to obtain the ray path through a back ray tracing by following the gradient of the estimated travel times.

After the computation of ray paths, a refined estimation of t^* values is retrieved through the integration of η along the traced rays. The quantity η represents the reciprocal number of Q.

After theoretical t^* for every source-receiver couple have been obtained, the differential values, dt^*, are obtained by computing the difference between the corresponding t^* values.

2.2.1 Sensitivity of the method to V(z) models

The validity of the spectral ratio method and of dt^* measurements has been tested in different models with V(z) depending on depth. All the performed synthetic tests are characterized by $V_S = \frac{V_p}{\sqrt{3}}$ and ρ=2700 kg/m^3.

V(z)=cost and deep source

In this test a homogeneous velocity (Vp=6.5 km/s) and attenuation model (Q=100) have been implemented.

Two different signals for receiver 1 and receiver 5 are shown in the figure 2.2 as an example; their spectra and the relative spectral ratio are also shown in the figure 2.3. In figure 2.3 the dt^* measurements as a function of ΔR are shown overlapped to theoretical dt* values, too. The quantity ΔR, here, is the difference of the distances travelled by the two signals recorded at two different receivers; obviously, this quantity depends on the ray paths. It means that, with the same source-receivers configuration but changing the velocity models, ΔR quantities will be different.

A 1 s time window around the first arrival has been chosen; we are allowed to use such a large time window because no secondary arrivals are present in seismograms. Before computing the fast Fourier transform of the synthetic signals, zeros were added to 2^8 points. In that way a time window of 1.020 s, corresponding to a minimum frequency in the amplitude spectra of 0.98 Hz, has been obtained. Then, also the sampling of lower frequencies is guaranteed.

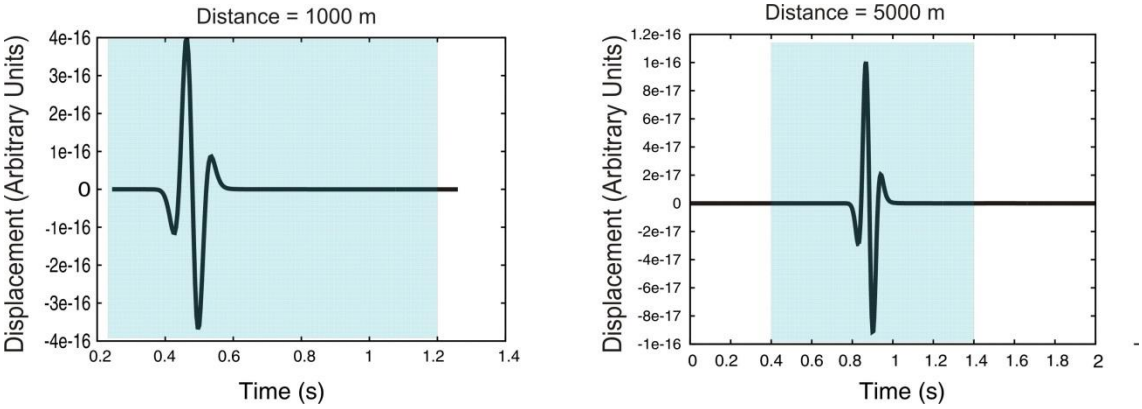

Figure 2.2. *Synthetic displacement seismograms at two different receivers. They are located at 1 km and 5 km epicentral distances, respectively. The cyan lightened area represents the portion of the seismogram that has been used to compute the amplitude spectra.*

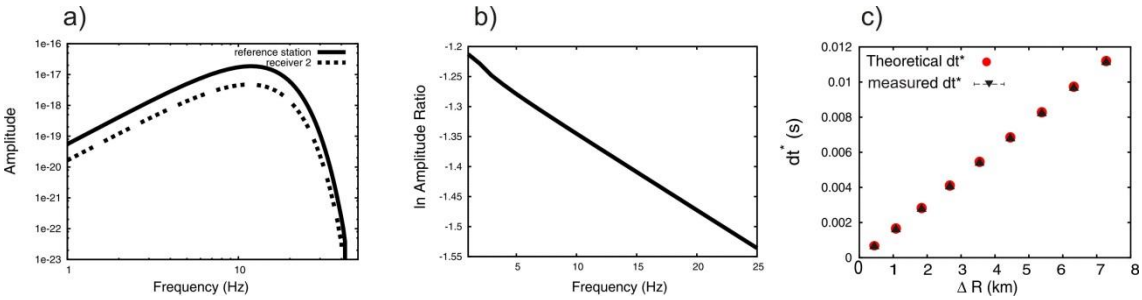

Figure 2.3. a) *Amplitude spectra of the signal recorded by the reference station (solid line) and by the station 5 km far from the source (dashed line).* ***b)*** *Spectral ratio computed between the two amplitude spectra represented in figure* ***a)****.* ***c)*** *Comparison between theoretical (red points) and measured* dt^* *(black triangles). There is a perfect agreement between measured and theoretical* dt^**. Furthermore, by fitting the* dt^* *distribution as a function of* ΔR *in the sense of least-squares, a Q=100.15 is retrieved.*

Based on results shown in figure 2.3, we can conclude that in optimal conditions, that are deep source and homogeneous model, spectral ratio method provides reliable dt* estimations.

Shallow source and V(z) velocity models.

The propagation of a wave field produced by a source (both an earthquake source and an explosive one) is greatly affected by the elastic properties of the medium in which waves travel.

A deep attention has been focused in this section on the velocity model. Actually it not only influences the arrival time of the waves at different receivers, but most of all it contributes to the generation of phases other than direct ones.

It is clear that in real conditions it could be very difficult to isolate phases different from the direct one; this depends on the possible overlapping of the phases and on a contamination of the signal to which we are interested.

The following synthetic tests have the aim to show the effects of velocity model on time domain signals and on their spectra, looking at the way they are reflected into dt^* measurements.

In particular, at first we have investigated the applicability of spectral ratio method in a gradient velocity model. After that, in order to give an answer about the applicability of the method in a real area, velocity models describing the elastic properties of Campi Flegrei area have been considered.

In detail, a continuous representation of Judenherc and Zollo 1D velocity model (2004) (JZ hereafter), an its smoother representation and the average 1D model obtained from 3D Campi Flegrei model (Battaglia et al., 2008) have been used.

An attenuation halfspace (Q=200) has been considered.

In these tests the source is shallower than the previous one (it is located at a depth of 300 m). The receivers configuration is the same of the previous one (fig. 2.1).

Gradient velocity model-MODEL 1

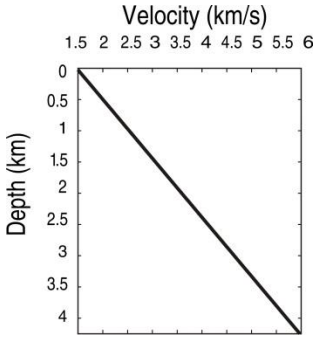

Figure 2.4. *Gradient velocity model.*

Also in this case, synthetic seismograms have been obtained convolving Green's functions computed by AXITRA with a 0.2 s duration Ricker source.

From figure 2.5 it is clear that also with a simple gradient velocity model a shallow source produces arrivals different from the P direct ones. They are due to free surface effects and generation of inhomogeneous waves. From an analytical point of view, it means that by using a very large time window, secondary arrivals will be included.

For this reason a 0.3 s time window has been chosen, starting from 0.05 s before the manually picked P first arrival time. Furthermore, zeros were added to total 2^7 points.

A cosine taper window of 10% fraction of tapering has been also applied to the cut signal in order to reduce the contribution of fictitious high frequencies in the amplitude spectra.

By considering the sampling time of the signal of 0.004 s, and the anti-aliasing corrections, the maximum frequency is 62.5 Hz. Since a zero padding has been done in order to compute fast Fourier transform of the signal, *df* is not equal to 3.33 Hz. Actually it is equal to 1.95 Hz. Finally, amplitude spectra have been smoothed with a moving 3 points averaging window.

The retrieved spectral ratios and measured dt^* are represented respectively by figure 2.6b and figure 2.7. The dt^* have been estimated by fitting the spectral ratio in the least-squares sense in the frequency range 5-25 Hz. The upper limit of the frequency range over which to fit the spectral ratio has been chosen looking directly at the individual spectra. It has been observed that for frequencies greater than 25-30 Hz the spectral amplitude is not meaningful.

Taking into account the *df* and the selected frequency range, then the spectral ratio has been fitted on a number of points equal to 10.

In particular it is possible to observe a very good fit between theoretical and measured dt^*, except for the 9/1 and 10/1 spectral ratios which correspond to Q estimations of 186 and 270 respectively (the theoretical Q_P value is equal to 200).

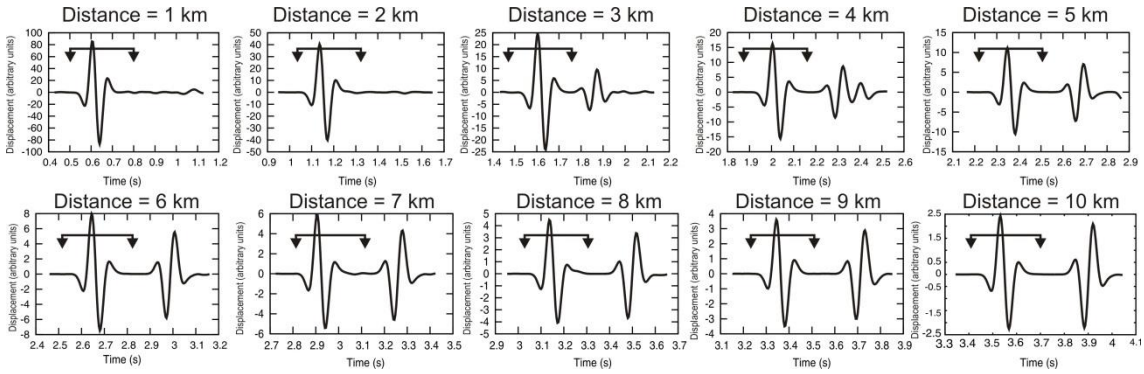

Figure 2.5 *Synthetic displacement seismograms generated by a shallow Ricker source and recorded at all receivers in a gradient velocity model. The traces have been cut in a 0.7 s time window only for this representation. The signal processing has been done, instead, on a 0.3 s signal time window (represented by the bar in each seismogram panel). It starts 0.05 s before the manually picked P first arrival.*

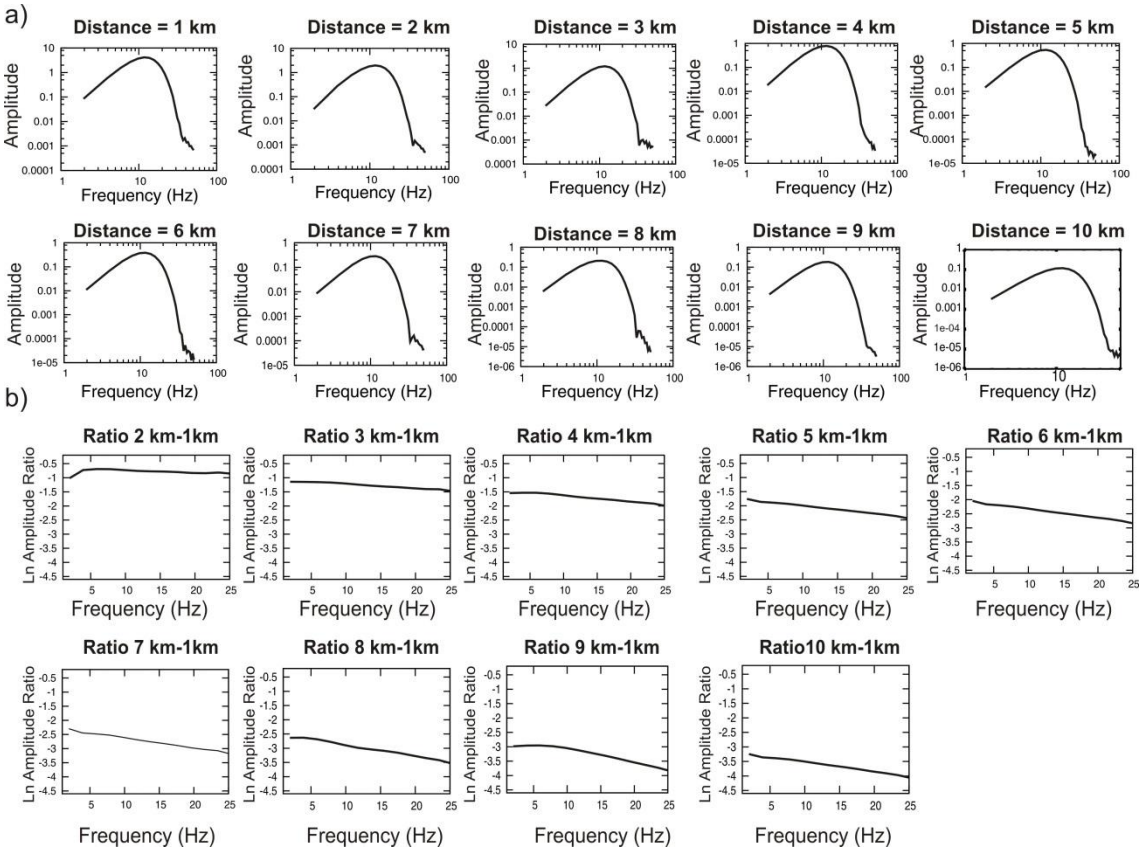

Figure 2.6 a) *Amplitude spectra of the synthetic signals recorded at the ten receivers. The amplitude spectra are very smooth and do not show any peak or spectral holes.* ***b)*** *Retrieved spectral ratios represented in the range 1-25 Hz; the higher frequencies are not represented because of the numerical noise visible directly in the amplitude spectra. A great linearity in the spectral ratios is observable: it is reflected in very small uncertainties in* dt^* *estimations.*

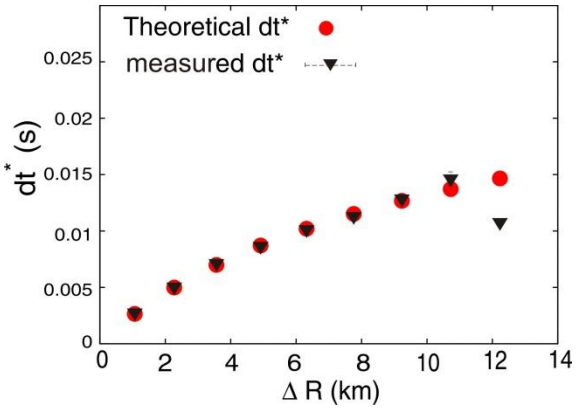

Figure 2.7 *Comparison between theoretical (red points) and measured dt* (black triangles): the agreement between them is very good, except for the ratio 9/1 and 10/1, for which the differences between estimated Q and real one correspond respectively to -14 and 76.*

JZ (2004) 1D velocity model-MODEL 2

The JZ 1D velocity model (2004) has been obtained from a tomographic study starting from the analysis of SERAPIS data set and part of Tomo-Ves 97 experiment data. It is a layered model, each layer having a thickness of 250 m.

Because, in the reality, Earth elastic properties gradually change, a continuous representation of JZ 1D velocity model has been used. It has been obtained linearly interpolating JZ 1D model. Then, by stacking homogenous plane layers having a thickness of 25 m, the velocity model has been constructed. After all, the Volterra theorem (see Gilbert and Backus, 1966) states that "wave system propagating in a medium with continuous spatial variations of density and wave speeds can be studied by solving for the waves in a discrete medium composed of many homogeneous parts" (cfr Aki and Richards, 1980).

Furthermore, the original JZ 1D model shows very strong velocity discontinuities among each layer; since Green's function are computed through reflectivity method, such velocity jumps are reflected in a great complexity of waveforms. On the other hand, the constructed continuous medium above described allows to obtain simpler wave forms, which can be more easily interpreted.

Simply looking at the velocity model, a strong velocity gradient at about 1.5 km is clearly visible. Furthermore, at greater depths (2 km and 2.5 km) two little velocity inversions are present.

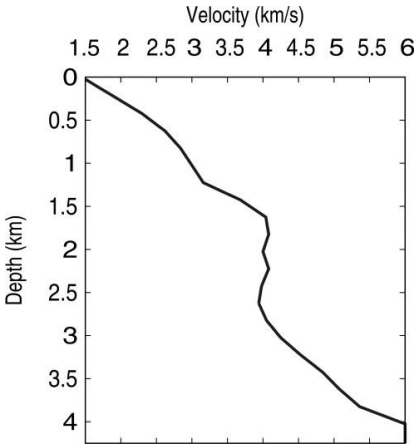

Figure 2.8 *Continuous representation of JZ 1D velocity model.*

Figure 2.9 shows that in addition to the presence of distinct secondary arrivals, P first arrivals are very often contaminated by interferences linked to the complexity of the

structure above described. It means that it is very difficult to choose a time window equal for all the signals and which allows to isolate only direct waves.

In particular these propagation effects are very clear for signals recorded by receivers at 3 km, 5 km, 6 km, 9 km, 10 km. Also the resulting spectra show an irregular form: it is directly related to time domain signal complexities (figure 2.10a). By computing the ratio between the amplitude spectra, some obtained spectral ratios are very far from a straight line; peaks and spectral holes, for example, are very clear for spectral ratios 5/1 and 6/1 (figure 2.10b).

Finally, dt^* have been measured by fitting spectral ratios by a least-squares regression (figure 2.11). The measured dt* values are very far from the theoretical ones, except some rare cases. Furthermore, most of the estimations are accompanied by a large error bar. Another aspect emerging by looking at figure 2.11 is that dt^* values do not show a coherent trend as a function of ΔR. It is clearly an effect of the interferences in the spectrum of the seismic phase that we are studying. It reflects the difficulty to isolate it and to remove the undesired contaminating propagation effects.

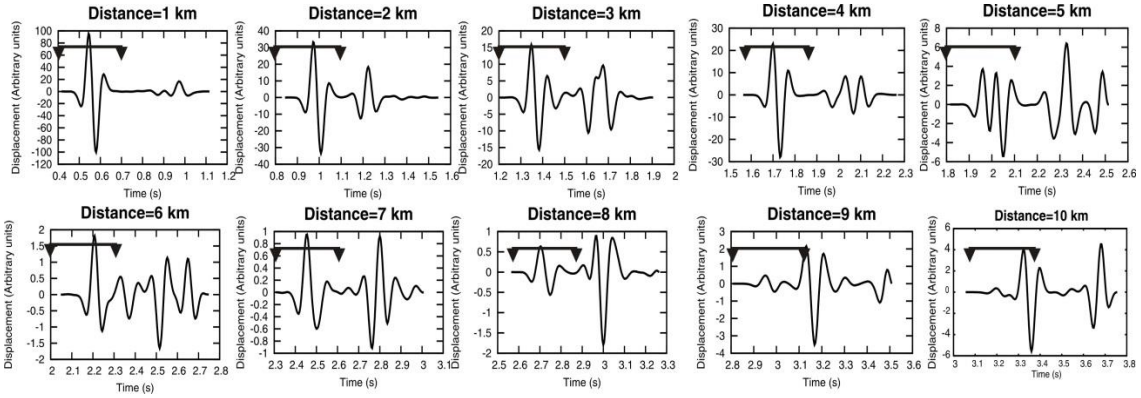

Figure 2.9 *Synthetic displacement seismograms generated by a shallow Ricker source recorded at all receivers for the continuous representation of 1D JZ velocity model (2004). The traces have been cut in a 0.7 s time window only for this representation. The signal processing has been done, instead, on a 0.3 s signal time window (represented by the bar in each seismogram panel). It starts 0.05 s before the manually picked P first arrival. For distances greater than 3 km, it is clear the complexity in the seismogram due to secondary phases arrival, principally. In particular, for some seismogram (e.g. receiver 5, 6, 8), the secondary phases are completely overlapped to the P first arrival, so that it is impossible to isolate a single phase in order to compute its amplitude spectrum.*

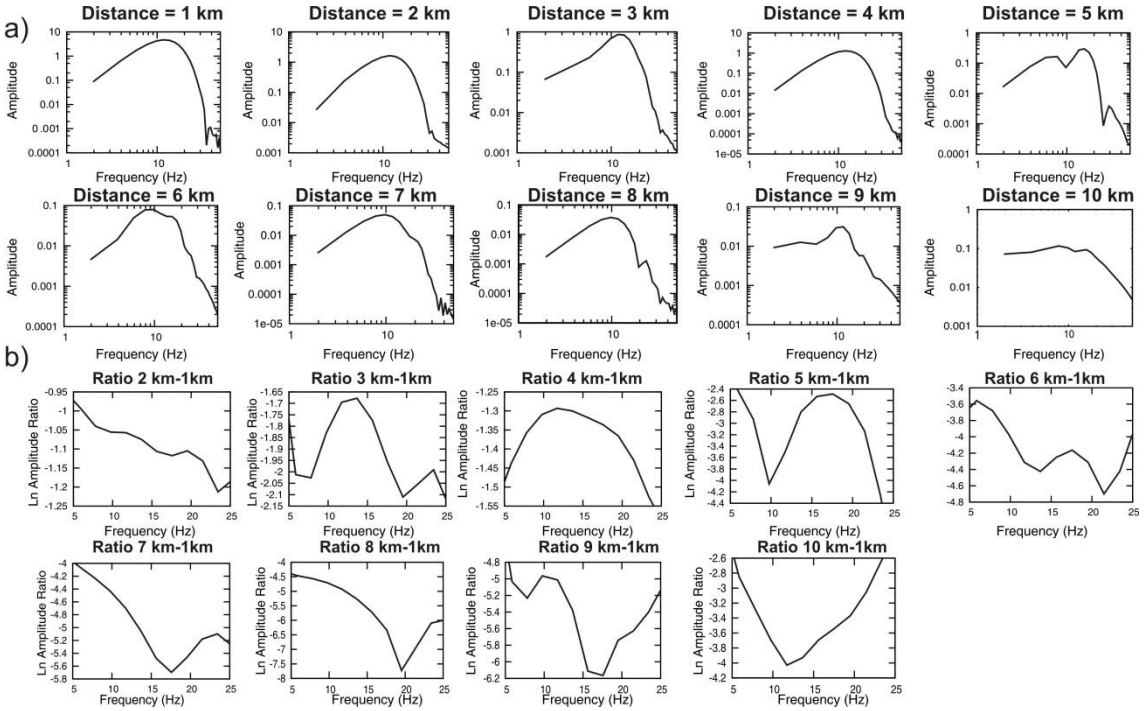

Figure 2.10 a) *Amplitude spectra of the synthetic signals recorded at the ten receivers. The complexities in the waveforms in the selected time window clearly influence the amplitude spectra.* ***b)*** *Retrieved spectral ratios represented in the range 1-25 Hz; the higher frequencies are not represented because of the numerical noise directly visible in the amplitude spectra. Spectral ratio in some cases are very far from the linear trend, due to the complexities of the individual spectral form.*

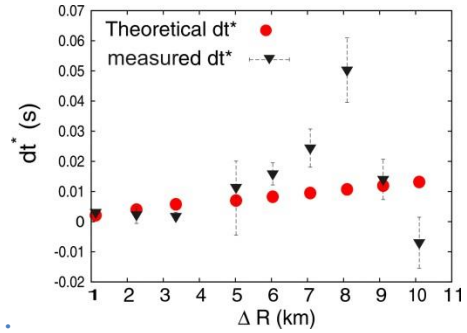

Figure 2.11 *Comparison between theoretical (red points) and measured dt* (black triangles); the fit between them is achieved only for the closest distances. Furthermore, for ΔR greater than 4 km, the dt* measurements have also a large error bar, which is indicative of spectral ratio far from a linear trend. The dt* value retrieved from the last spectral ratio (ΔR about 10 km) is negative: this is an impossible situation in the case of an homogeneous attenuating medium.*

Smooth representation of JZ 1D velocity model (2004) – MODEL 3

Due to the waveforms complexities produced by JZ 1D velocity model, another test has been performed; in particular a smoother model close, as much as possible, to JZ one has been considered (figure 2.12). This model has been obtained by fitting with a

polynomial function the velocity distribution vs depth of JZ 1D model. The retrieved model has been represented by a stack of 25 m thick homogeneous layers.

The great difference respect to JZ model is the absence of the strong velocity gradient at about 1.3 km depth. As explained before, such complexities greatly influence the signal producing multiple arrivals which in some cases contaminate the first arrival.

On the other hand, waves propagating in this medium maintain their original form without any interference in the P first arrival so that different phases are clearly separated; the only contaminated signals are those recorded by receivers at 9 km and 10 km (figure 2.13). Therefore, by looking at the synthetic seismic trace emerges that a propagation medium characterized by smooth variations of elastic properties allows to keep separation between the seismic phases.

Also in this case a time window of 0.3 s duration has been chosen; then, the same signal processing of the previous tests has been applied.

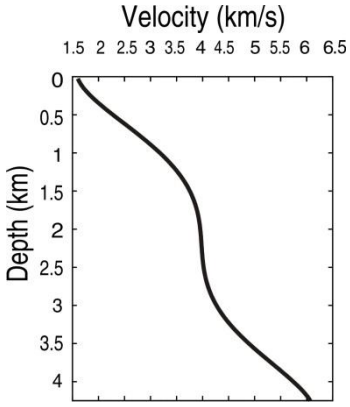

Figure 2.12 *Smooth representation of JZ 1D velocity model.*

The spectra and the spectral ratios are shown in figure 2.14a and figure 2.14b; the amplitude spectra are very smooth and have a very regular form, except for those relative to signals recorded at 9 km and 10 km. This is due to visible interferences in the time domain signal.

Concerning dt^* measurements, there is a very good agreement with theoretical dt^*; the only exceptions are dt^* values relative to spectral ratios 9/1 and 10/1.(figure 2.15).

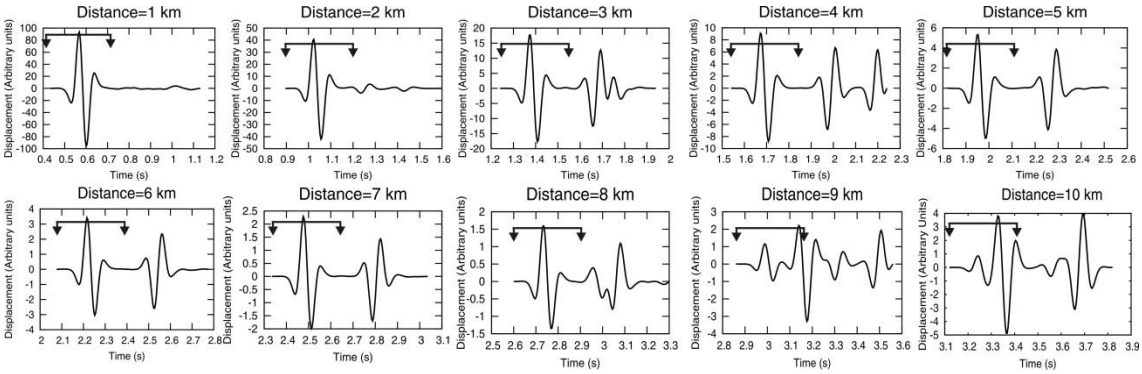

Figure 2.13 *Synthetic displacement seismograms generated by a shallow source recorded at all receivers for the smooth representation of 1D JZ velocity model (2004). The traces have been cut in a 0.7 s time window only for this representation. The signal processing has been done, instead, on a 0.3 s signal time window (represented by the bar in each seismogram panel). It starts 0.05 s before the manually picked P first arrival. The different seismic phases in each seismogram are completely separated, except for signals relative to synthetic seismograms recorded by receivers at 9 and 10 km.*

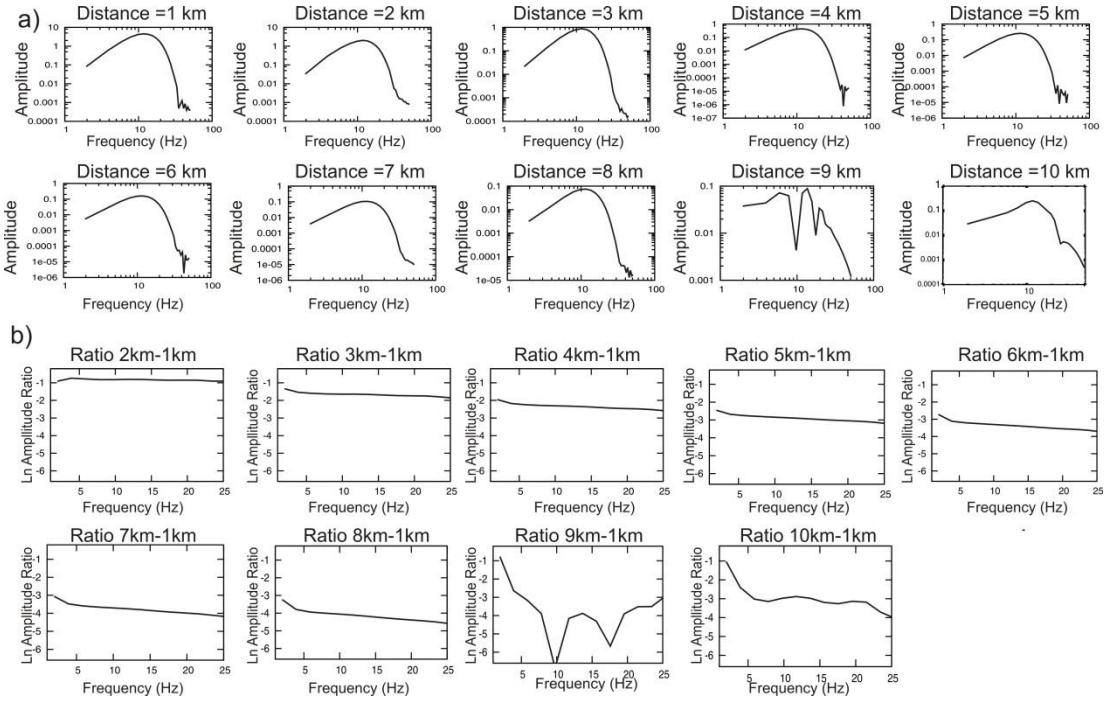

Figure 2.14 a) *Amplitude spectra of the synthetic signals at the ten receivers. The complexities in the waveforms in the selected time window influence clearly the amplitude spectra relative to receivers at 9 km and 10 km.* ***b)*** *Retrieved spectral ratios represented in the range 1-25 Hz; the higher frequencies are not represented because of the numerical noise visible directly in the amplitude spectra. The spectral ratio 9/1 is very far from a linear trend.*

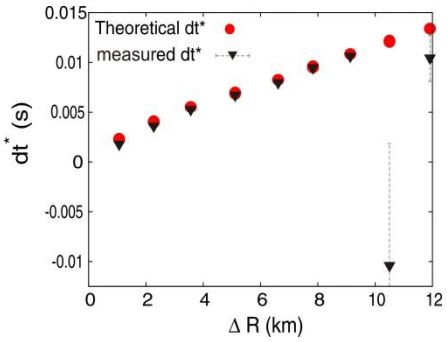

Figure 2.15 *Comparison between theoretical (red points) and measured dt* (black triangles). The agreement is perfectly kept except for spectral ratios 9/1 and 10/1.*

Average 1D Battaglia et al., (2008) model – MODEL 4

Battaglia et al. 3D model (2008) of Campi Flegrei is a three-dimensional velocity model obtained from the analysis of two merged datasets for the same area: an active seismic dataset (SERAPIS database) and earthquake data. In order to compute the synthetic seismograms, an average 1D model has been computed (fig. 2.16) and constructed, as usual, by staking 25 m thick homogeneous layers. Although this model does not show the JZ model complexities, it is possible to see two different velocity gradients: the former up to 2 km, the latter for greater depths. Small complexities characterize the model also in the upper 2 km.

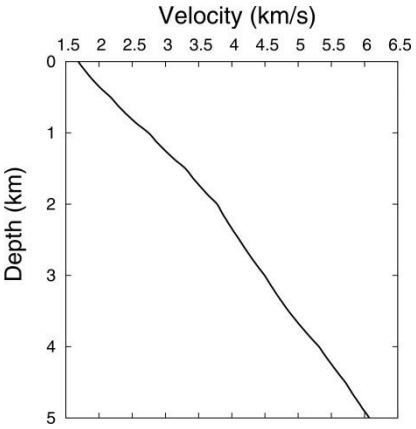

Figure 2.16 *Average 1D model of Battaglia et al. (2008) 3D velocity model.*

Concerning the synthetic waveforms, in this case important contaminations in P first arrivals are not clearly visible (figure 2.17). For two seismograms (signals at 6 km and 8 km) some very small interferences are present in the selected time window of 0.3 s duration. Furthermore, in all computed amplitude spectra, irregularities like spectral peaks or spectral holes are completely absent (figure 2.18a). This is reflected in spectral

ratios having a clear linear trend (figure 2.18b). Nevertheless, the fit between measured and theoretical dt^* is never respected and errors in dt^* estimations are very small (2.19); however, the differences between theoretical and observed values are in some cases very small.

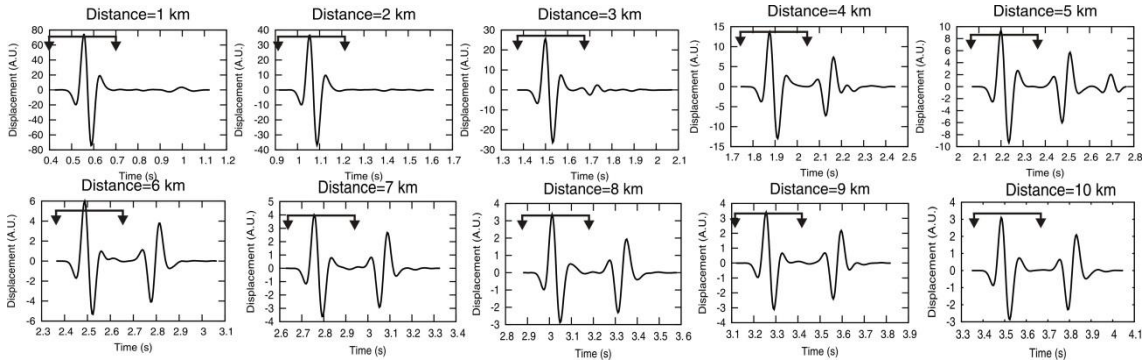

Figure 2.17 *Synthetic displacement seismograms generated by a shallow source and recorded at all receivers for the average 1D model of Battaglia et al. (2008) 3D velocity model. The traces have been cut in a 0.7 s time window only for this representation. The signal processing has been done, instead, on a 0.3 s signal time window (represented by the bar in each seismogram panel). It starts 0.05 s before the manually picked P first arrival. With this time window duration the secondary arrivals are completely discarded even if some very small signal disturbances are included in the selected time window (e.g. 6 km receiver signal, 8 km receiver signal).*

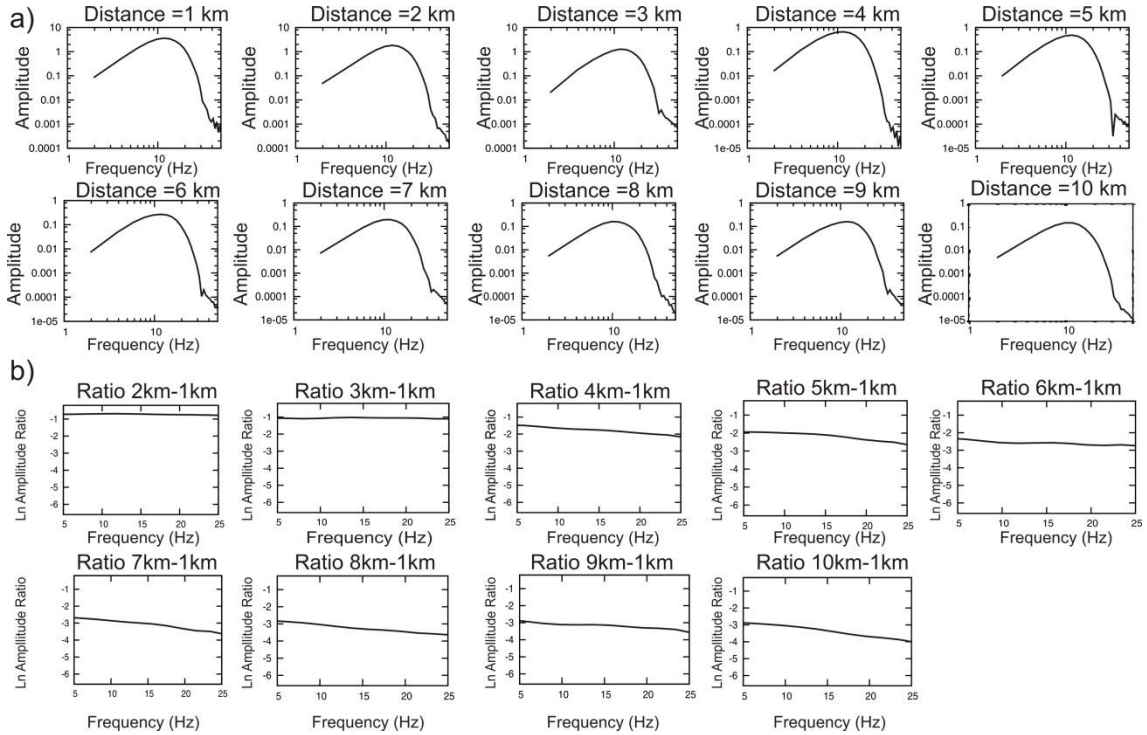

Figure 2.18 a) *Amplitude spectra of the synthetic signals recorded at the ten receivers. The complexities in the waveform in the selected time window influence clearly the amplitude spectra.* ***b)*** *Retrieved spectral ratios represented in the range 1-25 Hz; the higher frequencies are not represented because of the numerical noise visible directly in the amplitude spectra. All spectral ratios show a linear trend***.**

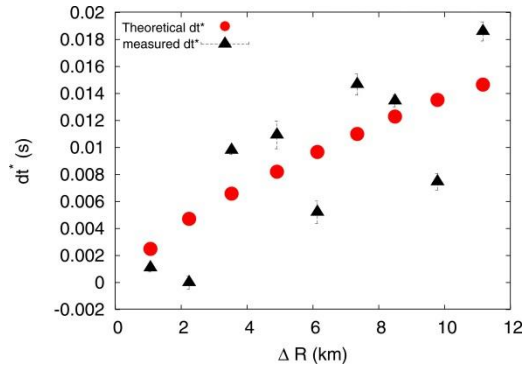

Figure 2.19 *Comparison between theoretical (red points) and measured dt* (black triangles). Despite the linear trend shown by spectral ratios, the fit between measured and theoretical dt* is never respected.*

2.2.2 Sensitivity of the method to the source function

Synthetic tests referring to model 2, model 3 and model 4 (cfr. previous paragraph) have been repeated changing only the source function; actually, Green's functions have been convolved with a 300 m depth triangular source of 0.2 s duration. This source time function is simpler than Ricker function, which introduces a greater number of oscillations in the waveforms.

The resulting velocity seismograms obtained for JZ model (model 2) are shown, only as an example, in the figure 2.20. The spectra have been computed with the same criterion followed in the previous tests: a time window of 0.3 s has been chosen, starting from 0.05 s before the picked P arrival.

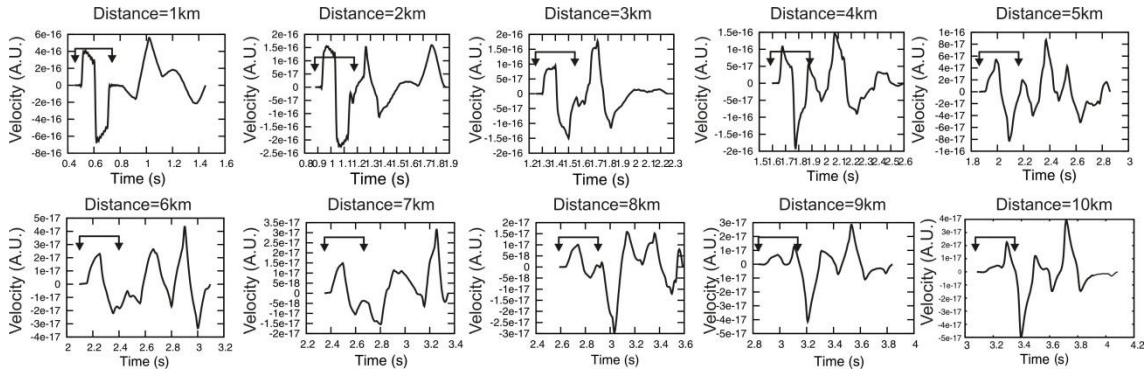

Figure 2.20 *Synthetic velocity seismograms generated by a shallow triangular source recorded at all receivers for the continuous representation of 1D JZ velocity model (2004). The traces have been cut in a 1 s time window only for this representation. The signal processing has been done, instead, on a 0.3 s signal time window (represented by the bar in each seismogram panel). It starts 0.05 s before the manually picked P first arrival. In comparison to signals generated by Ricker source, they are more difficult to be interpreted, even if it is clear that at greater distances from the source the signal become more and more complex.*

A cosine taper window with a 10% fraction of tapering has been applied to the P wave window. Differently from the other tests, due to greater oscillations in the spectra, an averaging smoothing window of 5 points total width has been used (figure 2.21a).

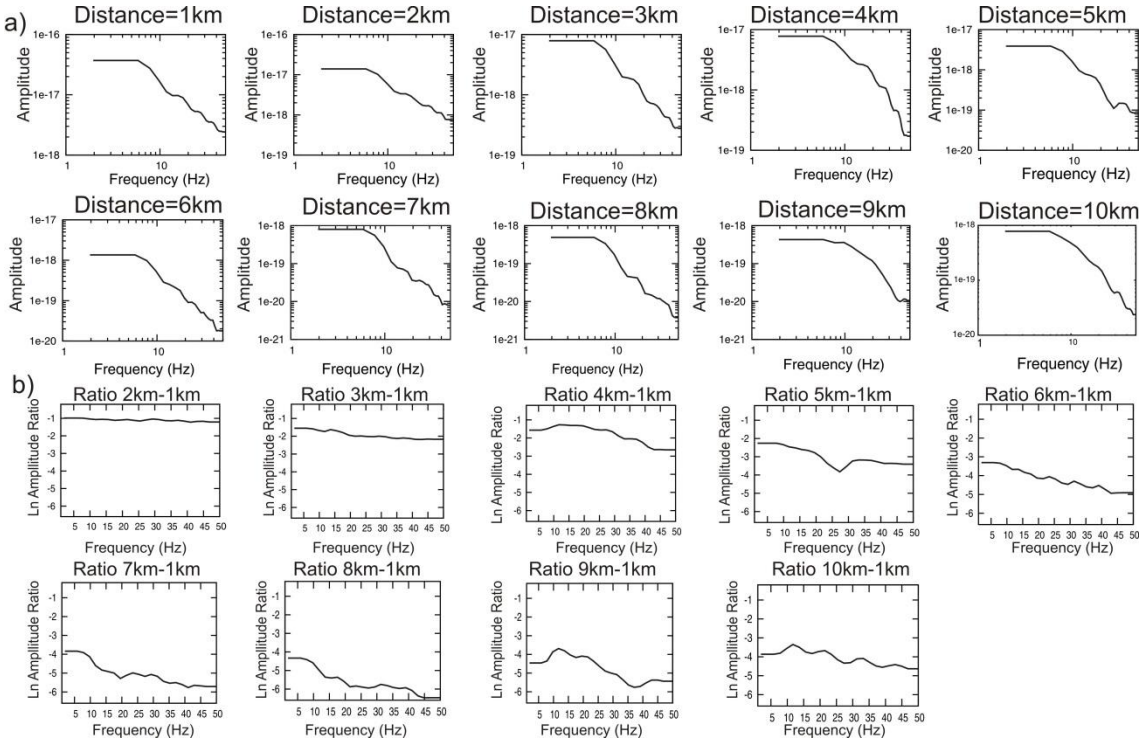

Figure 2.21 a) *Amplitude spectra of the synthetic signals recorded at the ten receivers represented in the frequency range 1-50 Hz. Higher frequencies have been cut because their spectral amplitudes are not so much meaningful respect to lower frequencies spectral amplitudes.* ***b)*** *Retrieved spectral ratios represented in the range 1-50 Hz.*

For these tests, dt^* have been measured by fitting spectral ratios in 5-50 Hz frequency range. The lower frequency limit has been chosen considering that spectra smoothing introduces a fictitious plateau up to 5 Hz. The upper limit, instead, has been chosen comparing higher frequencies amplitudes to spectral amplitudes recorded at low frequencies.

In figure 2.22 comparisons between theoretical and measured dt^* for the three different models are shown. The best agreement between theoretical and measured dt^*, also in the case of a triangular source, is obtained for the smooth representation of JZ 1D model (model 3). The complexities of JZ model greatly affect dt^* estimations. However, we can conclude that dt^* measurements relative to synthetic signals generated by a triangular source are more reliable than those obtained with a Ricker source.

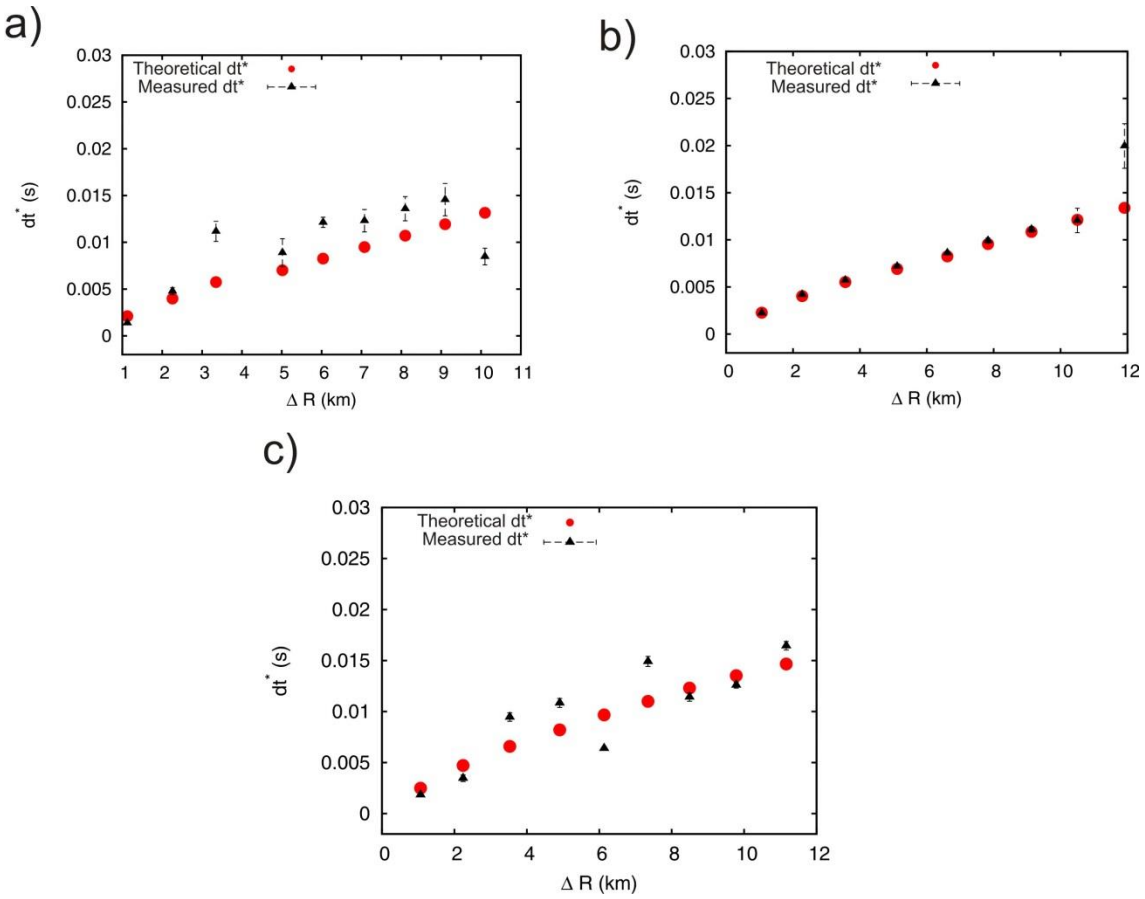

Figure 2.22 *Comparison between theoretical (red points) and measured dt* (black triangles) for different velocity models:* ***a)*** *JZ 1D velocity model (2004);* ***b)*** *Smooth representation of JZ 1 D velocity model (2004);* ***c)*** *Average 1D Battaglia et al. (2008). As well as with a Ricker source, the best agreement between measured and theoretical dt* is obtained with the smooth representation of JZ 1D velocity model. However, the simplicity of the source function allows to obtain better dt* estimates, even if both for 1D JZ velocity model and for the average 1D Battaglia velocity model there is not agreement between theoretical and measured dt*.*

2.2.3 Sensitivity of the method to the selected time window

In order to give an answer to the time window issue mentioned in the introduction, spectral analyses have been performed for different time interval durations: 0.3 s, 0.5 s, 1 s.

In particular, these tests have been repeated for synthetic signals generated by a shallow triangular source in the smooth representation of 1D JZ velocity model: actually, it has been shown that this velocity model is the one furnishing the most reliable dt* measurements.

After the cut of traces, signals have been tapered with the same cosine tapering window before described. Finally, spectra have been differently smoothed depending on the

selected time interval duration: the greater it is, the greater both the spectral resolution and the width of the averaging smoothing window are. In detail, for 0.5 s time window spectra have been smoothed with a total width window of 7 points; on the other side, 9 points of smoothing have been used in the case of a 1 s selected time window. Also in these tests, dt^* have been measured in the frequency range 5-50 Hz.

Figure 2.23 shows the dt^* distribution as a function of ΔR for each performed test: it clearly emerges that the best agreement between theoretical and measured dt^* is obtained selecting signal time window of duration equal to 0.3 s. Furthermore, figure 2.23 suggests that the gap between theoretical and measured dt^* does not necessarily increase by expanding the time window duration. For example let us look at the dt^* estimations relative to spectral ratio 3/1 and 4/1 (they correspond to points between 2 and 4 km ΔR): the measured dt^* relative to 1 s signal time window (purple triangles) show a better agreement with theoretical dt^* than measured dt^* relative to 0.5 signal time interval (blue triangles). This observation seems to confirm Sams and Goldberg (1990), Ingram et al., (1985) and White (1992) conclusions; in summary, they stated that the stability of the method increases expanding the time window. On the other side, a completely opposite behavior is observed from figure 2.23 at ΔR greater than 4 km.

However, the most evident aspect is that the best results are obtained considering a signal window of 0.3 s duration.

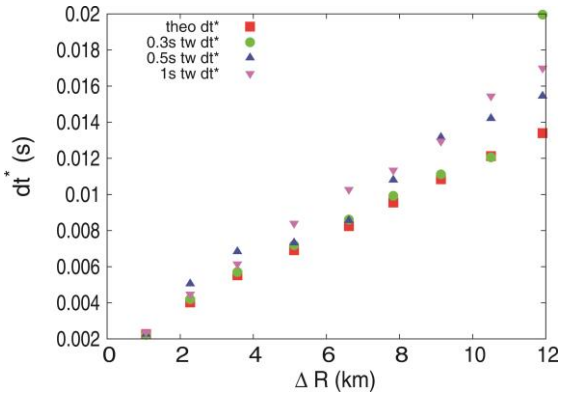

Figure 2.23 *Comparison between theoretical (red points) and measured dt^*, each one relative to a different selected signal time window (green points: 0.3 s; blue triangle: 0.5 s; purple triangle: 1 s).*

Tests described in the previous paragraphs were aimed to study the sensitivity of the method to different factors. Taking into account results of performed tests, two first conclusion can be drawn:

1) The application of spectral ratio method furnishes reliable dt^* measurements in smooth velocity models; the smoother is the model, the more reliable is the computed dt^* value.
2) It is necessary to choose the smallest time window which let us to remove secondary arrivals. In our case, a time window lightly greater than the source time duration has been chosen (0.3 s signal time window VS 0.2 source duration).
Nevertheless, results referring to the gradient velocity model suggest that isolating the first arrival is not always sufficient to obtain reliable dt^* measurements. Furthermore, tests on average 1D Battaglia et al. (2008) velocity model, as well as the one on the smooth representation of JZ 1D velocity model (2004), state the even very small interferences in the selected time window affect dt^* measurements.

2.3 Deconvolution procedure

As suggested by Sams and Goldberg (1990) and already said in the introduction, there is one more reason for which the spectral ratio method can lead to a wrong or uncertain dt^* estimation. Indeed, in most cases, amplitude variations due to elastic properties of the medium are accounted for by geometrical spreading factor that is described in its exponential form $|r|^{-\nu}$. This is a too simple approximation and it can affect attenuation measurements.
The technique here tested has been already proposed by Sams and Goldberg (1990) and reformulated by Xie (2010). In particular, it consists in removing the effects of the elastic Green's function from amplitude spectra of real signals.
Obviously, in order to properly compute the path effects produced by elastic properties, a complete knowledge of heterogeneous velocity and density structure is required. Unfortunately, it is, up to now, impossible. However we can exploit partial knowledges coming from gravimetric and tomographic studies to reduce at the minimum the errors.
In order to better describe the so called ***deconvolution procedure***, the equation which model the amplitude spectrum is recalled, that is:

$$A(f) = S_t(f)S_s(\theta,\varphi)C(f)G(t)I(f)\exp\left(-\pi t^* f\right). \qquad (2.1)$$

Based on what we have said before, the path geometric spreading must be substituted by the more complete elastic Green's function *J(f,x)*, giving the expression:

$$A(f) = S_t(f)S_s(\theta,\varphi)C(f)J(f,x)I(f)\exp\left(-\pi t^* f\right). \quad (2.2)$$

Note the dependence of the elastic Green's function on both the distance (represented by the term x) and on the frequency: the former allows to describe the geometric attenuation in an isotropic medium, the latter, instead, the amplitude variations linked to structure complexities.

In a complete elastic medium the recorded amplitude spectrum will be

$$A(f) = S_t(f)S_s(\theta,\varphi)C(f)J(f,x)I(f), \quad (2.3)$$

since there is no anelastic attenuation contribution.

If we were able to compute the elastic Green's function *J(f,x)* of the medium of which we want to study anelastic properties, we could divide equation (2.2) by the elastic Green's function term. In this way a *reduced amplitude spectrum* (Xie, 2010) is obtained:

$$\frac{A(f)}{J(f,x)} = S_t(f)S_s(\theta,\varphi)C(f)I(f)\exp(-\pi t^* f). \quad (2.4)$$

By performing this operation for all the receivers, the effect of a frequency-dependent Green's function should not more influence the spectral ratio computation and dt^* estimation.

As a matter of fact, let us consider two receivers at two different positions x_1 and x_2.

From equation (2.4):

$$\frac{A_1(f)}{J(f,x_1)} = S_t(f)S^1{}_s(\theta,\varphi)C(f)I(f)\exp(-\pi t^* f) = \bar{A}(f,x_1) \quad (2.5)$$

$$\frac{A_2(f)}{J(f,x_2)} = S_t(f)S^2{}_s(\theta,\varphi)C(f)I(f)\exp(-\pi t^* f) = \bar{A}(f,x_2) \quad (2.6)$$

Then, we divide equation (2.6) by equation (2.5), that is the far reduced spectral ratio divided by the reference reduced spectral ratio. By taking the logarithmic form:

$$\ln\frac{\bar{A}(f,x_2)}{\bar{A}(f,x_1)} = \ln\frac{S_s^2(\theta,\varphi)}{S_s^1(\theta,\varphi)} - \pi f\left(t_2^* - t_1^*\right) \quad (2.7)$$

The slope of the best fit line of the "deconvolved spectral ratio" is proportional to the *differential attenuation* term.

2.3.1 Application of deconvolution procedure

The above described procedure has been tested on synthetic seismograms generated with average 1D Battaglia et al. (2008) velocity model.

The same synthetic seismograms previously generated in an attenuating medium by a triangular source have been used.

On the other hand, to accurately assess the elastic Green's function of seismic phases, the propagation medium must have no anelastic attenuation. In order to avoid a computational singularity, the reflectivity method requires a nonzero amount of attenuation for the medium (Yang, 2002; Yang et al., 2007). For this reason we made calculations for models that have quality factor Q_P=100,000.

Furthermore, due to the difficulty of extracting from the numerical code the elastic Green's function, "elastic" synthetic seismograms have been generated. They were retrieved convolving elastic Green's functions first with a 0.2 s duration triangular source and, in a second test, with a 0.01 s duration triangular source. In particular, the second test allows to reduce as much as possible the source effect on the amplitude spectrum: actually, a triangular source of such duration has a flat spectrum up to 100 Hz.

The purpose of these two different source duration tests is to demonstrate the applicability and validity of the procedure independently from the duration of the source for which the elastic Green's functions are convolved.

Figure 2.24, represents the ratio between two amplitude spectra retrieved from elastic synthetic seismograms: in particular, they were relative to receivers at epicentral distances of 4 km and 1 km. These synthetic seismograms have been generated convolving the elastic Green's functions with a 0.01 s time duration triangular source.

Figure 2.24 shows that the spectral ratio is not constant varying the frequency. It confirms that, even in a completely elastic medium, there is a frequency dependent term, that is the elastic Green's functions. It confirms the idea above described of the necessity to remove this contribution in order to obtain more reliable dt^* measurements.

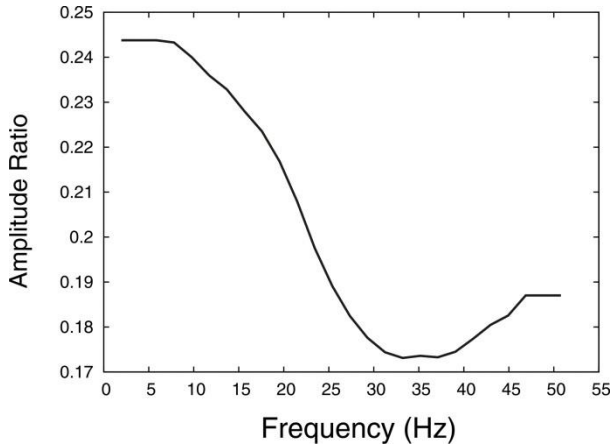

Figure 2.24 *Spectral ratio between amplitude spectra of elastic synthetic seismograms recorded by receiver at epicentral distances of 4 km and 1 km, respectively. The fact that the spectral ratio is not constant is a confirm of the frequency dependence of elastic Green's function term.*

Figures 2.25 and 2.26, instead, show the results obtained with the application of the deconvolution procedure in both tests. The dt^* have been measured by fitting the spectral ratios in two different frequency ranges: 5-25 Hz and 5-50 Hz. This has been done in order to see the differences in the obtained dt^* values based on used frequency band. Also, the comparison with results obtained without applying deconvolution procedure are shown.

However, the influence of used frequency range should be analyzed more deeply considering also the contribution of synthetic noise to signals.

Looking at figures 2.25 and 2.26, it is clear that the application of deconvolution procedure to synthetic signals improves the reliability of dt^* measurements. In particular, the best agreement between theoretical and measured dt^* is obtained by fitting spectral ratios in the frequency range 5-50 Hz. As said before, it is only a preliminary consideration, since on real data, the frequency range over which to fit the spectral ratio is strongly dependent on the noise content.

Therefore, we can conclude that

1) the choice of the source duration for which the purely elastic Green's functions are convolved is not important. Very good dt^* estimations, actually, are obtained in both synthetic tests.
2) For data analysis, the frequency range over which spectral ratio is fitted has to be taken into account.

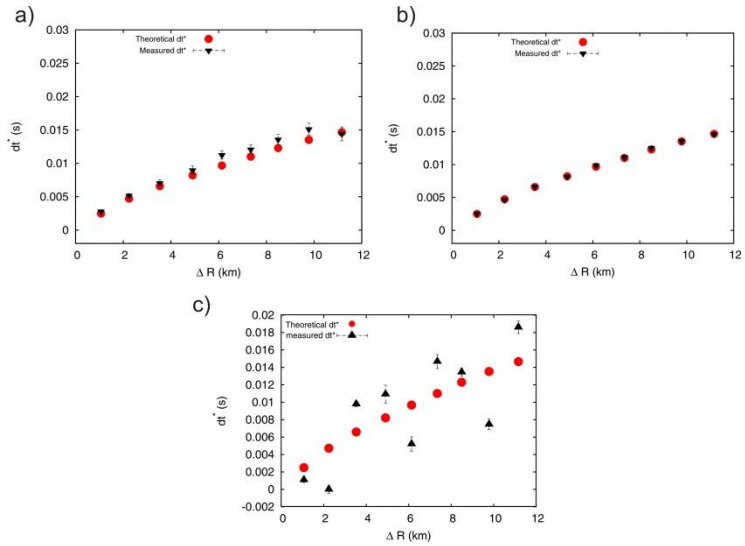

Figure 2.25 *Comparison between theoretical (red points) and measured dt*(black triangles). The elastic Green's functions have been convolved for a triangle source of 0.2 s duration.* ***a)*** *Results after application of deconvolution procedure; the spectral ratios have been fitted in the frequency range 5-25 Hz. The fit between theoretical and measured dt* is better than that one obtained without the application of deconvolution procedure.* ***b)*** *Results after application of deconvolution procedure; the spectral ratios have been fitted in the frequency range 5-50 Hz: there is a complete agreement between theoretical and measured dt*.* ***c)*** *Results without the application of deconvolution procedure. The spectral ratios have been fitted in the 5-50 Hz frequency range.*

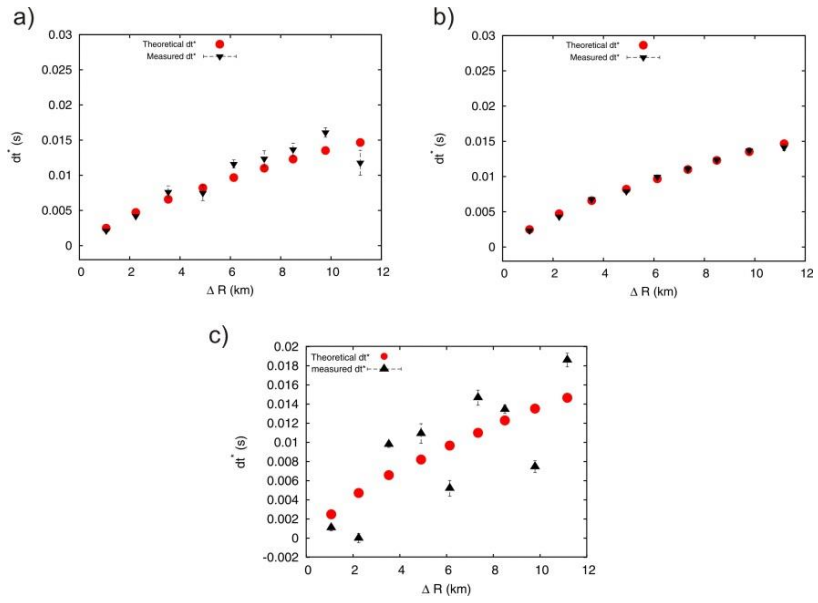

Figure 2.26. *Comparison between theoretical (red points) and measured dt* (black triangles). The elastic green functions have been convolved for a triangle source of 0.01 s duration. a) Results after application of deconvolution procedure; the spectral ratios have been fitted in the frequency range 5-25 Hz. The fit between theoretical and measured dt* is better than that one obtained without the application of deconvolution procedure.* ***b)*** *Results after application of deconvolution procedure; the spectral ratios have been fitted in the frequency range 5-50 Hz: there is a complete agreement between theoretical and measured dt*.* ***c)*** *Results without the application of deconvolution procedure. The spectral ratios have been fitted in the frequency range 5-50 Hz.*

CHAPTER 3

Data analysis: application of spectral ratio method to an active seismic database

3.1 Introduction

In the past, the spectral ratio technique has been applied both on active seismic data (e.g. Badri and Mooney, 1987; Evans and Zucca, 1988; Sams and Goldberg, 1990; Matheney and Novack, 1995) and on earthquake data (e.g. Teng, 1968; Taylor et al., 1986; Ponko and Sanders, 1994; Yoshimitsu et al., 2012).

The great advantage of active seismic experiment data is that the position of sources and of receivers is a-prior established. In that way a very dense ray coverage is achieved. On the other hand, the source is generally located at the surface or at very shallow depth. For a tomographic study, for example, this aspect greatly affects the investigation depth. In fact, in that case, the investigation depth will depend on two factors: 1) the maximum horizontal distance between the source and the receivers; 2) the true velocity model which describes the target medium. Furthermore, the proximity of the source to the free surface facilitates the generation of inhomogeneous and surface waves, as well as converted phases due to weathered layer effects. All these aspects are reflected in a greater complexity of the waveform. Concerning the earthquake data, they usually give the possibility of investigating at greater depth the propagation medium.

In this work, the spectral ratio method has been applied to the active seismic database obtained through SERAPIS experiment in order to provide a Q_P tomographic image of Campi Flegrei caldera.

In this chapter we will provide a complete description of SERAPIS experiment; furthermore we will illustrate how the spectral ratio method has been applied to the real database. In particular a deep focus on how seismic signals have been analysed will be

provided. Finally, the criterion that has been followed in order to select measured dt^* will be explained and the final data distribution will be presented.

3.2 The SERAPIS experiment

A dense and extended marine seismic survey called "SERAPIS" has been performed during September, 2001 in the gulfs of Naples and Pozzuoli. It provided a dense coverage of Pozzuoli Bay, of the coastal part of the Campi Flegrei caldera, and of the western sector of the Gulf of Naples. The source and receiver arrays covered an area of more than 50 x 50 km^2 (fig. 3.1).

During the field operation about 5000 shots, at 125 m distances, have been recorded at a network of 72 sea bottom receivers (OBS) and 84 land stations seismographs. Each shot has been produced by a battery of 3-6-12 synchronized air-guns mounted on the oceanographic vessel NADIR (owned by IFREMER). Concerning seismic stations, OBS were equipped with a 4.5 Hz three component sensors and a continuous recording device; on the other hand, land seismographs consisted of 18 vertical and 66 1Hz three component sensors operating on continuous recording during the experiment. The signals were recorded with a time sampling of 0.004 s, both by on land stations and offshore OBS. In the frequency domain, it corresponds to a Nyquist frequency equal to 125 Hz.

Near the coastline, shots were fired during the night, in order to reduce noise problem and due to dense urbanization of the area. For these reasons, furthermore, only three and six air-guns were operated near the coastline and in the Pozzuoli Bay. On the contrary, offshore, all 12 air-guns were used. In this way also the recordings of high energy P waves at distance of 40 km has been possible.

The oceanographic ship covered a total of 620 km along dense grid-lines oriented N-S and E-W in the Gulf of Pozzuoli, and along a few grid lines in the Gulf of Naples. All of the seismic lines were re-sampled at least twice, using a staggered configuration, which results in a smaller source spacing (less than 65 m). The acquisition layout was designed to provide a very high density in Pozzuoli Bay (about 1500 shots were fired inside the Bay) for an explored surface of 5 x 5 km^2. The other shots were fired in the Bay of Naples along some 10-20 km long profiles (cfr. Capuano et al., 2006).

The original SERAPIS dataset processing consisted of examining 300,000 OBS waveforms and 400,000 waveforms from stations on land. It provided more than 85,000 manually picked P first arrivals (fig. 3.2). These data have constituted the basis of the further analyses which we carried out.

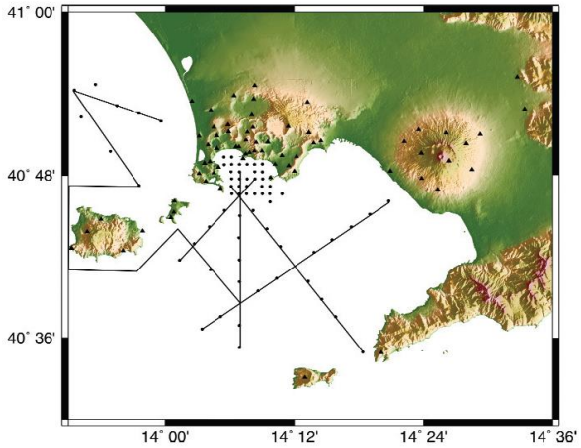

Figure 3.1 *Map of the investigated area during the SERAPIS experiment. The black triangles represent the position of stations; the solid lines, instead, represent the shot lines in the Pozzuoli Bay and in the Gulf of Naples (after Capuano et al., 2006).*

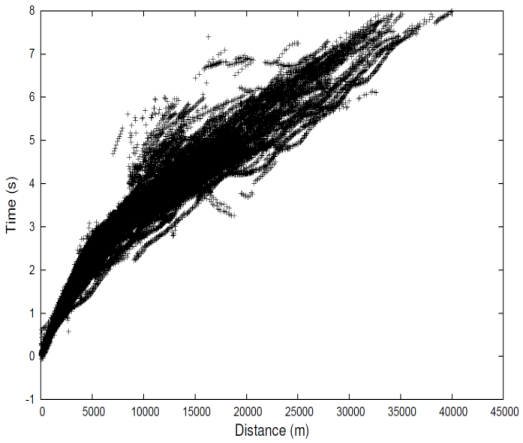

Figure 3.2 *Picked P first arrivals used in our study.*

3.3 The analysis of SERAPIS dataset.

Since on land station traces show a very low signal to noise ratio due to the high cultural noise in the area, in our study only traces recorded by OBS have been used. In particular, only seismograms recorded by OBS vertical component have been considered.

Moreover, among all SERAPIS dataset seismic traces, only those referring to shots and receivers located inside the Pozzuoli Bay have been considered. More than 1500 shots and 35 receivers have been selected in our tomographic study. They correspond to a total number of 41,768 seismic traces for which the P first arrival had been already picked.

Furthermore, all traces relative to receivers (horizontal offset between 2 m and 400 m) showing a physical saturation of the signal due to their proximity to the source have been discarded from our analysis (figure 3.3).

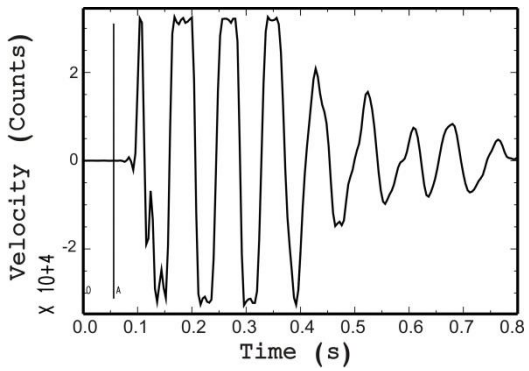

Figure 3.3 *Example of saturated traces recorded by a receiver very close to the source. Indeed, the horizontal distance between the OBS 011 and the shot 3469 is equal to 80.30 m.*

For spectral analysis, P first arrival time picked in the past by other people have been used.

3.3.1 Signal analysis processing

The original traces of SERAPIS database were arranged in common receiver gather sections and were saved into SEGY format. Therefore, at first, seismic signals have been converted from SEGY format into SAC (Seismic Analysis Code, 1995, Regents of the University of California) format. This operation has been necessary in order to carry out more easily all signal processing. It consisted in the cut of the traces, cosine tapering of the signal, computation of the fast Fourier transform and smoothing of the amplitude spectra.

First, the issue relative to time window duration selection has been faced. Based on synthetic tests results, the time interval duration should be lightly greater than the source duration. In our case, however, no useful informations about the duration of the seismic source are available. Actually, elastic waves propagating inside the Earth and recorded by OBS are not directly generated by air guns explosions. In fact, explosions produce only acoustic waves travelling in the water layer. The actual source generating elastic waves is thought to be linked to the complex coupling and interaction between the acoustic wave and the sea floor. The lack of information about the source properties did not allow us to establish in a proper way the duration of the time window on which to compute signal amplitude spectra.

Therefore, the following criterion has been followed: by directly looking at the seismic signals recorded by vertical components of OBS it is clear the difficulty to distinguish the different phases. However, it seems obvious that, with increasing of the duration of

the time window, the risk to contaminate the P first arrival spectrum greatly increases (figure 3.4).

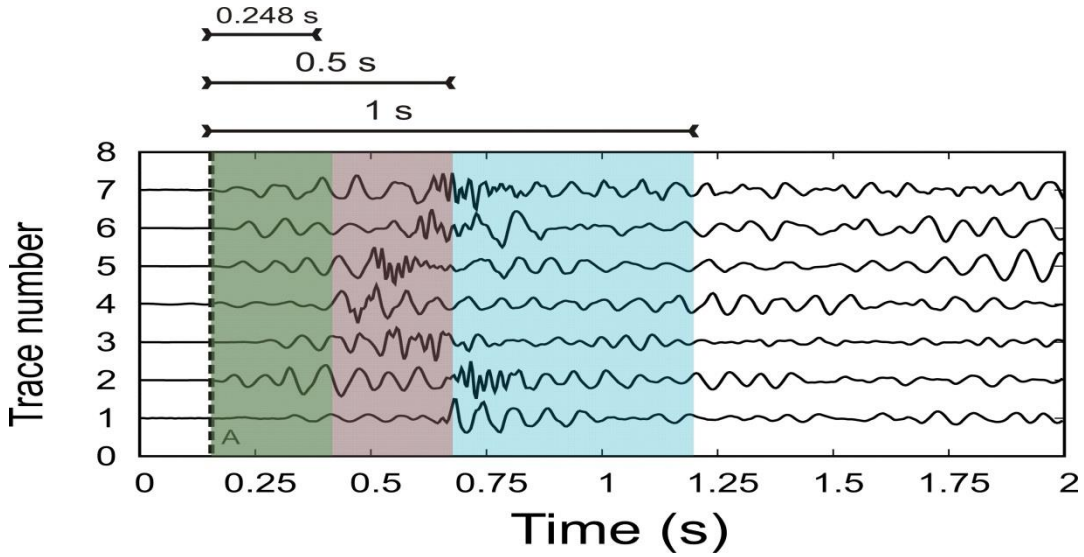

Figure 3.4 *Examples of six traces from SERAPIS dataset. The different shaded areas represent three different time windows, 0.248 s, 0.5 s and 1 s, respectively. The dashed vertical line represents the picked P first arrival. Note that by increasing the time window duration, other phases from the first arrival are included.*

Furthermore, it seems more reasonable to suppose a short source function duration than a longer one. For this reason, also taking into account the conclusions provided in the previous chapter, a time window of 0.248 s has been chosen. Selected time window starts 0.05 s before the picked P first arrival time.

We think that this time window duration is a good compromise between a too short and a very long window length; the former allows to isolate first arrivals to the detriment of a very low spectral resolution, the latter will have a complete opposite behavior.

In order to reduce distortions due to the windowing of the signal, a cosine taper function with a fraction of tapering equal to 5% has been applied to P wave time series.

After it, the displacement amplitude spectrum of the selected phase has been computed by means of a FFT on a number of points equal to 2^6. Due to the duration of the selected time window, the minimum retrieved frequency is equal to 3.90 Hz. Next, an averaging moving window with a total width of 3 points has been used to smooth the amplitude spectra.

In the synthetic tests described in the second chapter no considerations about the noise influence have been done. In the case of real data it is not possible to ignore this contribution and its effect on signal analysis. For this reason, all operations above

described and relative to the signal window have been applied to a noise window, too. It has the same duration of signal window and it has been selected before the picked P first arrival. The noise window has been used in order to compute the S/N ratio in the whole range of frequency. This information has been used for a first data selection: actually, only signals having an average signal to noise ratio greater than five have been considered in the spectral analysis. This operation has allowed to do a sort of quality control of the picking: if the picked first arrival is positioned much earlier than the actual P wave arrival, then the selected signal window contains also noise. In this conditions, the noise and signal spectral amplitudes will have comparable values. Similarly, if the pick is positioned long after the actual P wave arrival, noise window will contain, partially, also a signal contribution. In this case, this would give rise to a similarity between the noise and signal spectral amplitudes. (figure 3.5).

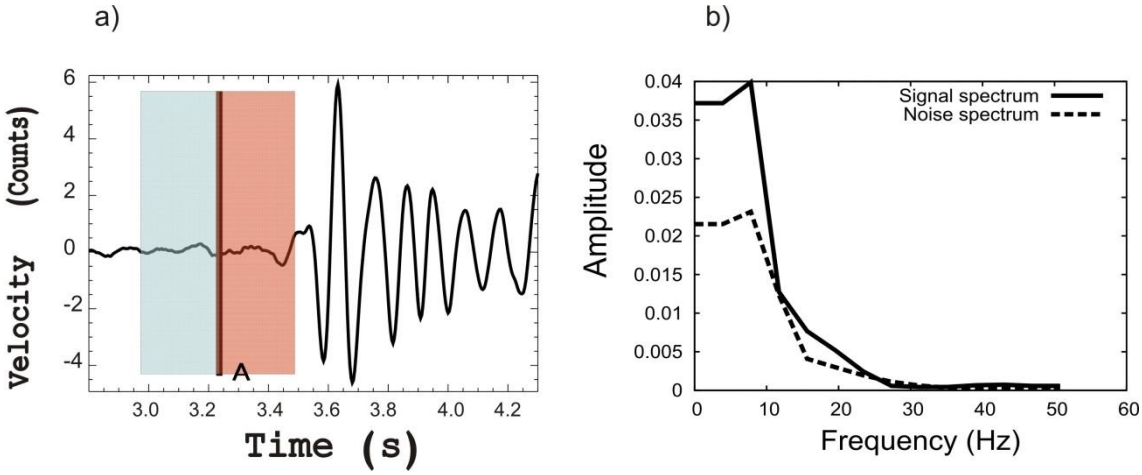

Figure 3.5 a) *Example of a trace in which the pick is positioned earlier than the actual P wave first arrival. The cyan area represents the window used to compute the noise spectrum; the red area, instead, highlights the window used to compute the signal spectrum.* ***b)*** *Signal and noise spectrum, represented by the solid and dashed line, respectively. Note that spectral amplitudes of noise and signal are not so different, and most of all their ratio is less than 5. It means that, in this way, traces for which the pick has not been conveniently positioned are discarded because of selection based on S/N ratio.*

Furthermore, through this selection criterion all intrinsically noisy traces have been discarded; this is important because it is well known that reliability of spectral ratio method is greatly affected by the noise.

In order to remove the elastic Green's function contribution affecting dt^* measurements, the deconvolution procedure described in the previous chapter has been applied.

To this purpose, Green's functions in a completely elastic medium in which Q_P is equal to 100,000 have been computed. The elastic properties are represented by the average 1D Battaglia et al. (2008) velocity model and by a density profile inferred from previous

literature works on Campi Flegrei caldera (Zamora et al., 1994; Berrino et al., 1998; Berrino et al., 2008) (figure 3.6). Next, the retrieved elastic Green's function are convolved for a 0.2 s duration triangular source. On the computed synthetic seismograms, the above described processing analysis has been applied. This consists of: 1) cut of the traces (0.248 s time window duration); 2) tapering of the selected time window (5% tapering window); 3) amplitude spectrum computation; 4) smoothing of the spectra (3 total width points average window).

Later, for each source-receiver couple, real amplitude spectra have been deconvolved for the corresponding synthetic amplitude spectra obtaining in that way the *reduced amplitude spectra* (cfr. paragraph 2.3).

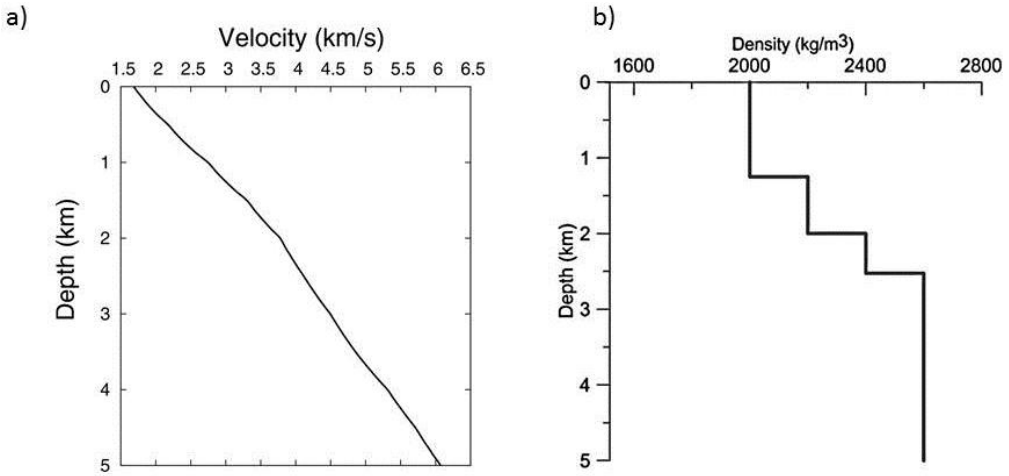

Figure 3.6. a) *Average 1D Battaglia et al. (2008) velocity model.* ***b)*** *Density profile inferred from previous literature works.*

3.3.2 The choice of the reference station

Next, the problem of the choice of the reference receiver has been faced. We remind you that the reference receiver is the station respect to which the spectral ratio is computed. Teng (1968) and Taylor et al. (1986), used a single reference station, stating (after an additional set of calculations) that its choice does not seem to affect the values of resulting data. Ponko and Sanders (1994), on the other hand, identified a virtual reference spectrum by averaging several spectra recorded from one event. This may be particular useful when, by looking at the spectral form, a strong dependency on station location is observable due to site effects.

In our case, we have followed a different criterion: for each source a different reference station has been chosen. In particular, the closest station to the source has been established to be the reference receiver. Actually, in some cases the closest recordings to the source have been discarded since their signals turned out to be saturated; for these shots, no spectral ratios have been computed. The histogram representing the distances of the reference stations from the source is shown in figure 3.7: the reference receivers mean distance from the source is equal to 587 m.

Our choice implies that the second receiver is always located at greater distances from the source than the reference one. For the sake of simplicity the second receiver will be called farther station, hereafter. If the investigated medium were homogenous in the anelastic properties our choice criterion of reference station would be reflected in all positive dt^* values; as we can see in the following, the three dimensional heterogeneity of the medium implies a more complex distribution of dt^* measurement.

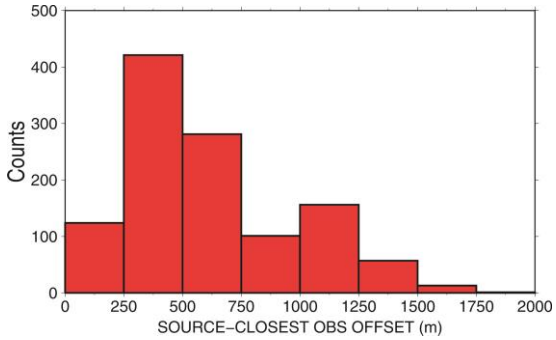

Figure 3.7 *Histogram representing the distribution of distances from the source of the reference receivers established in the spectral ratio analysis. The great percentage of reference receivers are at a distance between 250 and 750 m. The mean value of the "closest distances" is 521 m.*

3.3.3 Spectral ratio computation

Spectral ratios have been computed in a common source gather configuration. It means that, for every shot, the reduced amplitude spectra of the farther stations have been divided by the unique reference reduced amplitude spectrum.

In order to completely take into account the noise influence in dt^* measurements, spectral ratios have not been computed in the whole frequency range: actually, a very strong selection criterion has been applied. It consists of computing the spectral ratio only for those frequencies for which both amplitude spectra have a S/N ratio greater than five. In that way, "*holed spectral ratio*" (cfr. Tusa et al., 2006a; Tusa et al., 2006b) are obtained. This new term indicates a spectral ratio lacking spectral amplitude values at certain frequencies. In Tusa et al. (2006a, 2006b), a statistical study verified that to

deal with “holed spectrum” does not lead to significant differences in the estimates of spectral parameters.

In our case, no similar studies have been performed; on the other hand, we have seen that the percentage of discarded amplitude values is very low (less than 5% in the frequency range 10-20 Hz) up to 30 Hz and it starts to increase for greater frequencies.

The represented histogram gives also a clear indication about the frequency over which the noise starts to be important with respect to the signal amplitude: therefore, this analysis has provided information on the frequency range over which to fit the spectral ratio.

Prior to the fitting operation, a further correction has been applied. The primary concern of spectral ratio method is to detect a linear trend of the spectral ratios over a frequency range. For this reason it seems appropriate to achieve this goal by smoothing also the retrieved spectral ratios with a moving window with a total width of 3 points. Later, spectral ratios have been fitted in the sense of least-squares by means of an inversion algorithm implemented in the software package GNUPLOT (Janert, 2009). In order to take into account the influence on dt^* measurements of the frequency range over which spectral ratios are fitted, the least-squares regression has been carried out in 5-25 Hz, 5-30 Hz, 5-35 Hz frequency ranges (figure 3.8).

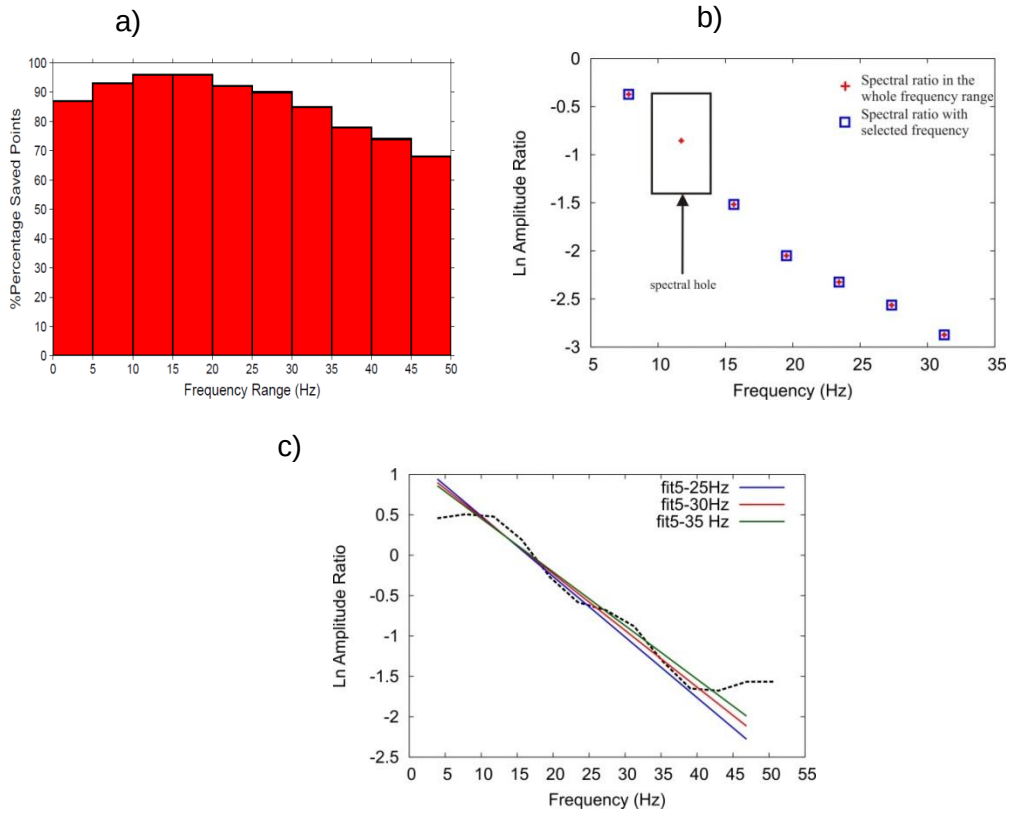

Figure 3.8. Previous page a) *Percentage of "saved points" in 5 Hz width bin after the application of selection frequency by frequency. In the frequency range 10-20 Hz the percentage of "lost points" is lower than 5%. At greater frequencies the noise contribution is more important and for this reason the percentage of "lost points" increases.* ***b)*** *Example of spectral hole in a computed spectral ratio. The red crosses represent the spectral ratio computed in the whole frequency range, the blue squares, instead, the spectral ratio computed after the application of selection frequency by frequency.* ***c)*** *Spectral ratio example (dashed line) which has been fitted in the range 5-25 Hz (blue solid line), 5-30 Hz (red solid line), 5-35 Hz (green solid line).*

3.3.4 dt* measurements selection

By applying the described spectral ratio computation, more than 26,000 dt* values have been measured. However, in order to select only data referring to spectral ratios having a truly linear trend a proper picking criterion has been elaborated.

The most appropriate parameter that may be used in order to select measured dt* on the basis of spectral ratios linearity is thought to be the linear correlation coefficient **R**. The threshold that we have considered below which to discard dt* values is |**R**|=0.95. We have considered the absolute value in order to possibly include also negative dt* values. Actually, even considering very close to the source reference receivers, a negative dt* value may be possible. As a matter of fact, in the very simple condition of a propagation medium described by figure 3.9,

$$dt^* < 0 \Rightarrow \frac{T_2}{Q_2} - \frac{T_1}{Q_1} \Rightarrow \frac{T_2}{Q_2}\left(1 - \frac{T_1}{Q_1}\frac{Q_2}{T_2}\right) < 0 .$$

Since T_2/Q_2 is always greater than zero, it follows that $\left(1 - \frac{T_1}{Q_1}\frac{Q_2}{T_2}\right) < 0$ if

$$1 < \frac{T_1}{T_2}\frac{Q_2}{Q_1} \Rightarrow \frac{T_2}{T_1} < \frac{Q_2}{Q_1} .$$

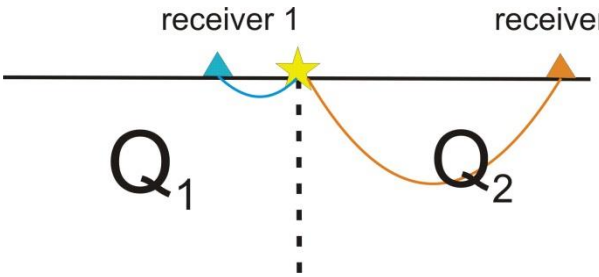

Figure 3.9 *Simple scheme describing a horizontal heterogeneity in the attenuating structure. In such situation, a negative dt* value is possible. The triangles represent the receivers, whereas the star represent the seismic shallow source.*

The condition expressed by the last inequality is a real possibility, especially for short distances for which T_2 is comparable to T_1.

Unfortunately, a selection criterion based only on the linear correlation coefficient value is not recommended for our purposes. Indeed, in that way a band of dt^* values very close to zero, both positive and negative, will be automatically discarded. In that way a discontinuous dt^* distribution is obtained. As a matter of fact, a point distribution approximated by a low slope best fit line (corresponding to a very close to zero dt^* value) will have a |R| value that only in the best cases will be sufficiently high (figure 3.10). In fact, for example, let us fix a dispersion coefficient of points around a best fit line. Let us consider a dispersion coefficient of points which, with a slope of the best fit line of 0.01, corresponds to a |R| coefficient equal to 0.98. By decreasing the slope to a quantity equal to 0.001, with the same value of the dispersion coefficient, |R| will be equal to 0.65. It means that, in order to have a greater |R|, the dispersion coefficient value has to decrease. Therefore, the points must be almost perfectly aligned.

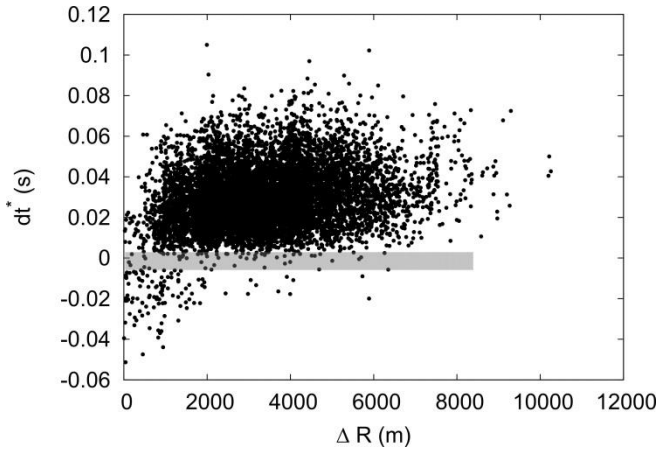

Figure 3.10 *Final dt^* distribution retrieved by fitting spectral ratios in the frequency range 5-25 Hz and by selecting them only based on linear correlation coefficient |R| >0.95. The lightened grey area highlighrt the discontinuous dt^* distribution and the band of dt* almost completely lacking of measurements.*

For this reason, the following three step procedure has been followed:

1) all spectral ratios having |R| > 0.95 have been selected;
2) the variance of residuals between the selected spectral ratios and their best fit lines has been computed;
3) the mean value of variance of residuals has been computed;
4) spectral ratios (and the respective dt^* estimates) having a variance of residuals value lower than the mean value previously computed are selected.

By applying this criterion to spectral ratios fitted in the frequency range 5-25 Hz, a final dt^* dataset consisting of 14,450 measurements has been built (figure 3.11). The 9% of the total dataset is constituted by negative dt^*. Negative values disappear for greater ΔR

values (ray lengths differences are relative to ray paths computed in the average 1D Battaglia et al., (2008) velocity model). This aspect is reasonable. In fact, it means that, for ΔR greater than about 4 km, the differences between travel times of reference receiver and farther station affect data distribution more than the possible effects linked to heterogeneity in the attenuating structure.

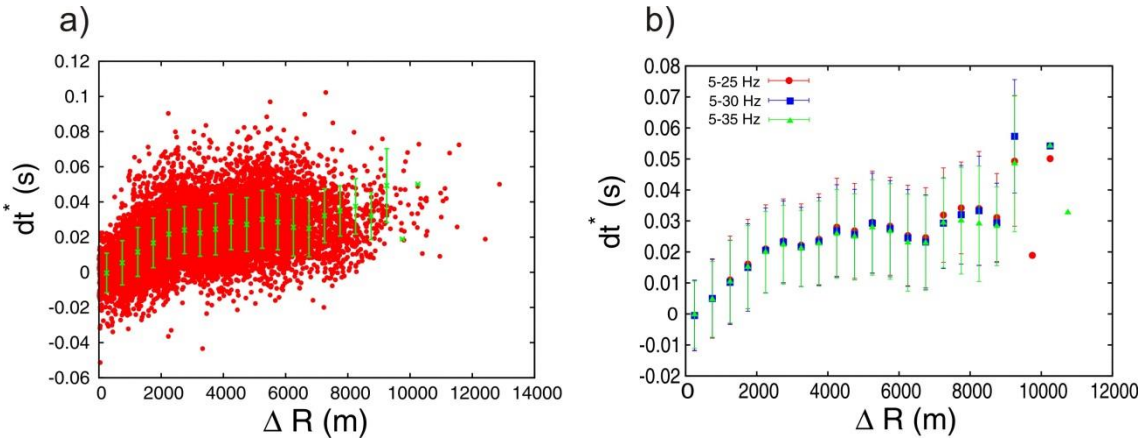

Figure 3.11 a) *Final dt* distribution consisting in 14,450 data computed by fitting spectral ratios in the frequency range 5-25 Hz. The green points represent the dt* mean values computed in ΔR ranges of 500 m, with the associated error bar describing the dispersion around the dt* mean value. Note that ΔR distribution increases with the distance up to about 4 km; for greater ΔR values the dt* trend remains constant.* ***b)*** *Distribution of dt* values measured by fitting spectral ratios in different frequency ranges, that is 5-25 Hz, 5-30 Hz, 5-35 Hz, indicated with red, blue and green colour, respectively. Note the complete overlapping between measured dt* in three different frequency ranges.*

By comparing the mean dt* distributions retrieved by fitting spectral ratios in 5-25 Hz, 5-30 Hz, 5-35 Hz frequency ranges, we can see that there are no meaningful differences: therefore we can conclude that the frequency interval on which spectral ratio method has been applied does not influence the final dt* distribution.

CHAPTER 4

Tomographic inversion procedure and synthetic tests

4.1 Introduction

"The use of differential times for determining relative locations of earthquakes has been a fruitful field of work for many decades (e.g. Douglas, 1967)"(Thurber et al., 2007). A lot of studies (e.g. Got et al., 1994; Rubin et al., 1998; Waldhauser et al., 1999) have confirmed the improvement that can be achieved in earthquake location due to the use of differential travel time measurements.

These successes inspired efforts to incorporate differential times in seismic tomography, which realized in Zhang and Thurber (2003, 2005) and Zhang et al. (2004) double difference algorithm.

A very similar approach has been followed in our case, in order to manage differential t^* measurements. Teng (1968) had already proposed a mathematical formulation to retrieve a 1D model from dt^* measurements.

In this chapter, the mathematics of the method used to extract information from the differential attenuation data will be described, as well as the general principles of the attenuation tomographic problem. Furthermore, a general description of the inversion code TOMO_TV will be provided. Finally, in order to check the reliability of the tomographic method and its applicability to real dt^* dataset synthetic tests have been performed. The characteristics and respective results of two synthetic tests will be described.

4.2 Principles of tomographic problem

In seismology, tomography is an inverse problem; it is a technique that uses informations contained in seismic records (data) to infer 2D or 3D models of the Earth

interior.

An inverse problem (Menke, 1984) can be easily described by the relation

$$\overline{d} = G\overline{m}, \tag{4.1}$$

where the term ***d*** represents the data vector of dimension N, whereas the vector ***m*** represents the model parameters vector having dimension M; the vector of model parameters constitutes the unknown of the inverse problem. The term **G** represents a matrix of dimension NxM and it is called the ***data kernel***: it defines the existing mathematical relations between data and model parameters vectors.

4.2.1 The attenuation tomography

Generally, in seismic tomography data are constituted by the travel times recorded by receivers located in different places in the investigation area. The model parameters, on the other hand, are the velocity values at which elastic waves propagate through the Earth.

In the case of the attenuation tomography, instead, the data are represented by t^* values measured from seismic traces. The parameters vector is constituted by the attenuation values: they are either Q_P or Q_S, or both of them, depending on the analysed seismic phase. For the sake of convenience we recall t^* definition here:

$$t^*_{i,j} = \int_{ray} \frac{ds}{Q(s)V(s)}. \tag{4.2}$$

We remind that it represents the accumulated Q^{-1} along the ray path connecting the source with the receiver. The indexes *i* and *j* represent the source and station index, respectively.

The relation (4.2) can be rewritten in terms of the reciprocal of the velocity, that is the slowness parameter *u*, and in terms of the reciprocal of quality factor, that is the parameter η:

$$t^*_{i,j} = \int_{ray} u(s)\eta(s)ds. \tag{4.3}$$

It means that

$$t^*_{i,j} = f(u, \eta, x_0, x_s); \tag{4.4}$$

the terms x_0 and x_s represent the ipocentral coordinates and the position of the station, respectively.

To retrieve the attenuation model which better fits the measured data means to find that model which reduces the misfit (i.e. the root mean square of residuals) between observed and theoretical data. Hereafter measured data will be defined with the notation $\boldsymbol{t^{*obs}}$, whereas theoretical data will be defined with the notation $\boldsymbol{t^{*theo}}$. The latter may be computed exploiting relation (4.3) which represents the solution of the forward problem for the tomographic method. In an attenuation tomography problem the computation of t^* theoretical values requires the a-priori knowledge of the couple-source position and, most of all, the ray path depending on velocity model. Furthermore, an ***initial attenuation model*** must be provided. More details on the way through which this computation is performed will be provided in the paragraph 4.4.

By linearizing the function (4.4) by means of a first order Taylor's series expansion, a different and most useful expression of the residuals between observed and theoretical (or predicted) data, $r_{i,j} = t_{i,j}^{*OBS} - t_{i,j}^{*THEO}$, can be achieved. Indeed

$$t_{i,j}^{*}(\eta) = t_{i,j}^{*}(\eta_0) + \left.\frac{\partial t^*}{\partial u(x,y,z)}\right|_{u=u0} \Delta u(x,y,z) + \left.\frac{\partial t^*}{\partial \eta(x,y,z)}\right|_{\eta=\eta_0} \Delta\eta(x,y,z) + \left.\frac{\partial t^*}{\partial x_0}\right|_{x0=x0^*} \Delta x_0 + R. \quad (4.5)$$

The terms u_0 and η_0 represent the parameters of the velocity model and of the initial attenuation model, respectively. The quantities Δu and $\Delta\eta$ are the perturbations with respect to the initial models. Similarly, the quantities x_0^* and Δx_0 describe the initial location of earthquakes and the perturbations with respect to ipocentral coordinates, respectively.

Since in the attenuation tomographic problem sources position is a-priori established, and also the velocity model is assumed to be known (it does not change during the inversion procedure), the quantities Δu and Δx_0 are equal to 0. Therefore, equation (4.5) will take the form:

$$t_{i,j}^{*}(\eta) = t_{i,j}^{*}(\eta_0) + \left.\frac{\partial t^*}{\partial \eta(x,y,z)}\right|_{\eta=\eta_0} \Delta\eta(x,y,z) + R \quad (4.6)$$

The hypothesis on which the linearization process of the quantity t^* is based is that the initial attenuation model is close to the actual and unknown one. Then, by perturbating it, we can retrieve a final model that minimizes the residuals. These, based on relation (4.6), can be expressed as

$$t_{i,j}^{*OBS} - t_{i,j}^{*THEO} = t_{i,j}^{*}(\eta) - t_{i,j}^{*}(\eta_0) = \delta t_{i,j}^{\ *} \approx \left.\frac{\partial t_{i,j}^{\ *}}{\partial \eta(x,y,z)}\right|_{\eta=\eta_0} \Delta\eta(x,y,z)\,. \qquad (4.7)$$

Equation (4.7) is a linear relation which connects the t^* residuals to perturbations to the initial attenuation model: therefore, its choice can greatly affect the retrieved final model: it is the greatest limit of all linearized tomographic problems.

In terms of the inverse problem, differently from what we have said before, the residuals $\delta t_{i,j}^{\ *}$ between observed and theoretical t^* represent the data; the perturbations $\Delta\eta$ respect to the initial model constitute the parameters.

The partial derivatives appearing in the equation (4.7), taking into account the t^* definition of equation (4.3), can be written as

$$\frac{\partial t_{i,j}^{\ *}}{\partial \eta(x,y,z)} = \int_{ray} u(x,y,z)dl\,. \qquad (4.8)$$

4.2.2 Representation of the velocity and attenuation structure and formulation of the attenuation tomography problem.

The computation of the integral in equation (4.8), as well as the one appearing in the t^* definition (equation 4.3), is analytically possible only in very simple earth model in which both u and η are "continuous, monotonic and only depth dependent functions" (Zollo and Emolo, 2011). In the most part of applications of tomographic method, then, the above mentioned integral is solved through numerical techniques. They are generally based on a simplified description of the propagation medium. Actually, the Earth's seismic velocity and attenuation structure has been represented in a wide variety of ways in seismic tomographic studies.

Two big classes can be defined speaking about the model parameterization: regular and irregular parameterization (Rawlinson et al., 2010). The former is usually simple and easy to formulate: cells or blocks with uniform seismic properties (velocity or

attenuation) are the most basic form of parameterizations, but the artificial discontinuities between each block are unrealistic. An alternative to block parameterization is to define seismic properties at the vertices of a regular grid. One of the first implementation of this approach was by Thurber (1983): he used a trilinear interpolation between a rectangular grid of nodes to define a continuously varying velocity field for Local Earthquake Tomography (LET).

The irregular parameterization, instead, allows to take into account the heterogeneity in the spatial ray coverage in the subsurface; it is principally due to the distribution of sources and stations. In particular this kind of parameterization "allows local smoothing scale lengths to vary spatially, and are in principle similar to the more recent commonly used variable mesh schemes" (Rawlinson et al., 2010). An example is constituted by the "continuous regionalization" developed by Montagner and Nataf (1986), that is commonly used in surface wave tomography.

The used tomographic inversion code defines the propagation medium by means of a tridimensional grid of nodes similar to that introduced by Thurber (1983) and above described. In particular, at each node of the grid (defined by the indexes triad *l,n,p*) a value of velocity and attenuation is assigned. Through an interpolation function $h_{l,n,p}$ a continuously varying velocity and attenuation field is retrieved. In particular, the interpolation function is equal to one in correspondence to the node *l,n,p* and equal to zero at the other nodes. Then, the attenuation perturbation field may be expressed by:

$$\Delta n(x,y,z) = \sum_{cube} \Delta\eta(l,n,p) h_{l,n,p} \ , \tag{4.9}$$

so that

$$\frac{\partial t_{i,j}^{\ *}}{\partial \eta(x,y,z)} = \sum_{cube} \frac{\partial t_{i,j}^{*}}{\partial \eta_{l,n,p}} \frac{1}{h_{l,n,p}} ; \tag{4.10}$$

therefore, taking into account the above equations, relation (4.7) will take the form

$$\delta t_{i,j}^{*} = \sum_{cube} \frac{\partial t_{i,j}^{*}}{\partial \eta_{l,n,p}} \Delta\eta_{l,n,p} \ . \tag{4.11}$$

The partial derivatives of t^* respect to the parameters of the tomographic problem (the attenuation values at the grid nodes), already defined in the equation (4.8), are now expressed as follows:

$$\frac{\partial t_{i,j}^{*}}{\partial \eta(l,n,p)} = \int_{ray} u(l,n,p) h_{l,n,p}\, dl \qquad . \tag{4.12}$$

Then, the equation (4.11) can be written in the common form of an inverse problem:

$$\delta t^{*} = G\Delta\eta \,. \tag{4.13}$$

Let us consider an attenuation tomographic problem with N_1 sources generating signals recorded by N_2 stations (N_1xN_2 = N data). By parameterizing the investigated medium in a 3D tomographic grid described by M nodes (the parameters to be determined), the resulting system of equations (4.13) can be written in the matrix form:

$$\begin{Vmatrix} \delta t_{1,1}^{*} \\ .... \\ .... \\ .... \\ .... \\ \delta t_{n1,n2}^{*} \end{Vmatrix} = \begin{Vmatrix} \frac{\partial t_{1,1}^{*}}{\partial \eta_1} & & \frac{\partial t_{1,n2}^{*}}{\partial \eta_m} \\ & \cdots\cdots\cdots\cdots & \\ \frac{\partial t_{n1,1}^{*}}{\partial \eta_1} & & \frac{\partial t_{n1,n2}^{*}}{\partial \eta_m} \end{Vmatrix} \begin{Vmatrix} \delta\eta_1 \\ .... \\ .... \\ .... \\ .... \\ \delta\eta_M \end{Vmatrix} \qquad . \tag{4.14}$$

4.2.3 The formulation of the attenuation tomographic problem for differential attenuation measurements.

In this paragraph the principles of tomographic inversion method developed to treat differential attenuation measurements are described. As said in the introduction, a similar approach to that by Teng (1968) and Zhang and Thurber (2003) has been followed.

For a single source and a set of receivers (*j* the closest one to the source, i=1,N the remaining stations), measured data are represented by the vector

$$\left\| dt_1^{*} .....dt_n^{*} \right\|^{T} \tag{4.15}$$

where

$$dt_1^{*} = t_1^{*} - t_j^{*} \tag{4.16}$$

and

$$dt_n^* = t_n^* - t_j^* . \tag{4.17}$$

For sake of simplicity, let us develop the problem only for the quantity dt_1^*.

With fixed velocity and attenuation models, theoretical dt_1^{*THEO} value may be obtained. It will differ from the observed dt_1^{*OBS} of a quantity

$$\Delta dt^*_1 = \left(t_1^* - t_j^*\right)^{OBS} - \left(t_1^* - t_j^*\right)^{THEO}, \tag{4.18}$$

in which the quantity Δdt^*_1 is the "double-difference" (Waldhauser and Ellsworth, 2000).

The above equation can be written as

$$\Delta dt^*_1 = \left(t_1^{*OBS} - t_1^{*THEO}\right) - \left(t_j^{*OBS} - t_j^{*THEO}\right), \tag{4.19}$$

where each term in brackets represents the residuals between measured and theoretical t^* in an initial velocity and attenuation model (we have previously defined this quantity δt^*).

From equation (4.11)

$$\delta t_i^* = \sum_{cube} \frac{\partial t^*_i}{\partial \eta_{l,n,p}} \Delta \eta_{l,n,p} . \tag{4.20}$$

In the above equation, the subscript *i* represents the receiver index.

Therefore, taking into account the above equation, the (4.19) will take the form

$$\Delta dt_1^* = \delta t_1^* - \delta t_j^* = \sum_{cube} \frac{\partial t_1^*}{\partial \eta_{l,n,p}} \Delta \eta_{l,n,p} - \sum_{cube} \frac{\partial t_j^*}{\partial \eta_{l,n,p}} \Delta \eta_{l,n,p} . \tag{4.21}$$

Let us assume to have a single source attenuation tomographic problem, for which seismic signals have been recorded by N stations. Parameterizing the investigated medium in a 3D tomographic grid described by M nodes, which constitute the M parameters to be determined, the resulting system of equations could be written in a matrix form:

$$\begin{Vmatrix} \Delta dt_1^* \\ .... \\ .... \\ .... \\ .... \\ \Delta dt_n^* \end{Vmatrix} = \begin{Vmatrix} \frac{\partial t_1^{*1}}{\partial \eta_1} - \frac{\partial t_j^{*1}}{\partial \eta_1} & & \frac{\partial t_1^{*m}}{\partial \eta_m} - \frac{\partial t_j^{*m}}{\partial \eta_m} \\ & ..... & \\ \frac{\partial t_n^{*1}}{\partial \eta_1} - \frac{\partial t_j^{*1}}{\partial \eta_1} & & \frac{\partial t_n^{*m}}{\partial \eta_m} - \frac{\partial t_j^{*m}}{\partial \eta_m} \end{Vmatrix} \begin{Vmatrix} \Delta \eta_1 \\ .... \\ .... \\ .... \\ .... \\ \Delta \eta_m \end{Vmatrix}. \quad (4.22)$$

The equation (4.22) is a typical inverse problem equation d= Gm, in which ***d*** represents the data vector and is constituted by the residuals between measured and theoretical dt^*, and ***m*** the vector of parameters constituted by the perturbations $\Delta\eta$ to the initial attenuation model. The data kernel ***G*** is constituted by the differences between two quantities. They are the partial derivatives of t^* relative to two different receivers with respect to the parameters of the tomographic problem, that are the nodes of the inversion grid. Therefore, the above equation can be expressed in the compact form

$$\Delta dt^* = G\Delta\eta. \quad (4.23)$$

Figure 4.1 shows how differences between partial derivatives are computed.

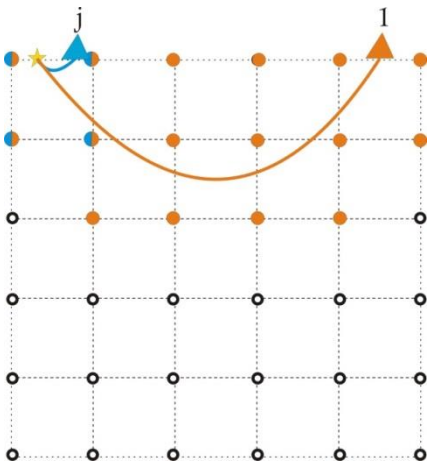

Figure 4.1: *2D representation of the tomographic inversion grid. The yellow star represents the source, the cyan triangle identifies the reference station, whereas the orange triangle represents the farther receiver. The quantities t^*_j and t^*_1 are the t* values of the above introduced stations, respectively. Therefore, in this simple example, the differential attenuation measurement dt^* is equal to t^*_1-t^*_j. The orange grid nodes are the vertices of the cells crossed only by the ray corresponding to the quantity t^*_1. Since the ray corresponding to the quantity t^*_j does not cross these cells, the partial derivatives of this quantity with respect to orange nodes are equal to zero (cfr. equation 4.12). The grid nodes half orange and half cyan are instead the vertices of the cell crossed both by t^*_1 ray and by t^*_j ray. In this case, both partial derivatives of t^*_1 quantity and of t^*_j quantity with respect to these parameters will be different from zero. Therefore, a difference between the respective values of partial derivatives will be computed.*

4.3 The inversion method

Tomography, no matter if velocity or attenuation one, is a mixed-determined inverse problem. It means that, even if the number of data is greater than the number of

unknowns, some parameters are completely undetermined, so that it is impossible to infer their values. This may be caused by the ray coverage. In order to be clear as much as possible, let us imagine a tomographic problem in which the medium is discretized by means of boxes. It may happen that there is a cell through which several rays pass. The slowness (or attenuation) value of this parameter is clearly overdetermined. "On the other hand, there may be boxes that have been entirely missed. These boxes are completely undetermined" (Menke, 1984). It means that, in order to solve the mixed determined problem, we should add other informations not contained in the equation **Gm=d**, that are the a-priori informations. Usually, in a linearized tomography problem, the a-priori informations consist in requiring that the final model is not so far from the initial one. A further condition can be implemented, that is to obtain a final model showing smooth variations of the parameters values along the three directions.

Therefore, the necessity to search for a model which both minimizes the misfit function and meets a-priori requirements has to be fulfilled. This is usually done by searching for a solution in the sense of *damped-least squares* (Menke, 1984). In this way, the undetermined problem is said to have been damped. Mathematically, the quantity to be minimized is

$$\phi(m) = (d - Gm)^T (d - Gm) + \varepsilon^2 (m - m_0)^T (m - m_0) + \eta m^T D^T D m . \qquad (4.24)$$

In the above equation, two weighting factor ε^2 and η (this is different from the reciprocal of quality factor before introduced) are present: they are the damping and smoothing parameter, respectively. The term m_0 represents the vector of initial model parameters, whereas the term D represents the second derivative smoothing operator. By minimizing the function $\phi(m)$ with respect to the model parameters in a manner exactly analogous to the least squares derivation, we obtain the estimate of model parameters:

$$m^{est} = \left(G^T G + \varepsilon^2 I + \eta D^T D\right)^{-1} G^T d \quad . \qquad (4.25)$$

4.3.1 Damping and smoothing parameter

The damping and smoothing parameter determine, respectively, the relative importance given during the inversion

1) to the closeness of the final model to the initial one;

2) to the smoothness of the final solution, respectively.

The values given to these parameters are reflected also on the importance given to the minimization of the misfit function. Therefore, if ε^2 and η are too large, the inversion procedure will minimize the undetermined part of the solution, but, as a result, the retrieved model will not minimize the misfit function. On the other hand, if ε^2 and η are set to zero, the misfit function will be minimized, but no a priori information will be provided to single out the undetermined model parameters.

From a practical point of view, damping tends to decrease the amplitude of perturbations to the initial model without filtering the final tomographic image. The smoothing essentialy acts as a low pass filter. It means that, when minimal smoothing and damping are used, the recovered tomographic image contains numerous short wavelength artifacts (Rawlinson et al., 2010). In order to impose the final solution to be smooth, the solution roughness should be minimized by imposing that the Laplacian of the attenuation field (represented by η, the reciprocal of Q) is zero (Benz et al., 1996).

In order to choose the "optimum" damping parameter "several one-step inversions were run with different damping values" (Eberhart-Philipps, 1986). Then, by plotting the resulting trade-off curve between the data fit and model perturbation, the damping value in correspondence of the elbow of the curve will indicate the best trade-off parameter. Actually, it will represent the value which reduces the data misfit with a moderate increase in the model perturbation.

A similar procedure is followed to choose the proper smoothing parameter. In this case the trade-off curve between data fit and model roughness obtained by running several one-step inversions with different smoothing values is studied. The choice criterion is the same of the one indicated for the damping parameter. The model roughness, as said before, is directly linked to the second derivatives of the attenuation field. In particular, in our case the roughness formulation proposed by Hobro et al. (2003) has been used, that is:

$$\|m\|_{MV}^2 = V^{1/3}\int_V \left(\frac{\partial^2 m}{\partial x^2}\right)^2 + \left(\frac{\partial^2 m}{\partial y^2}\right)^2 + \left(\frac{\partial^2 m}{\partial z^2}\right)^2 + 2\left(\frac{\partial^2 m}{\partial x \partial y}\right)^2 + 2\left(\frac{\partial^2 m}{\partial y \partial z}\right)^2 + 2\left(\frac{\partial^2 m}{\partial x \partial z}\right)^2 dV \quad . \tag{4.26}$$

The second derivatives are expressed by using the finite-differences operators:

$$\left(\frac{\partial^2 m}{\partial x^2}\right) = \frac{1}{\Delta x^2}\left(m_{i-1,j} - 2m_{i,j} + m_{i+1,j}\right) \tag{4.27}$$

and

$$\left(\frac{\partial^2 m}{\partial x \partial y}\right) = \frac{1}{\Delta x \Delta y}\left(m_{i-1,j-1} - m_{i+1,j-1} - m_{i-1,j+1} + m_{i+1,j+1}\right). \tag{4.28}$$

In the above equations the quantities $m_{i,j}$ represent the values of the parameters at grid index *(i,j)*, whereas Δx and Δy represent the parameters separation along *x* and *y* direction, respectively. The quantity *V* outside the integral, instead, represents the volume of the model whose roughness has to be computed.

Since both damping and smoothing parameter contribute to regularize the inverse problem, there may be a trade-off also between them. A procedure to overcome this problem and to uniquely determine the best combination of regularization parameters in the inversion problem does exist. It has been introduced by Rawlinson et al. (2006) and will be completely described in the next chapter, where the application of the tomographic procedure to real data will be shown.

4.4 Description of the tomographic procedure

We have used a "linearized, iterative tomographic approach as proposed by many authors (e.g Spakman and Nolet, 1988; Aster and Mayer, 1988; Hole et al., 2000; Benz et al., 1996; Le Meur et al., 1997; Latorre et al., 2004)" (Vanorio et al., 2005).

The tomographic inversion code TOMO_TV, developed by prof. Jean Virieux of the University Joseph Fourier in Grenoble, has been used in this thesis work. During the PhD thesis it has been modified twice: the first step consisted in adapting it in order to invert t^* measurements. These modifications have been made by some components of RISSCLab team – Unità di ricerca in Sismologia sperimentale e computazionale of University of Naples Federico II. The reliability of the code (renamed TOMO_Q) has been verified by means of synthetic tests carried out by me. The second step, instead, consisted in the modification of the inversion code in order to manage differential attenuation measurements. Also in this case a robust code validation phase was necessary. Only two synthetic tests carried out to this purpose will be shown in the next paragraph.

The inversion procedure consists in the following operations:

1) trilinear interpolation of the velocity model in a finer grid than the tomographic one;
2) ray tracing through Podvin and Lecomte (1991) algorithm;
3) computation of t^* by the integration of the quantity $u\eta$ (slowness times the reciprocal of Q; cfr. equation 4.3) along the ray path; after that, the dt^* are obtained through the computation of differences between the corresponding t^* values;
4) computation of the differences of partial derivatives of t^* with respect to the parameters of the tomographic problem;
5) smoothing of the matrix of derivatives by imposing that the Laplacian of the attenuation field must vanish;
6) inversion of linear system of equations (4.23) by means of LSQR algorithm (Paige and Saunders, 1982); the inversion is regularized by means of the damping parameter properly chosen.

Since the velocity model during this inversion procedure does not change, the 1^{st}, 2^{nd} and 4^{th} steps are executed only once. Actually, the first step is necessary for the ray tracing which depends only on the velocity model. The matrix of derivatives depend only on the velocity model, too (cfr. equation 4.12 e 4.22).

4.5 Validation of the code and of tomographic procedure: synthetic tests.

A lot of synthetic tests have been carried out in order to validate the inversion code after modifications brought to it. For the sake of brevity, only two of them will be described.

Synthetic test 1

The first test that will be shown was aimed to be sure about the running of the code in an overdetermined problem. In this test sources and stations were placed in the proper positions in order to guarantee the complete enlightenment by the ray of the propagation medium.

A tomographic grid of dimensions 10 x 10 x 6 km^3, with a grid spacing of 1 x 1 x 1 km^3 has been created. In a homogeneous medium, both in elastic and anelastic properties (Vp=6 km/s; Qp=500), an annular low Qp anomaly (Qp=100) is placed at depth

between 2 and 4 km. Stations are located both at the surface and in depth around the anomaly. Sources, instead, are placed under the anomaly, (5 km deep), and on the borders of the anomaly (figure 4.2a). Synthetic dt^* are computed by considering as the reference receiver, for each source, the closest station to the shot (figure 4.2c).

With a starting homogeneous attenuation model, Qp=300, a tomographic inversion has been run which has produced the results shown in figure 4.2(f-e). The final tomographic model at the third iteration has been represented in terms of percentage error, both in the plane and in the section view. The errors are less than 5%, except for those limited area (both in number and in size) for which there is a very poor ray coverage. Actually, higher error zones (percentage error about 50%) are in the more external parts of the tomographic model, approximately at the corner of the inversion grid.

Synthetic test 2

The second test was aimed to show the applicability of the tomographic inversion method with a real sources-stations configuration. In particular, the configuration corresponding to the 14,450 measured and selected dt^* from SERAPIS dataset has been considered (cfr paragraph 3.3.4, chapter 3). Seismic rays have been traced in a tomographic grid of dimensions 13 x 13 x 5 km^3, with a grid spacing of 500 x 500 x 250 m^3. The chosen velocity model is the average 1D Battaglia et al. (2008) one. Synthetic dt^* (represented in figure 4.3) have been computed in the over mentioned velocity model and in an attenuation model very similar to the previous synthetic test one: a low Qp annular anomaly (Qp=100) is located at depth between 0.5 km and 1.5 km in a homogeneous attenuation medium (Qp=500). The choice of the annular anomaly is linked to one of the most interesting and significant features emerging from previous geophysical studies and surface geological evidences (Rosi and Sbrana, 1987) in the Campi Flegrei area. Actually, gravimetric (Capuano and Achauer, 2003; Capuano et al, 2013) and tomographic images (Zollo et al., 2003; Judenherc and Zollo, 2004; Battaglia et al., 2008) show a positive density and velocity annular anomaly, identified as the buried rim of the Campi Flegrei caldera.

With a starting homogeneous attenuation model, Qp=300, a tomographic inversion has been run which has produced the results shown in figure 4.4. For this test, the inversion convergence is lightly slower than the previous test; therefore, the results at the eighth iteration are represented in figure 4.5, both in terms of Q absolute values and in terms of

percentage error. The attenuation anomaly is fully recovered from a geometrical point of view. At greater depths (1.25 km and 1.5 km) higher percentage errors are visible (about 40-50 %) around the annular anomaly because of the poor ray coverage at that depth.

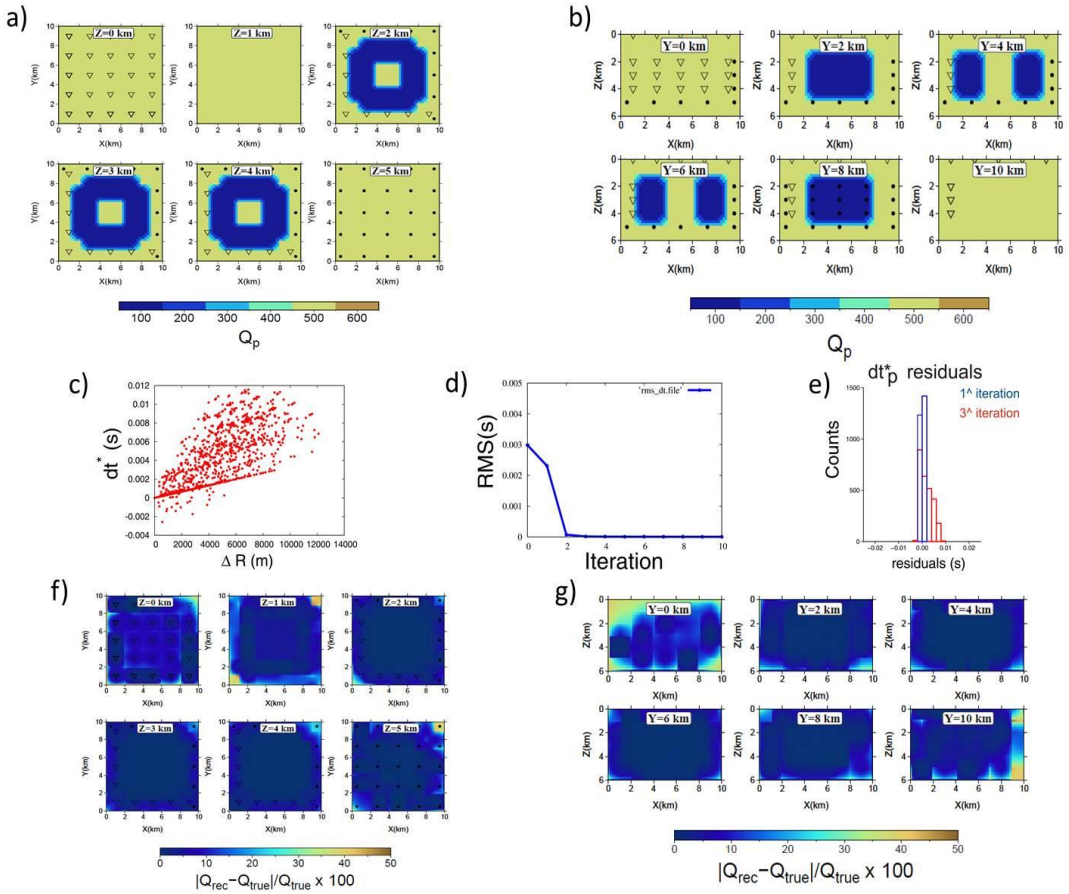

Figure 4.2 a) *True attenuation model of test 1: plane view. The triangles represent the stations, the black points the sources.* ***b)*** *True attenuation model of test 1: section view.* ***c)*** *Synthetic dt* computed in the attenuation model represented by previous figures and in a homogeneous velocity model (Vp=6 km/s).* ***d)*** *Rms vs number of iterations. A complete convergence of the solution is achieved after three iterations.* ***e)*** *Residuals at the first iteration (red histogram) and residuals at the third iteration (blue histogram).* ***f)*** *Final tomographic results at different depths represented in terms of the percentage error (plane view).* ***g)*** *Final tomographic results represented in terms of percentage error (section view).*

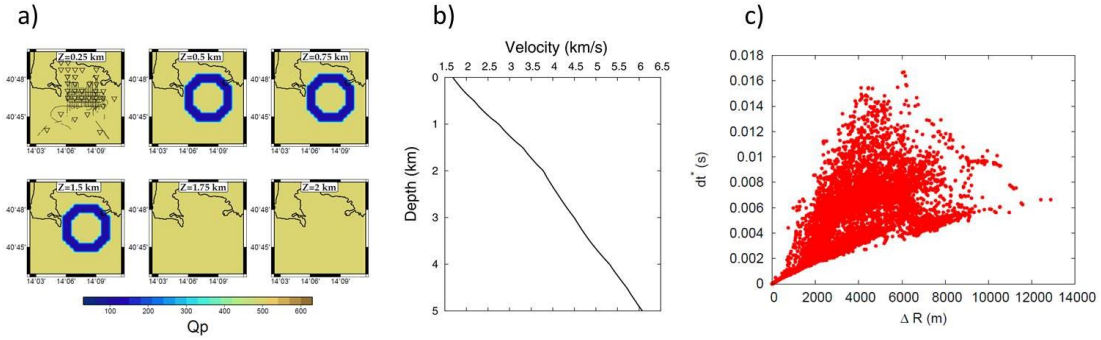

Figure 4.3 a) *True attenuation model of test 2. The triangles represent the stations, the black points the sources: they are positioned at a depth between 0 km and 0.25 km.* ***b)*** *Average 1D Battaglia et al. (2008) velocity model.* ***c)*** *Synthetic dt^* computed in the attenuation model represented by figure a) and in the velocity model represented by figure b.*

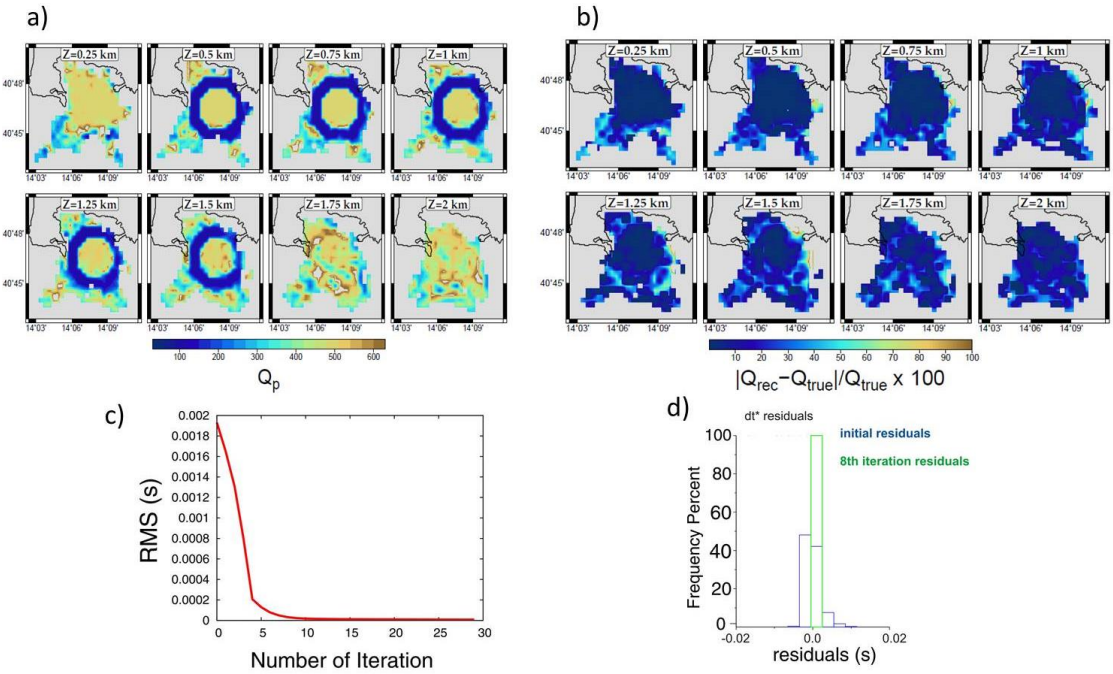

Figure 4.4 a) *Tomographic images at different depths retrieved after 8 iterations. Grey regions represent areas not covered by rays.* ***b)*** *Tomographic results, after 8 iterations, expressed in terms of percentage error. Grey regions represent areas not covered by rays.* ***c)*** *RMS vs number of iterations. A complete convergence of the solution is achieved after 8 iterations.* ***d)*** *Residuals at the first iteration (blue histogram) and residuals at the eight iteration (green histogram).*

CHAPTER 5

The attenuation tomography of Campi Flegrei caldera, Southern Italy.

5.1 Introduction

Campi Flegrei is a volcanic polygenetic complex located along the western coast of Southern Italy, 15 km west of Naples (de Natale et al., 1987). It covers an area of approximately 400 km^2 and it is one of the two active volcanic system in the south of Italy (figure 5.1). From a structural point of view, it is located in the southern part of the Plio-Quaternary Campanian Plain. It is a graben-like structure located at the eastern margin of the Tyrrhenian Sea. In this area, a lithospheric thinning is observed because of an extensional tectonic. It is linked to the rollback of the subducting Apulian-Ionian plate in the south-east direction (Faccenna et al., 1996). Besides the crustal thinning, the Campanian Plain shows typical features of an extensional area: normal faults (Milia and Torrente, 1997), high heat flow (Della Vedova et al., 2001), crustal magma reservoirs and high-K and normal-K volcanic rocks. Due to these characteristics, in Campanian Plain other volcanic systems are present (i.e. Ischia, Procida, and Somma-Vesuvius) (De Martino et al., 2014).

Campi Flegrei in the past: the eruptive history

The great volcanological interest in Campi Flegrei is linked to the associated high risk. Actually, Campi Flegrei are characterized by an explosive character. Furthermore, 1.5 million people live within the entire caldera, with about 350,000 in its active portion (Di Renzo et al, 2011; Capuano et al., 2013).

From a geomorphological point of view, Campi Flegrei volcanic field is a partly submerged nested calderic system. Its current shape is directly linked to its eruptive history. The oldest dated volcanic unit has an age of about 60,000 years and it is related

to a volcanism outside the borders of the current calderic system (Pappalardo et al., 1999, Di Renzo et al, 2011). However, the greatest eruptive events occurred about 35,000 and 15,000 years ago and are the main causes of the current configuration of the caldera.

The most significative eruptive event is represented by the Campanian Ignimbrite eruption (CI, hereafter), which was characterized by a Volcanic Explosivity Index (VEI) equal to 7 (Marianelli et al., 2006). This volcanic event is considered the largest magnitude eruption occurred in the whole Mediterranean region in the late Pleistocene. CI eruption caused the emplacement of at least 300 km^3 (Fedele et al., 2003) of trachytic-to-phonotrachytic magma (Civetta et al., 1997) as pyroclastic fall and current deposits (Fisher et al., 1993; Rosi et al, 1999). The detailed study of deposits of this eruption suggests that they were deposited in a single eruption, along NW-SE fractures (Barberi et al, 1978). After the eruption, a consequent collapse of the volcanic system occurred, generating a caldera of about 12 km in diameter (Barberi et al., 1991). Later, the collapsed part of the caldera had been invaded by the sea and filled by products of submarine volcanic activity.

A second significant eruptive phase consisted of the Neapolitan Yellow Tuff eruption (NYT, hereafter) (VEI = 6), which occurred about 15,000 years ago (Mastrolorenzo and Pappalardo, 2006). This eruption emplaced about 40/50 km^3 (Orsi et al., 1996) of pyroclastic material which covered entirely the caldera and the province of Naples. The eruption caused the collapse of an area of about 90 km^2 nested within CI caldera.

After NYT eruption, volcanic activity continued with at least 70 eruptions grouped in three different epochs of activity (15,000-9,500; 8,600-8,200 and 4,800-3,800 years ago). Eruptions occurred at monogenic tuff cones and tuff rings principally located along the structural boundary of the NYT caldera (Di Vito et al., 1999; Di Renzo et al., 2011).

Besides the eruptive activities, since 10,000 years ago a resurgence process affected the NYT caldera. This process consisted in the disjointing of the caldera floor in many blocks. One of the most evident geomorphological feature of this tectonic event consisted in the emersion of La Starza block (De Natale et al., 1987; Wohletz et al., 1999). All successive eruptions occurred near this local discontinuity. Furthermore, a significant uplift phase preceded the last eruptive event in the Campi Flegrei caldera, which generated a 130-m-high spatter cone (Monte Nuovo, 1538). In that case, there

was a vertical displacement of 7 m before the eruption (Dvorak and Gasparini, 1991). After 1538, NYT caldera has been continuously sinking, at an average rate of 1.3 cm per year (Berrino et al., 1984; Zollo et al., 2008).

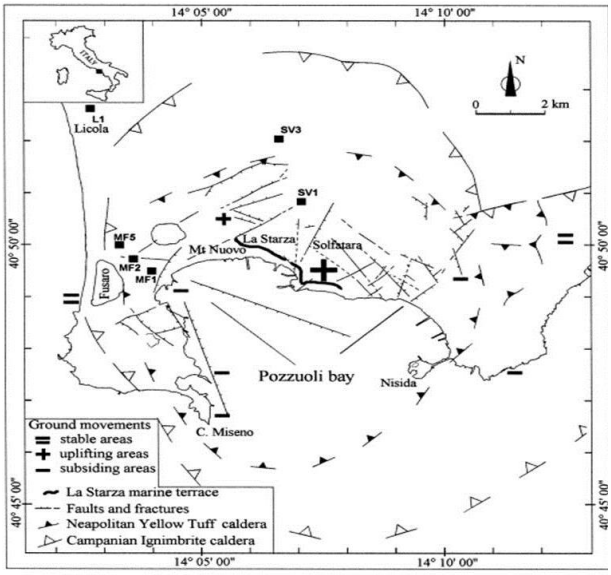

Figure 5.1 *Schematic structural map of the Campi Flegrei caldera. The borders of the CI and of NYT calderas are shown (after Orsi et al., 1999).*

Campi Flegrei in the present: the bradyseismic activity.

The current activity of the volcanic field principally consists in widespread fumarole inside and at the border of caldera, thermal spring activities as well as ground deformation episodes. In this regard, the subsidence trend of the last five centuries has been sometimes interrupted by unrest episodes characterized by short-term ground uplift. Actually, two large bradyseismic crises occurred in the last 40 years: the former between 1970 and 1972, the latter between 1982 and 1984. First uplift phase was accompanied by low magnitude seismicity. The second phase was characterized by a seismic swarm of more than 15,000 shallow microearthquakes in the magnitude range 1 - 4.2 (del Pezzo et al., 1987, de Lorenzo et al., 2001, Zollo et al., 2008). The above described bradyseismic episodes brought to a cumulative uplift of about 3.5 m in a 10-15 km wide circular area. As a consequence of these episodes, the risk of an imminent eruption was perceived. Therefore, about 30,000 people were evacuated from Pozzuoli, that is a city located at the center of the area affected by bradyseism (Bodnar et al., 2007). Since the end of bradyseismic crisis of 1982-1984, the ground has restarted the subsidence. However, several minor uplift episodes of few centimeters have been

observed in 1988-1989, 1993-1994, 2000-2001 (Gaeta et al., 2003, Battaglia et al., 2008). In July-August 2000 ground deformation reached a maximum value of about 4 cm (Saccorotti et al., 2007). Furthermore, Troise et al. (2007) relate a new uplift between the November, 2004 and October, 2006.

It is clear that now the activity that has to be mostly monitored is the above described bradyseism, and most of all the uplift episodes. Furthermore, unlike the general subsidence, uplift events are very often accompanied by seismicity.

The scientific understanding of bradyseismic phenomenon

The cause of the bradyseism is still debated in the scientific community. Generally, ground deformation in volcanic calderas are interpreted in terms of volume changes of a source of deformation at depth. It may be due either to a magma chamber (Shelly et al., 2013) or to a hydrothermal system. The joint contribution of both mechanisms can account for such volcanic activities, too (De Natale et al., 1991; Beaducel and De Natale, 2004; Amoruso et al., 2014). Concerning ground deformation phenomena at Campi Flegrei caldera, all mechanical models require that any source of ground deformations should be placed at shallow depth, approximately between 1.5 and 5.5 km depth. Starting from this consideration, several models have been conceived.

The first proposed model for Campi Flegrei uplift episodes is based on a pressure increase due to a shallow magmatic body and a resurgent dome in an elastic medium (Berrino et al., 1984; Dvorak and Berrino, 1991). Unfortunately, this model has been progressively rejected because of further geophysical analyses. In particular, these studies (e.g. Del Pezzo et al., 1996; Zollo et al., 2008) have stated that no magmatic bodies are present up to 7-8 km depth. De Natale et al. (1991) proposed a different mechanism to account for ground deformations at Campi Flegrei caldera: it is based on the action of shallow overpressured acquifers as a consequence of an energy input from the underlying magma chamber. Two possible mechanisms may explain the increase in the energy of the system: 1) a growth of the regional extensional stress; 2) a change in the chemical composition of the magmatic system. The former may cause both the opening of fractures and, as a consequence, the transfer of heat from the magma chamber to the shallower aquifers. The idea that hydrothermal fluids may have an important role in triggering activity at Campi Flegrei is valid. Actually, in the past,

correlation between ground movements and gas emissions has been found. Vanorio et al., (2005), to this end, interpreted a low Vp/Vs anomaly at 4 km depth in the center of the caldera as a zone of overpressured gas in supercritical conditions. They suggested that overpressured gasses may be the responsible of seismicity which very often accompanies unrest episodes. Beaducel and De Natale (2004) found that the observations during uplift phenomena are very well reproduced by a model in which there is a deep overpressured magma chamber. In their model they ascribed a great importance to the presence of structural discontinuities (faults and fractures) along the boundaries of the caldera.

Battaglia et al. (2006) state that the responsible mechanism of the unrest phenomena is directly linked to the presence of a shallow acquifer. In particular, the hydrothermal reservoir is fed, before unrest episodes, by lens of crystallizing magma. From this magma body there is a migration of hypersaline brine and gas. After the uplift, because of fractures in surrounding rocks, the fluids can laterally migrate. In that way, due to the deflation of the hydrothermal system, a subsidence phase starts. Todesco et al. (2014) proposed a similar mechanism; this model accounts also for the subsidence of the caldera floor.

Previous tomographic studies in Campi Flegrei caldera

In order to better understand the deep system and the main mechanisms of the Campi Flegrei activity, in the recent past a lot of tomographic studies have been carried out. Both elastic and anelastic properties of the on-land and off-shore Campi Flegrei caldera have been imaged. Both active and passive seismic data have been used.

Aster and Mayer (1988) provided a Vp, Vs and Vp/Vs image of the on-land part of the Campi Flegrei caldera. In particular, they used data recorded during the seismic swarm which occurred during the 1982-1984 bradyseismic crisis. The main result consisted of a shallow region of high Vp/Vs ratio and low Vs in the central part of the caldera, beneath the city of Pozzuoli. The authors interpreted this feature as a region of liquid-saturated cracks (figure 5.2).

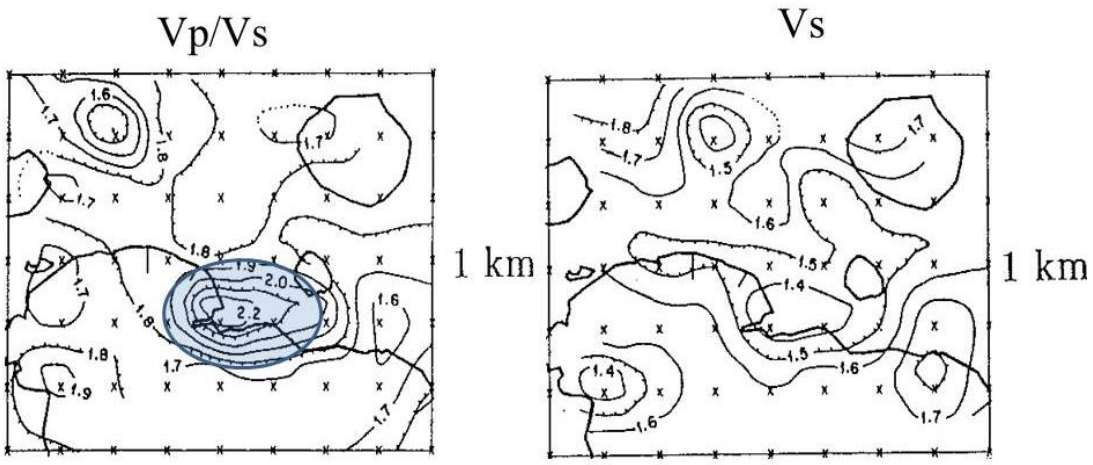

Figure 5.2 *Tomographic results of Campi Flegrei caldera modified after Aster and Mayer (1988) and Orsi et al. (1999).* ***Left:*** *Vp/Vs imaging of the on-land part of Campi Flegrei caldera. A high Vp/Vs is located beneath the city of Pozzuoli.* ***Right:*** *Vs imaging of the on-land part of Campi Flegrei caldera. Beneath the city of Pozzuoli, a Vs value has been retrieved.*

A high Vp/Vs ratio at shallow depth has been also found by Vanorio et al. (2005), Chiarabba and Moretti (2006), Battaglia et al. (2008). A similar interpretation to the one given by Aster and Mayer (1988) has been provided. Dello Jacono et al. (2009) interpreted the shallow high Vp/Vs ratio region as a water saturated volcanic and marine sediments layer. Furthermore, Vanorio et al. (2005), as well as Chiarabba and Moretti (2006) and Battaglia et al. (2008), imaged an anomalous deep low Vp/Vs region. Vanorio et al. (2005), through a rock physics modelling, interpreted it as a zone of overpressured gases under supercritical conditions.

The main feature imaged by several velocity tomography studies is an off-shore annular high Vp anomaly between 750 m and 2 km (Zollo et al., 2003; Judenherc and Zollo, 2004; Chiarabba and Moretti, 2006; Satriano et al., 2006; Battaglia et al., 2008; Dello Jacono et al., 2009) (figure 5.a). Due to the lacking of ray coverage in the off-shore region of the caldera, Vanorio et al. (2005) were not able to image that annular anomaly. On the other hand, they imaged an horse-shoe high Vp*Vs anomaly on the on-land part of the caldera (figure 5.3c). A good match has been found between these annular anomalies and positive density anomaly recognized by Capuano and Achauer (2003) and confirmed by a recent work of Capuano et al. (2013). For this reason, this geophysical evidence has been interpreted as the buried rim of the Campi Flegrei caldera. From borehole data, it is thought that the caldera rim is composed of consolidated lava and tuffs, with interbedded lava sequences (Agip, 1987).

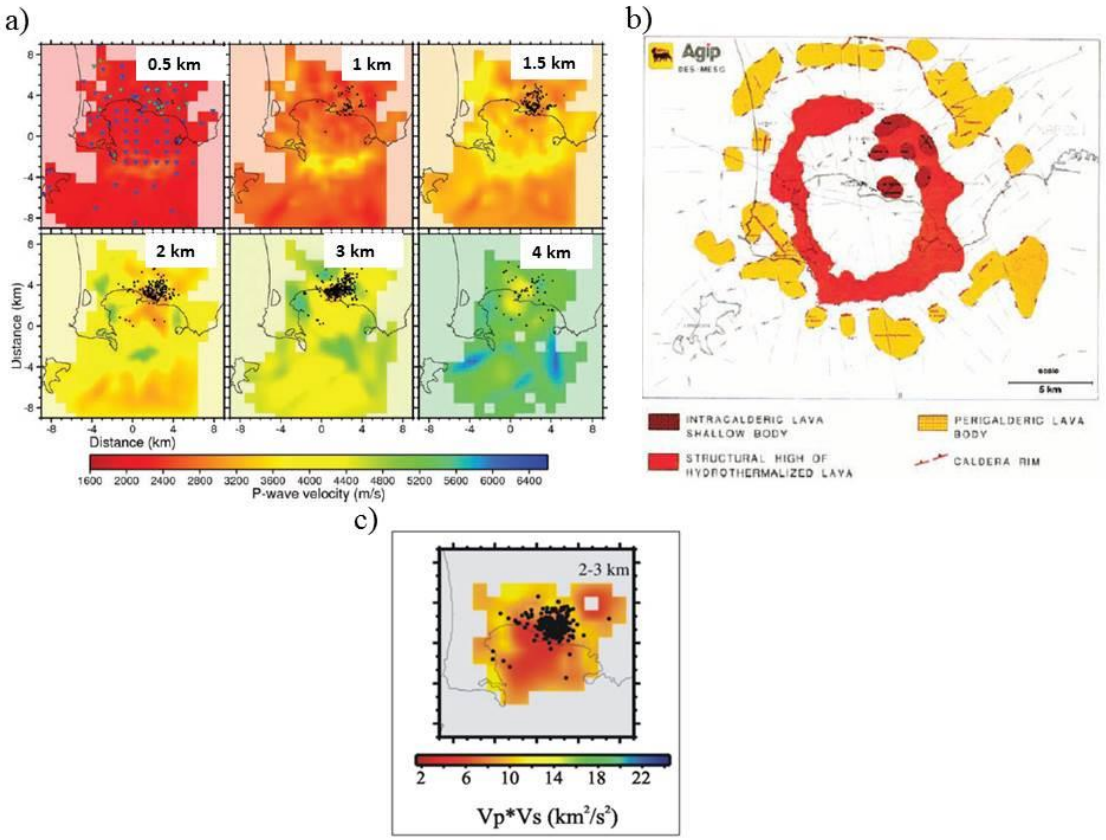

Figure 5.3 a) *P-wave tomography results (modified after Battaglia et al., 2008). The annular anomaly is evident at 1 km and 1.5 km.* ***b)*** *3D structure imaging of gravity observations (after Battaglia et al., 2008 and Agip, 1987).* ***c)*** *Vp*Vs imaging retrieved by Vanorio et al., (2005). An horse-shoe anomaly is present in the northern part of the tomographic image.*

Two attenuation tomography studies have been carried out in the past, too. They were focused on the reconstruction of the on-land part of Campi Flegrei caldera (De Lorenzo et al., 2001; De Siena et al., 2010).

De Lorenzo et al. (2001) provided a compressional wave attenution map of Campi Flegrei from earthquake data. They found a large low Qp anomaly in the north-eastern part of the caldera. In particular, this region is located between 0 and 2 km. Furthermore, between 2 and 3 km a low Q_P region has been imaged in the central-eastern part of the caldera. A high Q_P area, separating two large low Q_P regions, has been found between 0 and 2 km. The authors correlated the retrieved images with those obtained by Aster and Mayer (1988). They found a good match between the high Vp/Vs ratio areas and low Q_P anomalies. Furthermore, they interpreted the correlation between decrease of Vp/Vs ratio with depth and low Q_P values as thermal effects (figure 5.4, first row).

De Siena et al. (2010) provided Q_P and Q_S maps using a similar dataset to the one used by De Lorenzo et al., (2001)(figure 5.4 second row and third row). De Siena et al. (2010) have imaged three hydrothermal basins, characterized by high Q_P^{-1} and Q_S^{-1} values and well correlated with high Vp/Vs regions. These hydrothermal basis are located principally in the region between Monte Nuovo and Mofete, and beneath Pozzuoli and Agnano. Furthermore, the authors interpreted low Q_P^{-1} and Q_S^{-1} values at 3 km depth as the top of an hard-rock layer, in correspondence with discontinuity already seen by Zollo et al. (2008) at about 2.7 km.

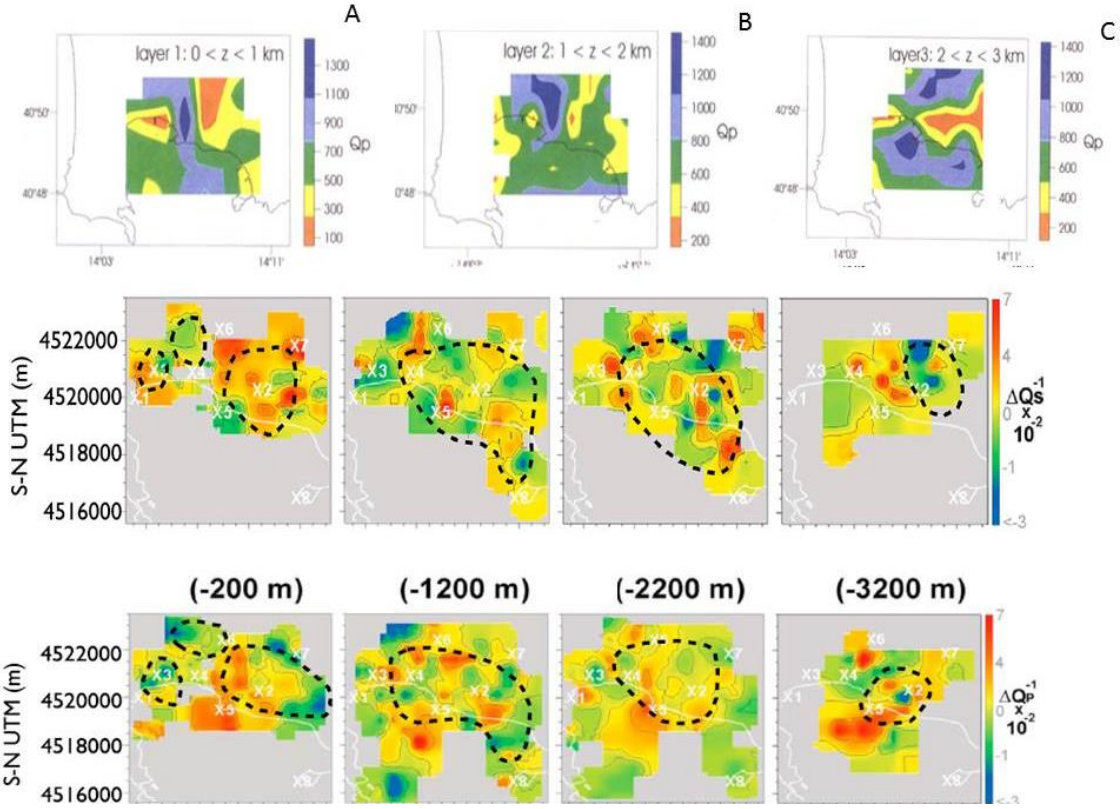

Figure 5.4 First row: *de Lorenzo et al. (2001) Q_P images.* ***Second Row:*** *De Siena et al. (2010) Qs images at different depths (-200 m, -1200 m, -2200 m, -3200 m). These are expressed in terms of variations of the attenuation parameter from a mean value equal to about 100 previously computed.* ***Third row:*** *De Siena et al. (2010) Q_P images. These are expressed in terms of variations of the attenuation parameter from a mean value equal to about 200 previously computed.*

5.2 The inversion strategy

The three dimensional Q_P model of Campi Flegrei caldera has been obtained by the inversion of the dt^* data measured from SERAPIS database and deeply described in the third chapter. The tomographic grid has dimensions 13 x 13 x 3 km^3. The rays connecting the shots and the receivers have been traced in the average 1D Battaglia et

al. (2008). This model has been chosen because the dt^* dataset has been obtained by applying the deconvolution procedure described in the chapter 2. In particular, we remind that recorded spectra have been divided by synthetic spectra computed in a completely elastic medium. Its properties are described by the average 1D Battaglia et al. (2008) velocity model and by a density profile inferred from Zamora et al. (1994), Berrino et al. (1998), Berrino et al. (2008).

Before running the tomographic inversion, three important issues have been faced: 1) the choice of the starting model; 2) the choice of the parameterization, that is the spacing between two adjacent grid nodes along the three directions *x*,*y*,*z*; 3) the choice of regularization parameters, that is the damping factor and smoothing parameters. In particular, three different smoothing parameters, Lx, Ly, Lz (one for each direction, *x*, *y*, *z*) have to be established.

In the following paragraphs, the way through which the above questions have been dealt with will be discussed.

5.2.1 The starting model

The choice of the starting model has a great importance in any linearized tomographic problem. In case of lack of preliminary attenuation models deriving from previous tomographic studies, a starting homogeneous attenuation model is generally chosen (e.g. Hansen et al., 2004; Chiarabba et al., 2009; Bisrat et al., 2013).

In our case, no attenuation models of the off-shore part of Campi Flegrei caldera have been provided in the past. Actually, de Lorenzo et al. (2001) and De Siena et al. (2010) focused their studies on the on-land region of Campi Flegrei.

Therefore, in our case, a different approach has been followed. First, a synthetic configuration of source and receivers has been used, consisting of a single source and of 1000 receivers (figure 5.5). In particular, the closest receiver to the source is located at a distance of 587 m and it has been used as the reference receiver for the computation of synthetic dt^*. The farther receiver is located at a distance of 12 km from the source. The 587 m distance corresponds to the mean gap between the reference stations and the sources in the case of the measured dataset and real sources-receivers configuration. On the other hand, the distance of 12 km corresponds approximately to the maximum distance between the shots and the receivers in the selected SERAPIS dataset. By using

this configuration, the rays for each couple source-receiver have been traced in the average 1D Battaglia et al. (2008) velocity model.

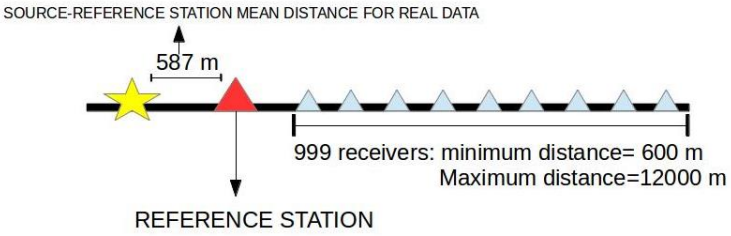

Figure 5.5 *Synthetic source-receiver configuration. The reference receiver is located 587 m distant from the unique source. 999 receivers are located on a line at distances progressively increasing from a minimum of 600 m and a maximum of 12 km.*

The trial and error procedure

After ray tracing, a trial and error procedure has been carried out. It consisted of retrieving the synthetic dt^* distribution which best fits the mean distribution of measured dt^*. It has been done by gradually adjusting simple 1D attenuation models. Then, the computed dt^* distribution is compared with the measured one (cfr. figure 3.11a). For sake of clarity, as an example, in figure 5.6 it is shown the synthetic dt^* distribution relative to a trial 1D attenuation model overlapped with the measured dt^* distribution.

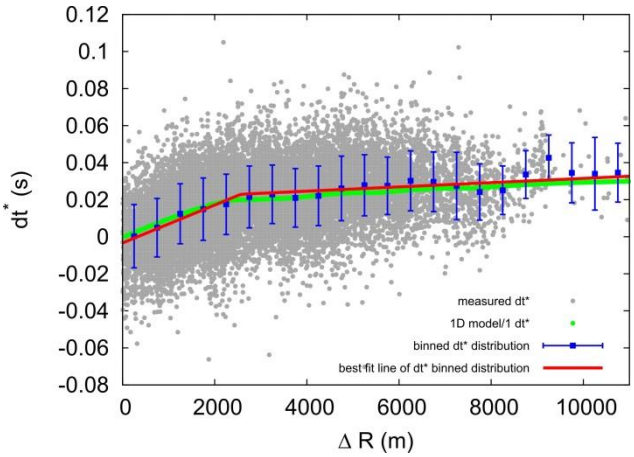

Figure 5.6 *Synthetic dt* distribution. The grey points represent the real measured dt^*. The blue points represent the binned measured dt^* distribution. The red line the best fit line of the binned distribution. The green aligned points describes the synthetic dt^* computed for a trial 1D attenuation model. The dt^* have been computed by using the source-receivers configuration represented in figure 5.5.*

The tested 1D attenuation models can be described by a set of four parameters, Q_0, Q_1, α and h. These parameters are related each other through the following relation:

$$\begin{cases} Q = Q_0 & z < h \\ Q = Q_1 + (z-h)\alpha & z \geq h \end{cases} \qquad (5.1)$$

The attenuation models are discretized with a 125 m step along the z direction and extend up to 3 km depth. As a matter of fact, based on the actual source-receiver configuration and on the average 1D Battaglia et al. (2008) velocity model, only 9 rays out of a total of more than 15000 rays reach a depth greater than 3 km. The maximum depth which has been reached by rays is 3.5 km.

The chosen attenuation model is the one which, based on a simple visual inspection, shows the best agreement between synthetic and measured dt^*. The retrieved 1D attenuation model is represented in figure 5.7 and is described by the following set of parameters:

Q_0=50,

Q_1=70,

h=750,

α=0.0375.

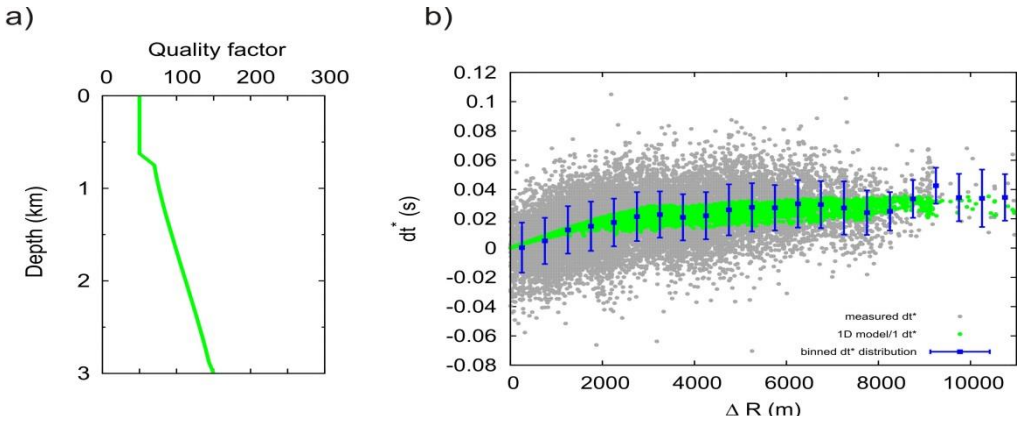

Figure 5.7 a) *Retrieved 1D attenuation model from the trial and error procedure.* ***b)*** *Synthetic dt* distribution relative to the 1D attenuation model obtained through the described procedure. The green points represent the synthetic dt* relative to the real sources-receivers configuration. Grey points represent the measured dt*. The blue points, with the associated error bar, describe the mean distribution of measured dt*.*

The grid search procedure

In order to better define a 1D attenuation model of the Campi Flegrei caldera a grid search procedure has been implemented. In that way, all physically admissible values of the four parameters (Q_0, Q_1, α and h) have been explored.

At the beginning, a grid step of 50 for the parameters Q_0 and Q_1 has been fixed. The range of explored values of these parameters is between 1 and 1000. On the other hand, the range of explored values of the parameter h extends from 250 to 1000, with a grid

step of 125. Finally, the range of explored values of the parameter α extends from 0.02 to 0.05 with a grid step of 0.0025 (figure 5.8).

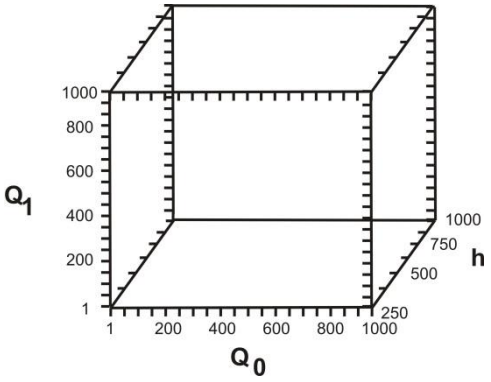

Figure 5.8 *Schematic representation of a three dimensional parameter space. In this example, it is constituted by the triad of parameters (h,Q_0,Q_1).*

In order to constrain the model parameters, a recursive procedure has been adopted. It is based on a grid search in a three dimensional parameter space constituted by the triads (h,Q_0,Q_1), (α, h, Q_1), (Q_0, α, h) and (Q_0, α, Q_1). For each search in the three dimensional parameter space, the fourth parameter is fixed either to the initial value or to the value obtained in the previous step. In our case, the initial values correspond to the parameters estimations obtained through trial and error procedure. For each combination of parameters, the misfit (RMS) between the measured and computed data has been measured. Therefore, the combination which minimizes the prediction error is chosen as final result (de Lorenzo et al., 2014).

Two different grid search explorations have been carried out. The difference between these procedures consists in the fixed parameter at the first step of the exploration:

1) at the initial step the parameter α has been fixed to a value equal to the one provided by trial and error procedure (α=0.0375). First, the triad (h,Q_0,Q_1) has been allowed to vary in the parameter space. In the following step, the parameter Q_0 has been fixed to the value obtained at the previous step, and the triad (α, h, Q_1) was allowed to vary in the space of parameters. The following steps have been carried out in a similar way; each time the fixed parameter and the triad which is allowed to vary have been changed.
2) At the initial step the parameter Q_0 has been fixed to a value equal to 50, that is the one provided by trial and error procedure. The triad (α, h, Q_1) was allowed to vary in the parameter space. In the following step, the parameter Q_1 has been

fixed to the value retrieved at the previous step. An analogous procedure has been performed for the following steps.

The results retrieved at the end of the procedure have been used as initial value for a more refined grid search exploration. This has been done for both the above described explorations. In this second phase, a grid step of 10 for the parameters Q_0 and Q_1 has been fixed. The range of explored values of these parameters is between 30 and 200. The explored values of the parameter h goes from 250 to 750, with a grid step of 125. Finally, the range of explored values of the parameter α extends from 0.03 to 0.04 with a grid step of 0.00125.

Both the refined explorations provided the same results, that are:

Q_0=70,

Q_1=50,

h=350,

α=0.0375.

It means that the choice of the parameter which is fixed at the first step of the grid procedure is not crucial in obtaining the final results. Figure 5.9 shows the retrieved 1D attenuation model and the computed dt* distributions. In particular, these are relative to the synthetic source-receivers configuration (figure 5.9b) and to the real sources-receivers configuration (figure 5.9c).

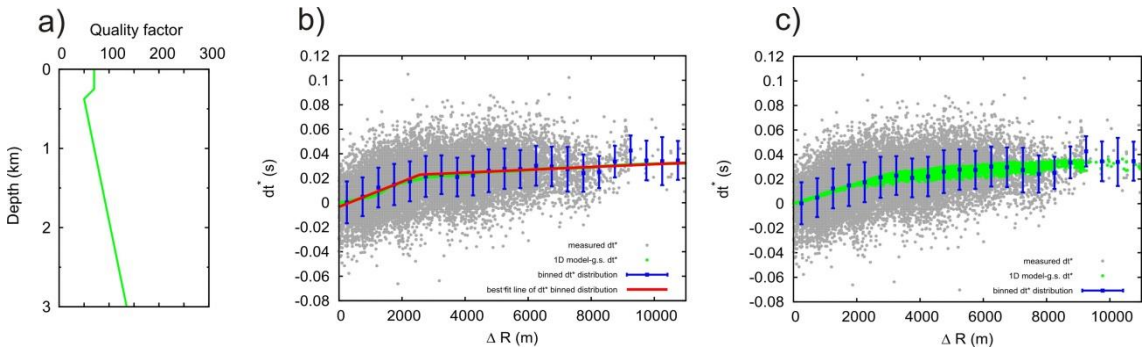

Figure 5.9 a) *Retrieved 1D attenuation model from grid search procedure.* ***b)*** *Synthetic dt* distribution relative to the 1D attenuation model obtained through the described procedure. The green aligned points represent the synthetic dt* relative to the source-receivers configuration described in figure 5.5. Grey points represent the measured dt*. The blue points, with the associated error bar, describe the mean distribution of measured dt*. The red line identifies the best fit line of the mean distribution of measured dt** ***c)*** *The same convention of colours of* ***b)*** *has been used. In this case, green points represent the theoretical dt* distribution computed with the real sources-receivers configuration.*

The random exploration of 1D attenuation models

The two described techniques (trial and error procedure and grid search exploration) have provided two different results, even if they are very similar. In particular, both models show a linear increase of the parameter Q_P for depths greater than 750 m. Furthermore, the Q_P value in the shallower part of the model is very similar in the two different 1D attenuation models.

Due to the existing discrepancies between the two models, a different approach has been followed. The average 1D attenuation model (hereafter "reference model") between the two models retrieved by the above described techniques has been computed. Then, 200 1D compressional attenuation models have been randomly generated within two extreme 1D attenuation models (Vanorio et al., 2005). The upper and lower bound of the interval of random models have been chosen so that their average model coincides with the "reference model".

Each of 200 1D random attenuation models has been used as initial model for the tomographic inversion of measured dt^*. Figure 5.10 represents the "reference model", the upper and the lower bound, and the 200 1D initial random models.

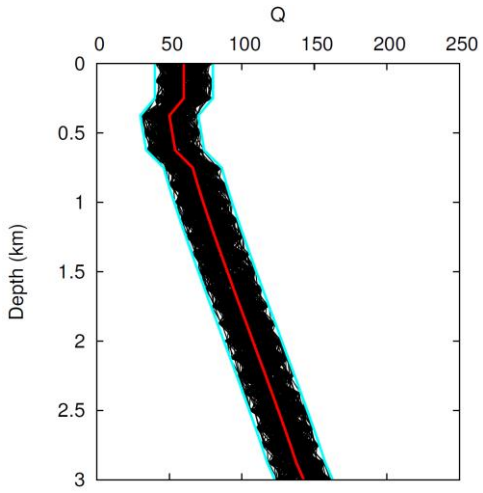

Figure 5.10. *The red line represents the "reference model", obtained as the average between the 1D attenuation models retrieved through a trial and error procedure and a grid search exploration, respectively. The cyan lines describe the upper and lower bound used for the generation of 1D random attenuation models. The latter, finally, are represented by black solid lines.*

5.2.2 The grid spacing and regularization parameters

The selection of proper regularization parameters is directly linked to the used parameterization in the tomographic grid. For example, depending on the distance between two adjacent nodes, the requested degree of smoothing of the retrieved anomalies may be different. Furthermore, the degree of underdetermination of the

tomographic problem strongly depends on the ray sampling of inversion nodes and, hence, on model parameterization (Kissling et al., 2001). It follows that the regularization parameters will depend on the grid spacing.

The choice of the grid spacing in the tomographic model is very important, since it controls the smallest spatial anomaly which can be recovered. On the other hand, its choice is crucial because a too small parameterization can introduce false anomalies and artifacts inside the retrieved tomographic images.

In the following sections the used criteria for the selection of model parameterization and of regularization parameters will be described. First, by establishing a trial parameterization, the procedure to estimate the optimum regularization parameters will be described. After that, we will present the considerations and the statistical analysis which have been carried out in order to select the proper grid spacing.

The choice of the damping and of smoothing parameters

The criterion that is generally used to select the damping factor in a tomographic problem has been already introduced (cfr. paragraph 4.1). It is has been said that this criterion is also used to estimate the optimum smoothing parameters. In our case, in order to pick the best combination between damping and smoothing parameters, the recursive scheme proposed by Rawlinson et al. (2006) has been used.

First, a trial parameterization that is: dx = 0.5 km, dy = 0.5 km, dz = 0.25 km has been used. After that, an initial 1D attenuation model has been chosen: it is the one obtained by means of trial and error procedure before described (figure 5.7a). Then, a trial combination of smoothing parameters Lx=Ly=Lz=1 has been fixed. In this case, the degree of smoothing is equal along the three directions.

After that, "several one-step inversions have been run with different damping values". In particular, damping parameter equal to 0.1, 0.35, 0.6, 0.85, 1.10, 1.5, 2, 3 and 6 were tested. Figure 5.11a shows the resultant trade-off curve between the residual data variance and model variance. The damping parameter, ε^2, showing the best compromise between these two quantities is located between the points corresponding to 0.35 and 0.6. For this reason, an intermediate value ε^2=0.5 has been chosen.

In the next-step, by fixing ε^2=0.5, many one-step inversions have been run with different combination of Lx, Ly, Lz. All possible combinations between smoothing

parameters have been studied. In particular the combination of value 0.1, 0.2, 0.3, 0.4, 0.7, 0.9 has been explored. The figure 5.11b shows the most meaningful trade-off curves between the residuals data variance and model roughness (equation 4.28). Each curve is relative to a particular combination of smoothing parameters. In most cases, two of them are fixed, whereas the third one varies along the curve. The red curve, instead, describes the trade-off between residuals data variance and model roughness by varying simultaneously the three parameters. The optimum curve is chosen to be the closest one to the origin of the graph. The optimum value, instead, is chosen to be the closest one to the elbow of the curve. In this case, the combination Lx=Ly=Lz=0.3 has been selected.

By fixing Lx=Ly=Lz to the estimated values 0.3, a new search of the optimum damping parameter has been performed. The trade-off curve generated from this process suggests that ε^2=0.65 produces a model which satisfies both the residuals and the model variance (figure 5.11c).

In the next step, a further exploration of smoothing parameters has been carried out. The resulting trade-off curves shows that the combination Lx=Ly=Lz=0.3 is still a good choice of smoothing parameters (figure 5.11d). Therefore, further iterations of the illustrated process are unnecessary.

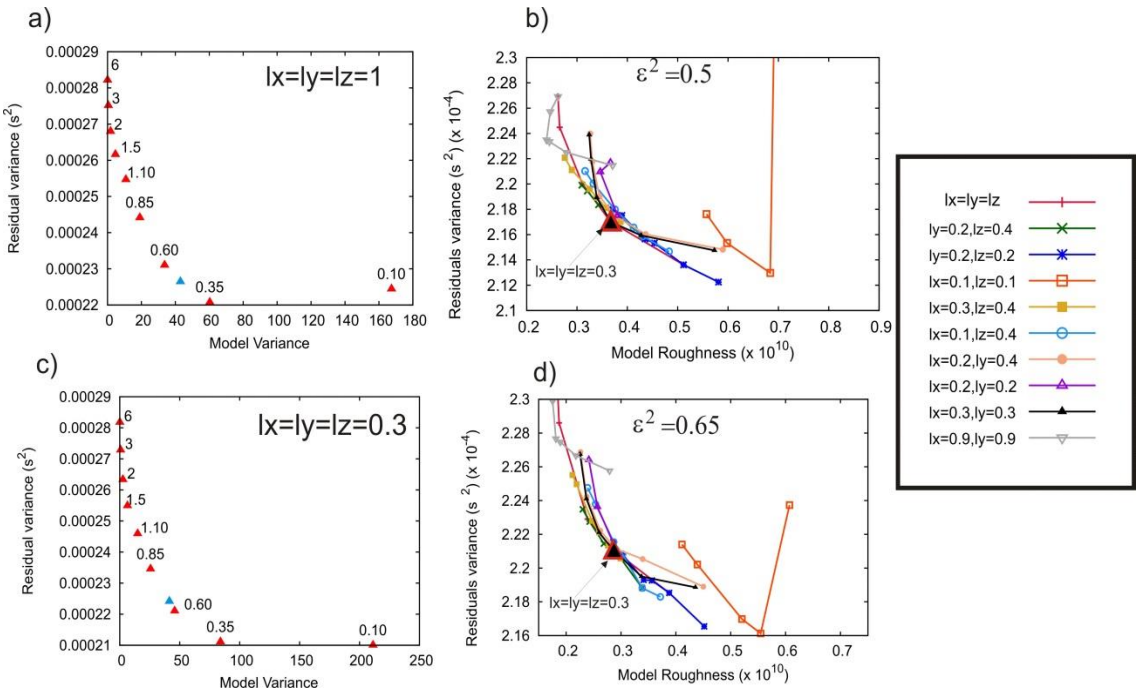

Figure 5.11(previous page) *The recursive iterative procedure adopted for the choice of the proper regularization parameters is here described.* ***a)*** *Trade-off curve between the variance of residuals and variance of the model. Several one-step inversions have been carried out by fixing Lx=Ly=Lz=1 and by varying the damping parameter. The chosen damping parameter is* $\varepsilon^2=0.5$*, and it is represented by the cyan triangle.* ***b)*** *Trade-off curve between residuals variance and model roughness. They have been obtained by fixing the damping parameter to the one retrieved at the previous step and by progressively changing the combination between smoothing parameters. Each curve represents a different combination between Lx, Ly and Lz. In particular, two parameters are fixed, and the third one changes along the different points of the curve. The correspondence between the different combination of smoothing parameters and the colours of the curve is shown in the box at the right of the figure. At this step of the procedure, the combination Lx=Ly=Lz=0.3 has been chosen. It is indicated with the largest black triangle, that is surrounded by a red line.* ***c)*** *Analogously to the procedure adopted at the first step, a trade-off curve between residuals variance and model variance has been retrieved. The smoothing parameters have been fixed to the values retrieved at the previous step. The chosen damping parameter is* $\varepsilon^2=0.65$*, and it is represented by the cyan triangle.* ***d)*** *Analogously to the procedure adopter at the second step, several trade-off curves between residuals variance and model roughness have been retrieved. The damping parameter has been fixed to the value obtained at the previous step. The combination of smoothing parameters that is chosen at this step is Lx=Ly=Lz=0.3. It is represented by the largest black triangle, that is surrounded by a red line. Since it is equal to the one retrieved at the second step of the iterative procedure, no further iterations have been necessary. Therefore, the final combination of regularization parameters is* $\varepsilon^2=0.65$ *and Lx=Ly=Lz=0.3.*

The choice of the model parameterization

In order to properly select the grid spacing for the tomographic inversion of measured dt^*, two preliminary considerations have been done:

1) Battaglia et al. (2008) have provided an elastic tomographic model of the off-shore part of the Campi Flegrei caldera by using a merged passive and active seismic dataset. It means that they used a source-receivers configuration similar to the one used by us. In their work, they used a uniform grid spacing at the size of 0.5 x 0.5 x 0.5 km^3;
2) it is known that the spatial resolution of seismic imaging depends also on the wavelengths of the signals which have been analysed. In particular, it is generally requested that the wavelength is smaller than the cell size. In the present dataset, spectra have been analysed in the frequency range 5-25 Hz. Moreover, if we consider the average 1D Battaglia et al. (2008) velocity model, the mean value of P waves velocity in the upper 3 km of the Campi Flegrei caldera is equal to 2.75 km/s. Since the wavelength λ is directly linked to the frequency f and to the velocity c by means of the relation $\lambda=c/f$, the mean wavelength of analysed signals is about 200 m.

After these initial observations, a more thorough analysis has been performed. In particular, by using as initial model the 1D attenuation model retrieved from the trial and error procedure, several inversions have been run with different parameterization: 1 x 1 x 0.5 km^3; 1 x 1 x 0.25 km^3; 0.5 x 0.5 x 0.25 km^3; 0.25 x 0.25 x 0.25 km^3. For each model parameterization, a preliminary study concerning the choice of proper regularization parameters has been carried out. To this purpose, the same recursive iterative procedure described in the previous section has been adopted. To establish the attenuation model which best reproduces the data, and therefore which is the optimum grid spacing to be used, the final RMS is not a sufficient criterion. In fact, the increase in the model parameters always coincides with a decrease in the final RMS. However, the reduced RMS can also be reflected in an unnecessary increase in the complexity of the final result. Therefore, a statistical comparison (Akaike, 1974) between models characterized by a different number of parameters has been carried out. In particular, this statistical criterion allows to select, among many models, the one producing the minimum value of the AIC (Akaike Information Criterion). It means that the chosen result provides the best compromise between the adherence to data and model simplicity. In our case, a corrected Akaike Information Criterion (AIC_c) has been used (Cavanaugh, 1997):

$$AIC_C = n(\ln 2\pi E + 1) + \frac{2(p+1)n}{n-p-2}. \qquad (5.2)$$

In the previous expression, the term n represents the number of data; the number of parameters is represented by p, whereas the term E is the final misfit.

Therefore, models obtained at the tenth iteration of the inversion have been compared through the computation of AIC_c. The minimum AIC_c value has been obtained with the 0.5 x 0.5 x 0.25 km^3 grid spacing (Table 5.1).

GRID SPACING (km^3)	RMS(s)	AIC_c
1 x 1 x 0.5	0.0153	-74578.7891
1 x 1 x 0.25	0.0150	-68774.1094
0.5 x 0.5 x 0.25	0.0138	-596470.875
0.25 x 0.25 x 0.25	0.0129	-122557.727

Table 5.1 *Estimations of AIC_C for different parameterizations.*

Based on the initial considerations and on the results of a statistical analysis, the chosen parameterization is 0.5 x 0.5 x 0.25 km^3. Furthermore, it is very similar to the one used by Battaglia et al. (2008). This choice has allowed to investigate in a very detailed way both the horizontal and the vertical heterogeneity of the shallower part of the off-shore Campi Flegrei caldera.

5.3 The three dimensional attenuation model

The tomographic inversion of selected dt^* dataset has been run in a tomographic grid of dimensions 0.5 x 0.5 x 0.25 km^3. The chosen damping factor is ε^2=0.65, whereas the selected smoothing parameters are Lx=Ly=Lz=0.3. Two hundred tomographic inversions have been run using as starting attenuation model the randomly generated 1D models. Figure 5.13 shows the initial RMS for each starting Q_P model and the final RMS at the ninth iteration. Only the attenuation models having a final RMS less than 0.0140 s have been selected. After that, the average attenuation model between 108 picked Q_P models has been computed. In this way, we think that the influence of the starting attenuating model is somehow damped and averaged. The average attenuation model represents the final result of the tomographic inversion. The retrieved image produce a reduction of 28 % of the variance of residuals with respect to the "reference model" (figure 5.15).

Figure 5.14 shows the map view of the tomographic result. In particular, each panel represents the attenuation model at different depth slices: 0.25 km, 0.5 km, 0.75 km, 1 km, 1.25 km, 1.5 km. The regions without ray coverage are represented in grey. The distribution of adopted shots and stations is shown separately in the figure 5.12.

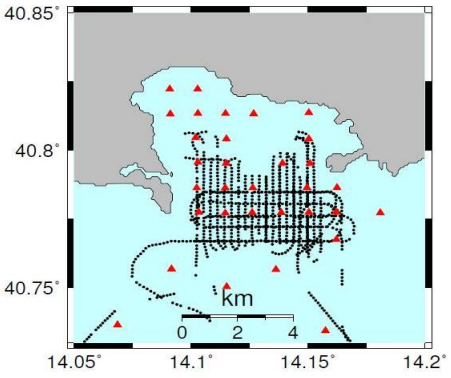

Figure 5.12 *Position of sources (black points) and receivers (red triangles) used for the tomographic inversion.*

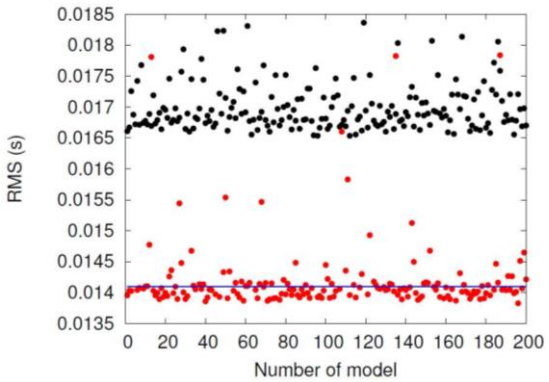

Figure 5.13 *Initial and (black points) and final misfit values (red points) relative to 200 random 1D attenuation models. The blue line represents the threshold under which the 3D attenuation models have been selected.*

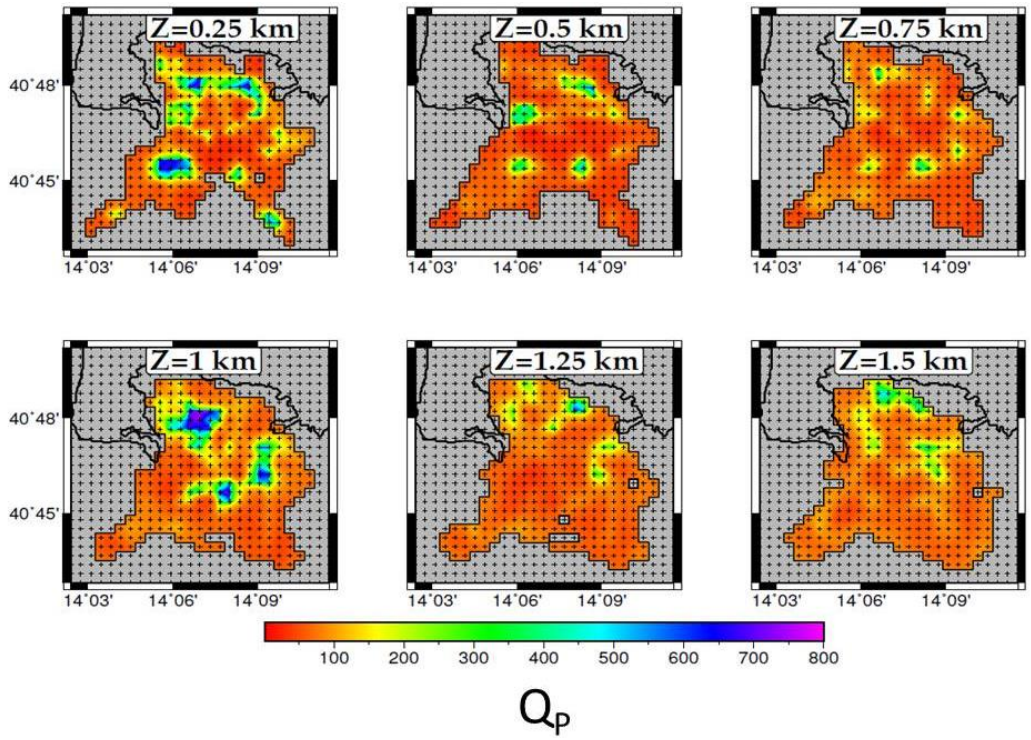

Figure 5.14 *Map view showing the final solution for P wave attenuation structure. The black crosses represent the nodes of the tomographic grid. The grey regions identify the areas not crossed by the rays. The main features of the tomographic images are reported in the text.*

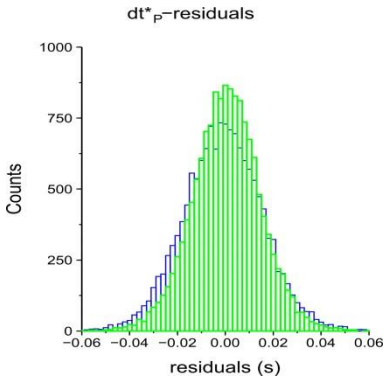

Figure 5.15 *Histogram of the residuals between measured and computed dt^*. The grey histogram represents the final distribution of residuals, whereas the blue histogram represents the distribution of residuals for the "reference model".*

The Q_P retrieved model describes a medium characterized by high attenuation layers. In particular, the central part of the Campi Flegrei caldera shows low Q_P values, less than 50 up to 0.5 km. As the depth increases, the Q_P values in the same area lightly increase, too. As a matter of fact, values greater than 100 have been reached. Several high Q_P anomalous bodies have been recovered in the studied area, both at shallow and at greater depths.

In particular, at 250 m depth, three high Q_P bodies have been imaged:

1) a W-E structure is present in the central part of the Pozzuoli Bay (north part of the tomographic model). The recovered Q_P estimations have maximum value

greater than 600;

2) an approximately circular body is present in the western part of the Pozzuoli Bay, very close to Capo Miseno; maximum Q_P values are between 250 and 350.
3) an almost elliptical W-E structure is located in the south-western part of the Campi Flegrei caldera. This structure is placed in correspondence of Miseno Bank, that is one of the three submerged volcanic edifices in the offshore part of Campi Flegrei.

The map representing the tomographic results at 500 m depth shows four small bodies characterized by lower attenuation (Q_P value about 250). They are very similar in terms of Q_P values and are located: 1) in the north-eastern part of the Pozzuoli Bay; 2) in a region very close to Capo Miseno; 3) in the southern part of Campi Flegrei caldera. The southern anomalous bodies are placed approximately in correspondence of Miseno Bank and Pentapalummo Bank. The latter is another monogenetic submerged volcano in the Thyrrenian Sea.

The map relative to tomographic images at 750 m depth shows short wavelengths, high Q_P bodies describing a pseudo-circular pattern. They occur mostly along the eastern and southern sector of the annular structure which has been imaged in previous gravimetric and tomographic works. It was interpreted as the buried rim of the volcanic caldera.

At 1 km depth, an arc-like high Q_P anomaly has been imaged, mainly in the eastern and in the southern part of the caldera. Very high Q_P values have been estimated, up to 700. Moreover, a very low attenuation body has been retrieved in the central-western part of the Pozzuoli Bay.

Finally, at greater depths, that is 1.25 km and 1.5 km, isolated high Q_P anomalies have been found. However, at these depths, the ray coverage is very poor, as it will be shown in the next paragraph.

5.4 Resolution study

The quality of the tomographic model determined from the inversion setup has been assessed in several ways. In particular, DWS, Resolution Diagonal Element (RDE) and spread function have been computed. Furthermore, fixed geometry tests and a checkerboard test have been carried out. The former have been performed in order to specifically assess the reliability of high Q_P anomalous bodies recovered in the

tomographic model. Checkerboard tests, on the other hand, have been performed in order to check the minimum anomaly size that is revolved by means of tomographic inversion.

5.4.1 DWS, RDE and Spread Function

The DWS represents an average measure of the ray density in the neighborhood of every node of the model. It is equivalent to the total ray length map which is commonly used in a tomographic model represented through cells discretization. The DWS gives more information than the simple sum of the number of rays which pass close to a grid node. It takes into account also the distance between the ray and the model parameter. "The DWS of the n^{th} attenuation parameter α_n is defined as

$$DWS(\alpha_n) = N \sum_i \sum_j \left\{ \int_{P_{ij}} \omega_n(x) ds \right\}$$ " (Toomey and Foulger, 1989). (5.3)

In the above equation, the index i and j represent the source and receiver indexes, respectively. The parameter ω_n is the weight used in the linear interpolation and depends on the position of the ray with respect to the grid node; the term P_{ij} is the ray path between the source and the receiver, and finally the term N is a normalization factor which takes into account the volume influence by α_n. The absolute values of DWS are not meaningful, since they are only relative estimations of which are the nodes mainly crossed by the rays. However, poorly sampled nodes will be marked by relatively small values for DWS.

The computed DWS relative to the chosen parameterization and to the average 1D Battaglia et al. (2008) velocity model is shown in the figure 5.16. Each panel represents the DWS at each slice of the tomographic model up to 2 km depth. It is evident that the higher ray sampling is obtained at shallow depths, up to 750 m – 1 km. In particular, the best sampled region is the central part of the tomographic grid. For depths greater than 1 km – 1.25 km the ray coverage is very low.

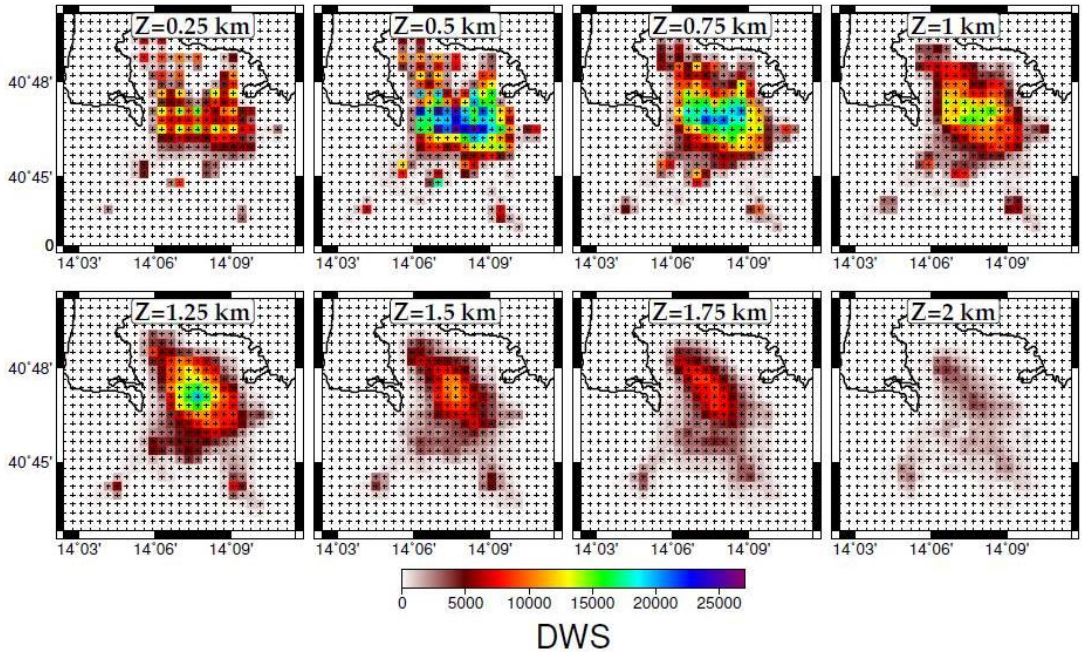

Figure 5.16 *Computed DWS at each z-slice of the tomographic model. The regions mainly covered by the rays are those at 0.5 and 0.75 km depth, in particular in the central part of Campi Flegrei caldera. The black crosses represent the nodes of the tomographic grid.*

Several studies have shown that DWS values give a good representation of the diagonal element of the resolution matrix of the model and of possible smearing (Michelini and McEvilly, 1991; Hauksson, 2000; Rietbrock, 2001). Nevertheless, the resolution matrix of the model and the spread function have been computed in our case.

The resolution matrix has been defined by Menke (1984) as:

$$R = \left(G^T G + \varepsilon^2 I\right)^{-1} G^T G \qquad (5.4)$$

and describes how closely an estimate of the model parameters is to the true solution. The resolution matrix has dimensions M x M, where the term M represents the number of parameters. If the matrix R is equal to the identity matrix, then a perfect resolution has been achieved and each parameter of the model is uniquely determined. In order to computed the resolution matrix of our tomographic problem, the damping factor ε^2=0.5 has been chosen. Actually, it corresponds to the regularization parameter used by Battaglia et al. (2008) tomographic work.

The figure 5.17 represents the map view of the diagonal elements of the resolution matrix (RDE). By comparing this image with DWS images, it is evident that the best resolution coincides with regions mainly covered by rays. In particular, at 1.25 km, only

few parameters of the model are characterized by a RDE greater than 0.6. It confirms the fact that at these depths the resolution is very low, due to a very poor ray coverage.

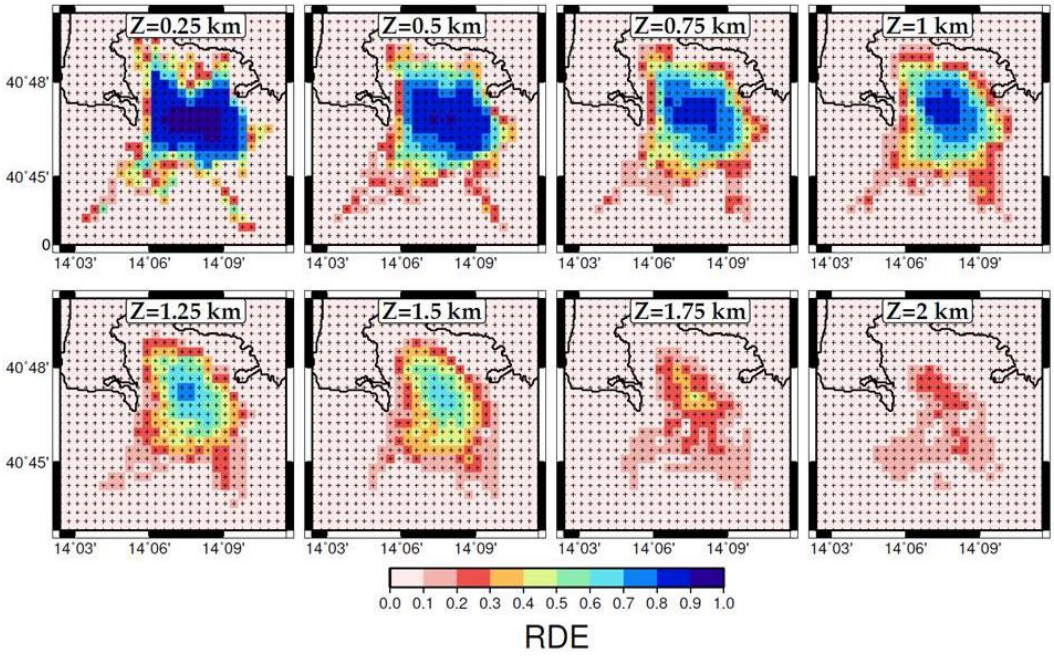

Figure 5.17 *Representation of diagonal elements of the resolution matrix. The black crosses represent the nodes of the tomographic grid. A satisfactory agreement between RDE and DWS is achieved. The above panels show that a very good resolution (RDE >0.7) is achieved up to 1 km depth, mainly in the central part of the tomographic grid. At greater depths, the resolution strongly decreases.*

A well resolved node coincides with a parameter at whose correspondence the resolution is peaked and characterized by a value close to 1. Furthermore, it means that the resolution does not contain meaningful contributions from surrounding nodes. In order to infer the possible contribution from adjacent nodes, the ***spread function*** for each parameter of the model has been computed. In particular, for each node, the spread function compresses the information contained in the whole row of the resolution matrix into only one value. The Spread function relative to the node *j* as defined by Toomey and Foulger (1989) is

$$SF_j = \log\left[\left|r_j\right|^{-1}\sum_{k=1}^{N}\left(\frac{r_{jk}}{\left|r_j\right|}\right)D_{jk}\right]. \qquad (5.5)$$

In the above expression, the term $|r_j|$ represents the norm of the *j-th* row of resolution matrix. The term r_{jk} describes the value of the element of resolution matrix of indexes *j,k*. Finally, the parameter D_{jk} defines the distance in km between two pair of nodes. The lower the SF_j value, the higher the resolution is. Actually, if a node is very well resolved, its term $|r_j|$ will have a lower value than in the opposite case. Analogously, the

summed terms, $\sum_{k=1}^{N}\left(\frac{r_{jk}}{|r_j|}\right)D_{jk}$, causes the spread function to be high for nodes that have a significant resolution contribution from adjacent and, especially, distant nodes (Reyners et al., 1999). The SF_j function describes somehow the degree of smearing in the final tomographic model.

The figure 5.18 shows the computed values of spread function for different slices of the tomographic model. Nodes characterized by high DWS and RDE values have also low values of spread function. The nodes having lowest values of SF (SF_j=-5), in particular, coincides with most resolved regions. This representation confirms that the best solved regions are at shallow depths, up to 1-1.25 km.

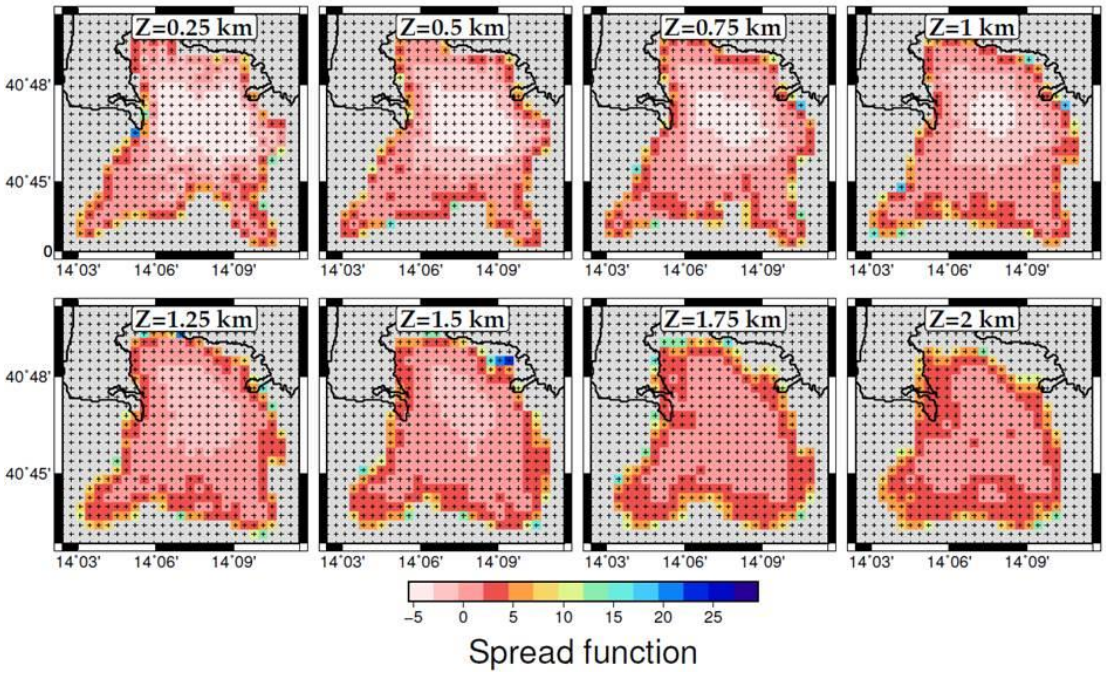

Figure 5.18 *Representation of the spread function at each slice of the tomographic model. The lowest values of SF (SF=-5) are almost completely overlapped to the nodes of the model characterized by high RDE values. Very high SF values are present in the most external nodes of the tomographic model. The grey regions represent areas not crossed by rays.*

5.4.2 Synthetic tests: fixed geometry and checkerboard tests

Four fixed geometry synthetic tests have been carried out (figure 5.19-5.22). Each test is characterized by a different attenuation structure aimed to reproduce the retrieved Q_P images at different depths. The true sources-receivers configuration of the SERAPIS dataset has been used.

Synthetic dt^* have been determined by means of a forward calculation through the velocity and attenuation model. Gaussian random noise with a variance comparable to the errors on real data has been added to synthetic data. By using the same regularization parameters (damping and smoothing parameters) adopted for the inversion of the real dataset, synthetic data have been inverted.

1) In the first fixed geometry synthetic test, the reliability of the three high Q_P anomalies recovered at 0.25 km has been assessed (figure 5.19). These anomalous bodies have been placed in a homogeneous attenuation model (Qp=30). The results of the inversion shows that the northern and southern anomalies are almost completely not detected (figure 5.19). It means that the presence of these bodies may not be a real feature of the propagation medium. These bodies can be considered false anomalies and artifacts directly linked to the low ray coverage and low RDE values in corresponding regions of the tomographic model. On the contrary, the anomaly located close to Capo Miseno, is partially recovered. However, the size of the retrieved anomaly is smaller than the real one. The recovered Q_P values are also lower than the actual one. There are no significant smearing effects both in the horizontal and in the vertical directions.
2) In the second fixed geometry synthetic test two of the four high Q_P bodies recovered at 0.5 km depth have been studied (figure 5.20). The anomalous bodies have been placed in a homogeneous attenuation medium (Q_P=30). The results of the inversion indicates that both anomalies are not well recovered, both from a geometrical and a quantitative point of view (figure 5.20). The retrieved anomalies have Q_P values equal to 90, that is lower than the synthetic Q_P value, equal to 300. Also in this case, the position of these anomalous bodies corresponds to not well resolved areas.
3) In the third fixed geometry synthetic test, the high Q_P anomalous body located in the central-western part of the Bay of Pozzuoli at 1 km depth has been reproduced(figure 5.21). In this case, the tomographic image provided by inversion of synthetic data indicates that a suitable level of recovery of the anomaly has been obtained (figure 5.21). However, the detected shape and Q_P value are partially underestimated with respect to the real ones.
4) In the last fixed geometry synthetic test, an annular anomaly has been located

between 0.75 km and 1.25 km (figure 5.22). It is characterized by a Q_P value equal to 200 immersed in an homogeneous low Q_P medium (Q_P=70). The retrieved images show an almost perfect recovery of the anomaly at 1 km depth (figure 5.22). In particular, at this depth the annular geometry is completely resolved. The retrieved Q_P estimations, instead, have values between 150 and 200. At 0.75 km depth, the annular anomaly is only partially recovered, both in terms of geometry and in Q_P values. At 1.25 km, instead, the level of recovery is lower than at shallower depths. Significant smearing effects are clearly visible in the regions of the model characterized by a very poor ray coverage, that is the southern part of the tomographic model. This feature is observable at any slice of the model. Moreover, a very light smearing effect is present at 0.5 km depth in correspondence of the annular anomaly located at greater depths.

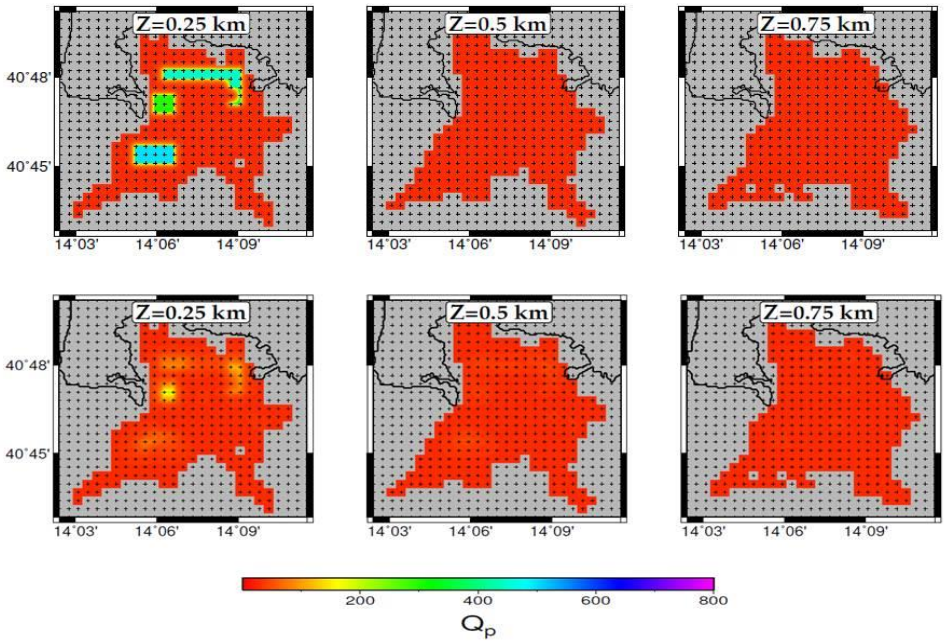

Figure 5.19 First row: *Synthetic pattern of the first fixed geometry test.* ***Second row:*** *Recovered 3D attenuation model. The northern and the southern anomaly are almost completely not detected. On the contrary, the high Q_P body close to Capo Miseno is partially recovered.*

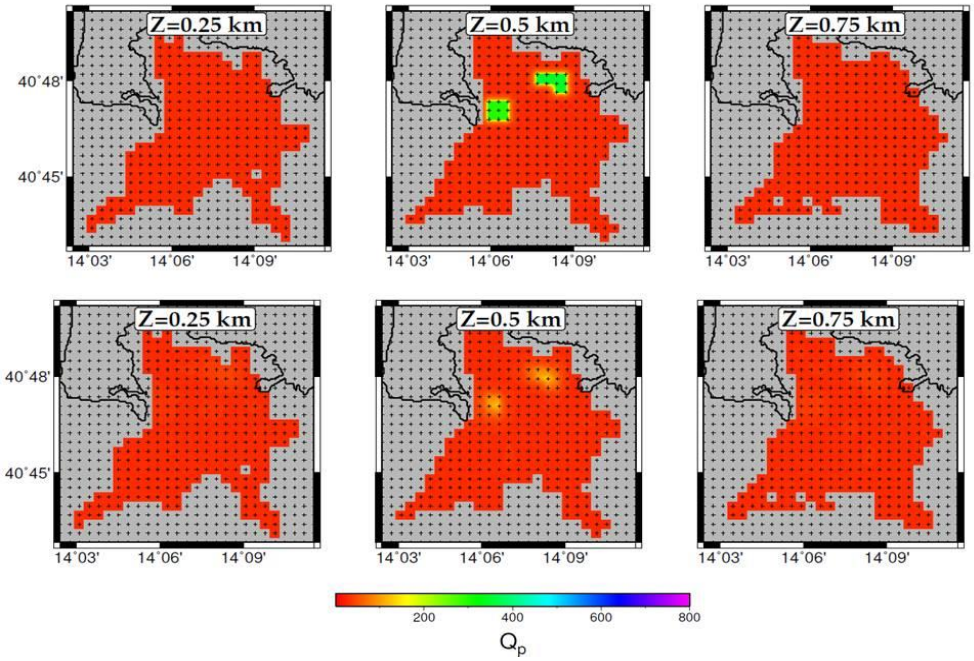

Figure 5.20 First row: *Synthetic pattern of the second fixed geometry test.* ***Second row:*** *Recovered 3D attenuation model. The two anomalies are almost completely not detected both in terms of geometry and from a quantitative point of view.*

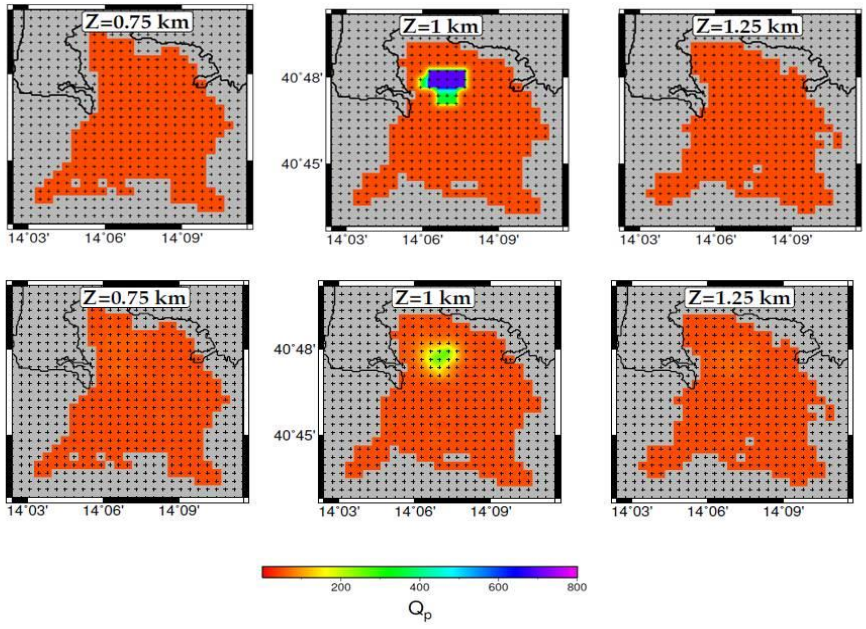

Figure 5.21First row: *Synthetic pattern of the third fixed geometry test.* ***Second row:*** *Recovered 3D attenuation model. The synthetic anomaly is recovered better than the anomalous bodies studied in the previous tests. The retrieved Q_P value is lower than the actual one, due to the low ray coverage at 1 km depth.*

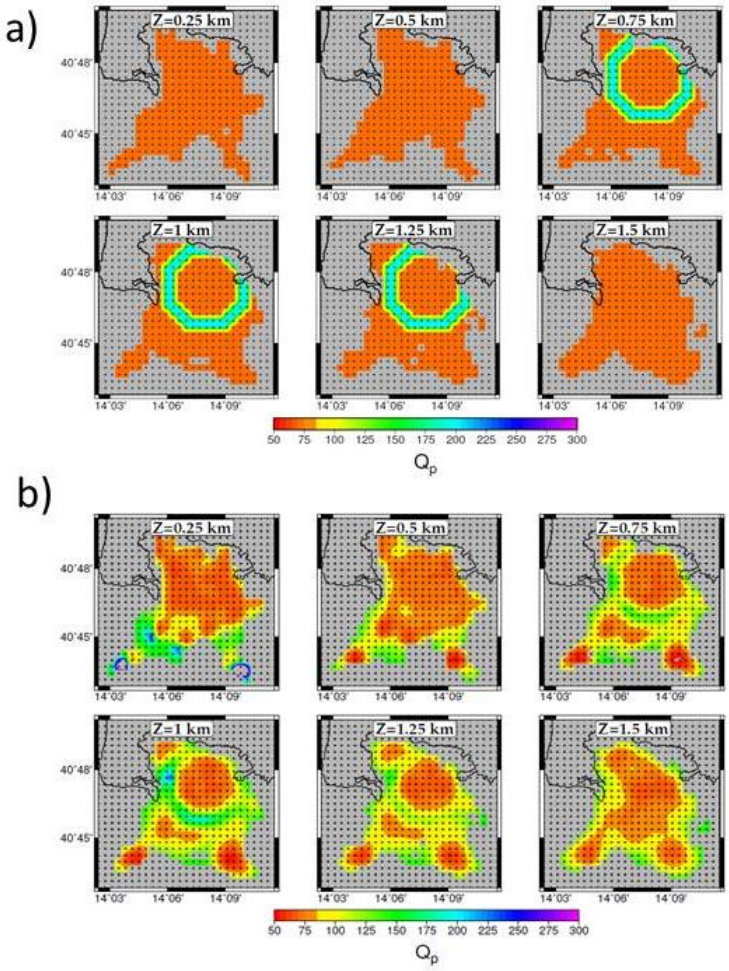

Figure 5.22 a) *Synthetic pattern of fourth fixed geometry test. An annular anomaly of Qp=200 is placed in an homogeneous low Q_P medium (Q_P=70) at depth between 0.75 km and 1.25 km.* ***b)*** *Recovered 3D attenuation model. The annular anomaly is very well resolved from a geometrical point of view at 0.75 km and 1 km depth. The Q_P estimations are lower (Qp=150) than the actual Qp value. Large smearing effect are visible in the southern part of Campi Flegrei caldera, both at shallower and at greater depths. Moreover, a light smearing effect is visible south-east to Capo Miseno.*

In addition to fixed geometry synthetic tests, a checkerboard test has been performed (figure 5.23). The checkerboard was constructed taking an homogeneous model with *Qp*=200 which is characterized by the same parameterization of the tomographic grid (0.5 x 0.5 x 0.25 km^3). A perturbation of 25% is superposed to the attenuation model. Since the use of regularization parameters does not favour the reconstruction of sharp attenuation contrast between nodes, a model node with average attenuation value has been positioned between these blocks. In this way, an anomalous checkerboard structure has been obtained. It is characterized by the alternation of nodes having the values 150-200-250. Figure 5.23 represent the synthetic pattern and the recovered one. Synthetic dt^*

have been determined by means of a forward calculation through the velocity and attenuation model. Also in this case, Gaussian random noise with a variance comparable to the errors on real data has been added to synthetic data. By using the same regularization parameters (damping and smoothing parameters) adopted for the inversion of the real dataset, synthetic data have been inverted.

The results of the inversion clearly show that in the central part of the tomographic model, up to 750 m, the checkerboard structure is well recovered. It means that attenuation anomalies of size equal to 500 m is are detected by the tomographic inversion. These results confirm what we have already observed from previous synthetic tests.

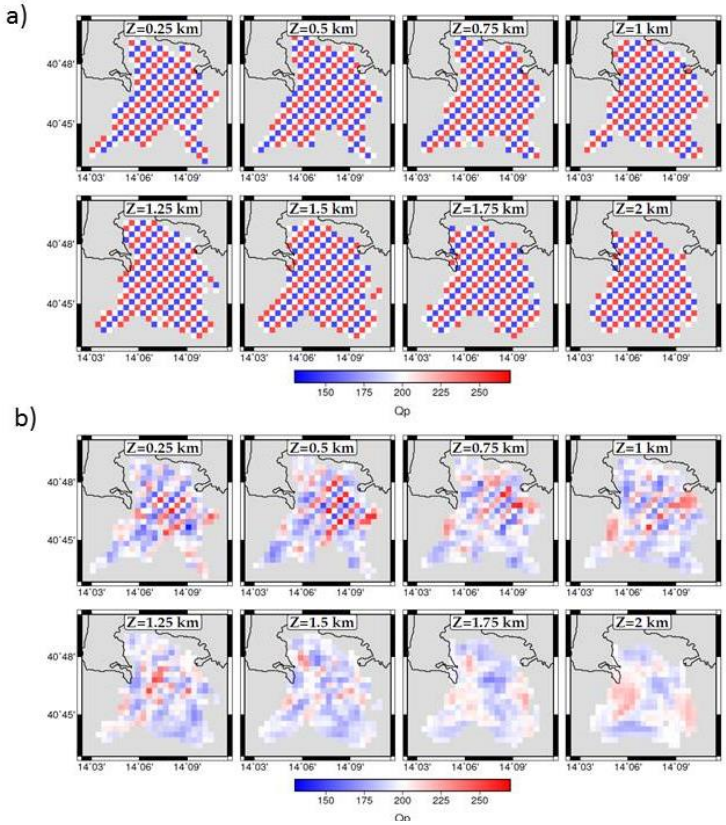

Figure 5.23 a) *Synthetic pattern of the checkerboard test.* ***b)*** *Recovered 3D attenuation pattern. The checkerboard structure is well resolved in the central part of the tomographic grid, up to 0.75 km.*

5.5 Discussion and interpretation of results

The results of attenuation tomography show some features that can be interpreted based on previous geophysical studies done in Campi Flegrei caldera. Furthermore, informations retrieved by core data have been used for our interpretation.

Based on our results, the shallow (0-1.25 km) off-shore part of Campi Flegrei caldera can be described as a prevalent low Q_P body, including also some high Q_P anomalies.

The inner, shallow part of the off-shore region of Campi Flegrei caldera is principally composed of deposits that have filled the caldera: water saturated volcanic (tuffs) and marine sediments (Dello Jacono et al., 2009). In particular, in the first meters, sediments are composed of mud, sandy silt rich in bioclasts and volcaniclasts, along with three tephra layers (Sacchi et al., 2014). From a geophysical point of view, the shallower part of inner area of Campi Flegrei caldera is characterized by low P-wave velocity values. Tomographic images obtained by us show low Q_P values in this region of the Pozzuoli Bay (Q_P about 30-40). It is in agreement with the variability of Q_P values retrieved from laboratory studies carried out on sandstones in different saturation conditions (Johnston et al., 1979; Winkler and Nur, 1979; Amalokwu et al., 2014).

Another prominent feature that has been recovered by the tomographic inversion is a pseudo-circular high Q_P anomaly at 0.75 km and 1 km depth. The ad-hoc resolution test which has been carried out confirms the reliability of this structure. From a geographical point of view, the retrieved anomaly is partially overlapped to the detected high P-wave velocity anomaly and positive gravimetric anomaly (figure 5.24). A good correlation between the geometries of the attenuation, velocity and density anomalies can be observed. The annular anomaly has been previously interpreted as the buried rim of the NYT caldera. From borehole data, the rim of the caldera is composed of compacted tuffs and lavas, with interbedded lava sequences. In our case, however, this arc-like structure seems to be located further south than the detected velocity and density ones.

The southern high Q_P anomalies detected at 0.5 km depth are located in correspondence of offshore volcanic edifices of Pentapalummo and Miseno banks (figure 5.26). Positive magnetic anomalies have been found in the proximity of all offshore volcanoes of Campi Flegrei. Milia et al. (2010), from a seismic stratigraphic analysis of submarine volcanic field, interpreted these magnetic anomalies in terms of cooled lava bodies. It may justify also the presence of high Q_P anomalies. In any case, the whole Pozzuoli Bay is characterized by lava intrusions, also at shallow depths (Mirabile et al., 1989). These may justify the detection of high Q_P bodies.

Finally, a high Q_P anomaly has been imaged north-west of Capo Miseno. The reliability of this feature has been assessed by means of a proper syntethic test. This anomaly is

located close to a zone of low Vp/Vs imaged by Chiarabba and Moretti (2006) (figure 5.25). Furthermore, the same authors, detected a low Vp value in the same region at which a high Q_P anomalous body has been retrieved by us. Hansen et al. (2004) interpreted the combination of these factors as the effect of the presence of a trapped CO_2. As a matter of fact, laboratory experiments have shown that for values of pressure lower than the pressure of saturation, the presence of gas can lead both to a decrease of P-wave velocity and of P-wave attenuation (Ito et al., 1979). This may be a possible physical interpretation of the high Q_P anomaly located at 1 km depth. Actually, an area very rich in fumaroles has been identified in De Bonitatibus et al. (1970) and it is located close to the detected low attenuation body. No precise knowledge of the chemical composition of the off-shore fumaroles is available. On the other hand, fumaroles characterized by H_20, H_2S and also CO_2 are present at Solfatara.

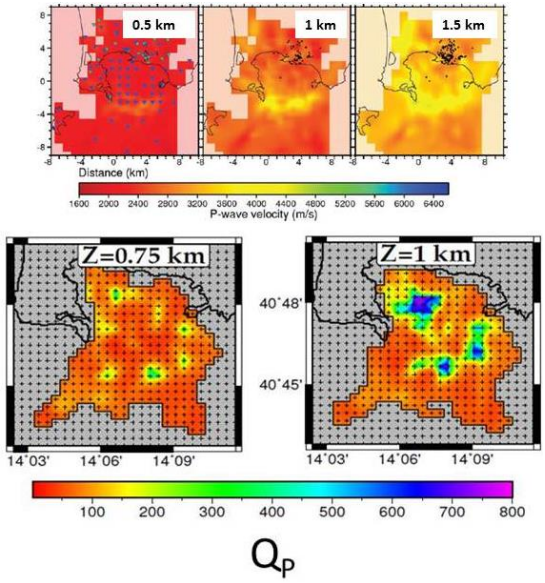

Figure 5.24. First row: *Battaglia et al. (2008) P-wave velocity map (modified after Battaglia et al. 2008).* ***Second row:*** *Attenuation tomography maps obtained by us.*

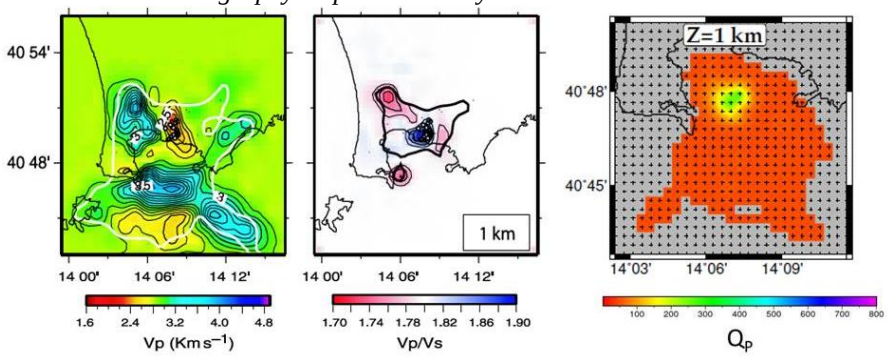

Figure 5.25. Left Panel: *P-wave velocity tomography map at 1 km depth (after Chiarabba and Moretti, 2006).* ***Central panel:*** *Vp/Vs tomography map at 1 km depth (after Chiarabba and Moretti, 2006).* ***Right panel:*** *Recovered attenuation image relative to the fixed geometry test 3).*

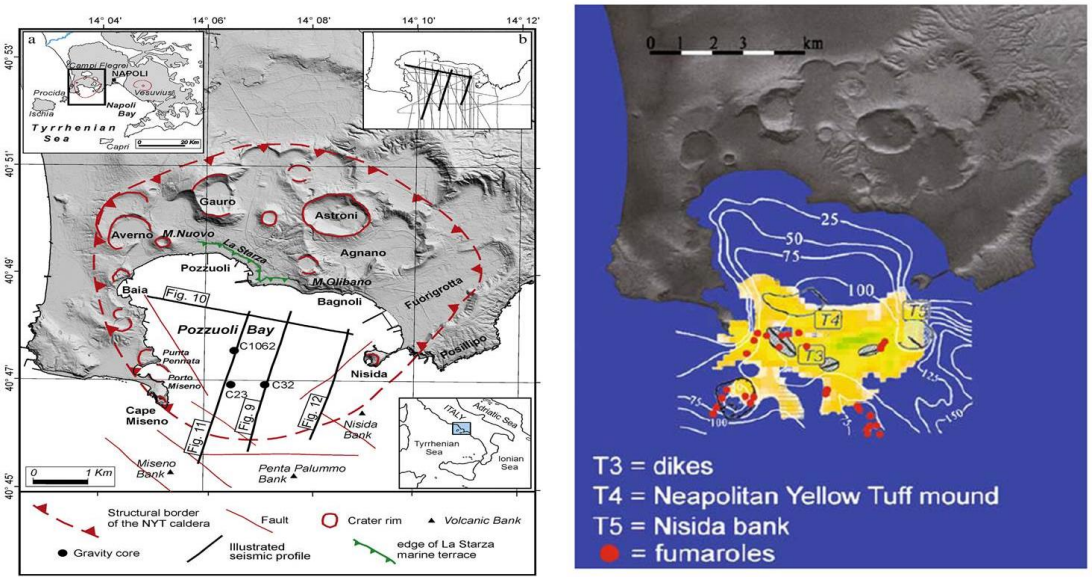

Figure 5.26 Left: *Schematic map of Campi Flegrei caldera, with indicated Miseno and Pentapalummo Banks in the southern part of the image (after Sacchi et al., 2014).* ***Right:*** *Positions of the fumaroles and of the dikes, correlated with the positive high Vp and high density anomalies (from dello Jacono, 2009).*

CONCLUSIONS

The aim of this PhD thesis has been to face the issue of achieving an attenuation image in volcanic areas. To this purpose, the Campi Flegrei volcanic field has been used as a testing region of the method, in order to retrieve a three dimensional Q_P map of the off-shore part of the area. The shallow part (up to 1.5 km depth) of the propagation medium has been investigated. This analysis has been performed by interpreting data recorded during the SERAPIS active seismic experiment, which was carried out on September, 2001 in the gulf of Naples and in the Bay of Pozzuoli.

The work has been developed in two different sections:

1) Elaboration of a strategy for data analysis;
2) Elaboration of an inversion strategy of measured data.

The first section of the thesis has consisted principally in testing the applicability of spectral ratio method to an active seismic dataset. In particular, it has been studied the sensitivity of the adopted measurement technique to three factors: 1) the velocity model; 2) the selected signal time window; 3) the frequency range over which the spectral ratio has to be computed and fitted. By means of synthetic tests we came to the following conclusions:

1) the more smooth the velocity model is, the more reliable the dt^* measurements provided by spectral ratio method are;
2) the time window to be selected in order to perform the necessary spectral analysis has to have comparable length to that of the seismic source. In that way, the signal contaminations relative to secondary arrivals are discarded from the spectrum computation.
3) The frequency range over which spectral ratio is computed and fitted can considerably affect the reliability of dt^* measurements.

Moreover, the measurements provided by spectral ratio method are greatly affected by the heterogeneities of the propagation medium. This problem has been overcome by adopting the so-called “deconvolution procedure” to suppress the contribution of the purely elastic Green’s function from the computed spectra. This procedure has been

tested on synthetic data and it has been verified that it greatly contributes to improve the reliability of dt^* measurements.

The spectral ratio method, after the application of deconvolution procedure, has been applied to seismic data of SERAPIS dataset. In that way a database of 14450 dt^* measurements has been obtained.

The second section has been developed in two phases. In the first one, the modification of the tomographic inversion code has been done. It consisted in a two-step change: first, the velocity tomography code has been adapted to the case of the attenuation. These modifications have been carried out by people of RISSC-Lab team. The testing of the code has been performed by me. After that, the code has been adapted in order to manage differential attenuation measurements. The synthetic tests have been carried out both with an optimal and with the real sources-receivers configuration. In that way, the reliability of the tomographic inversion code has been assessed.

Finally, the inversion of measured dataset has been run. To this purpose, it has been necessary a phase of study aimed to the optimal choice of parameterization, of regularization parameters and of the initial attenuation model. The best parameterization has been chosen by means of a statistical criterion (*AICc*). Concerning the initial model, a new approach has been followed. Actually, 200 1D attenuation models have been randomly generated within two reasonable 1D models. The final 3D P-wave attenuation model has been obtained by averaging 108 three dimensional models. These correspond to final models retrieved from the inversion of dt^* dataset using 1D initial random models. Only final models producing a RMS lower than a fixed threshold have been selected. Starting from these, the average three dimensional P-wave attenuation models has been computed.

The reliability of the final tomographic result has been assessed through a proper resolution study. It consisted of fixed geometry and checkerboard synthetic tests and of the study of DWS, model resolution matrix and spread function. All these tests have shown that the best resolution has been achieved in the central part of the tomographic model up to 1-1.25 km.

The main results retrieved from the inversion of dt^* measurements consists in the presence of a high Q_P anomalous body between 0.75 km and 1 km depth. It is well correlated with the annular anomaly detected by previous geophysical studies. It has been interpreted in the past as the buried rim of the NYT caldera, which is mainly

composed of consolidated lavas and tuffs with interbedded magmatic intrusions. Other high low attenuation bodies have been detected in the caldera. They have been interpreted either in terms of effects of cooled lava bodies or in terms of regions with pressured gas, in particular CO_2.

All the high Q_P bodies are immersed in a high attenuation layer. This is well correlated with low Vp and high Vp/Vs values and it has been interpreted as a layer of water saturated marine and volcanic sediments.

References

AGIP, 1987. Geologia e geofisica del Sistema geotermico dei Campi Flegrei. **Servizi Centrali per l'Esplorazione**, SERG-MMESG, San donato.

Akaike, 1974. A new look at the statistical model identification. **IEEE Trans. Autom. Control**, 6, 716-723.

Aki, K., and Richards., P.G., 1980. Quantitative seismology. **University Science Book**.

Amalokwu, K., Best, A. I., Sothcott, J., Chapman, M., Minshull, T. and Li, X., 2014. Water saturation effects on elastic wave attenuation in porous rocks with aligned fractures. **Geophys. J. Intern.**, 197, 2, 943-947, doi: 10.1093/gji/ggu076.

Amoruso, A., Crescentini, L. and Sabbetta, I., 2014. Paired deformation sources of the Campi Flegrei caldera (Italy) required by recent (1980-2010) deformation history, **J. Geophys. Res. Solid Earth**, 119, 858-879, doi: 10.1002/2013JB010392.

Aster, R. C. and Meyer, R. P., 1988. Three-dimensional velocity structure and hypocenter distribution in the Campi Flegrei Caldera, Italy. **Tectonophysics**, 149, 195-218.

Azimi, S. A., Kalinin, A. V., Kalinin, V. V., and Pivovorov, B. L., 1968. Impulse and transient characteristics of media with linear and quadratic absorption laws. **Izvestiya Physics of the Solid Earth**, 88-93.

Badri, M. and Mooney, H. M., 1987. Q measurements from compressional seismic waves in unconsolidated sediments. **Geophysics**, 52, 6, 772-784.

Barberi, F., Innocenti, F., Lirer, L., Munno, R., Pescatore, T. and Santacroce, R., 1978. The Campanian ignimbrite: a major prehistoric eruption in the Neapolitan area (Italy). **Bull. Volc.**, 41, 1-22.

Barberi, F., Cassano, E., La Torre, P. and Sbrana, A., 1991. Structural evolution of Phlegrean Fields in light of volcanological and geophysical data. **Journ. Volc. Geoth. Res.**, 92, 14,139-14,150.

Battaglia, M., Troise, C., Obrizzo, F., Pingue, F. and De Natale, G., 2006. Evidence for fluid migration as the source of deformation at Campi Flegrei caldera (Italy). **Geophys. Res. Lett.**, 33, L01307, doi: 10.1029/2005GL024904.

Battaglia, J., Zollo, A., Virieux, J., and Dello Jacono, D. 2008. Merging active and passive data sets in travel time tomography: The case study of Campi Flegrei caldera (southern Italy). **Geophysical prospecting**, 56, 555-573.

Beaducel, F. and De Natale, G., 2004. 3D modelling of Campi Flegrei ground deformations: role of Caldera boundary discontinuities. **Pure Appl. Geophys.**, 161, doi:10.1007/s00024-004-2507-4.

Benz, H. M., Chouet, B. A., Dawson, P. B., Lahar, J. C., Page, R. A. and Hole, J. 1996. Three dimensional P and S wave velocity structure of Redoubt Volcano, Alaska. **J. Geophys. Res.**, 101, B4, 8111-8128.

Berrino, G., Corrado, G., Luongo, G. and Toro, B., 1984. Ground deformation and gravity changes accompanying the 1982 Pozzuoli uplift. **Bull. Volc.**, 47, 187-200.

Berrino, G., Corrado, G. and Riccardi, U., 1998. Sea gravity data in the gulf of Naples: a contribution to delineating the structural pattern of the Vesuvian area. **Journ. Volc. Geoth. Res.**, 2008, 82, 139-150.

Berrino, G., Corrado, G., and Riccardi, U., 2008. Sea gravity data in the gulf of Naples: a contribution to delineating the structural pattern of the Phlegrean volcanic district. **Journ Volc. Geoth. Res.,** 175, 241-252.

Birch, F., 1942. Handbook of physical constants. **Geol. Soc. Am. Spec. Paper**, 36.

Bisrat, S. T., DeShon, H. R., Pesicek, J. and Thurber, C., 2013. High-resolution 3-D P wave attenuation structure of the New Madrid Seismic Zone using local earthquake tomography. **J. Geophys. Res.**, 119, doi:10.1002/2013JB010555.

Blair, D. P. and Spathis, A. T., 1982. Attenuation of explosion-generated pulse in Rock Masses. **J. Geophys. Res.**, 87, B5, 3885-3892.

Bouchon, M., 1979. Discrete wave-number representation of elastic wave field in three-space dimensions. **J. Geophys. Res.**, 84, 3609-3614.

Bodnar, R. J., Cannatelli, C., De Vivo, B., Lima, A., Belkin, H. E. and Milia, A., 2007. Quantitative model for magma degassing and ground deformation (bradyseism) at Campi Flegrei, Italy: Implications for future eruptions. **Geology**, 35, 9, 791-794, doi:10.1130/G23653A.1

Brenguier, F., Coutant, O., Baudon, H., Dorè, F. and Dietrich, M., 2006. High resolution seismic tomography of a Strombolian volcanic cone. **Geophys. Res. Lett.**, 33, L16314, doi:10.1029/2006GL026902.

Capuano, P. and Achauer, U., 2003. Gravity field modeling in the Vesuvius and Campanian area, in The TomoVes Seismic project: Looking inside Mt. Vesuvius [CD-ROM], edited by Zollo, A. et al., Coop. Univ. Editrice Napoletana, Naples.

Capuano, P., Zollo, A., Auger, E., Caielli, G., Chiarabba, C., Convertito, V., D'Auria, L., de Franco, R., Emolo, A., Judenherc, S., Lovisa, L., Makris, J., Michelini, A., Moretti, M., Priolo, E., Russo, G., Virieux, J., 2006. Campi Flegrei active seismic experiments waveforms compilation. **In "Geophysical Exploration of the Campi Flegrei (Southern Italy) Caldera's Interior: Data, Methods and Results"**.

Capuano, P., Russo, G., Civetta, L., Orsi, G., D'Antonio, M. and Moretti, R., 2013. The active portion of the Campi Flegrei caldera structure imaged by 3-D inversion of gravity data. **Geochemistry, Geophysics, Geosystems**, 14, 10, 4681-4697.

Cavanaugh, J. E., 1997. Unifying the derivations for the Akaike and corrected Akaike information criteria. **Statistics&Probability Letters**, 33, 2, 201-208.

Chiarabba, C. and Moretti, M., 2006. An insight into the unrest phenomena at the Campi Flegrei caldera from Vp and Vp/Vs tomography. **Terra Nova**, 18, 373-379, doi: 10.1111/j.1365-3121.2006.00701.x

Chiarabba, C., Piccinini, D. and De Gori, P., 2009. Velocity and attenuation tomography of the Umbria-Marche 1997 fault system: evidence of a fluid-governed seismic sequence. **Tectonophysics**, 476, 73-84, doi:10.1016/j.tecto.2009.04.004.

Chouet, B.,2003. Volcano Seismology. **Pure and Appl. Geophys**., 160, 739-788.

Civetta, L., Orsi, G., Pappalardo, L., Fisher, R.V., Heiken, G., Ort, M., 1997. Geochemical zoning, mingling, eruptive dynamics and depositional processes – The Campanian Ignimbrite, Campi Flegrei Caldera, Italy. **Journ. Volc. Geoth. Res.**, 75,183-219

Cormier, V. F., 1982. The effect of attenuation on seismic body waves. **Bull. Seism. Soc. Am.**, 72, 6, 169-200.

Coutant, O., 1989. Program of numerical simulation AXITRA. **Tech. Rept., LGIT**, Grenoble, France.

Clawson, S. R., Smith, R. B. and Benz. H. M., 1989. P wave attenuation of the Yellowstone Caldera from Three-Dimensional Inversion of Spectral decay using explosion source seismic data. **J. Geophys. Res**., 94,B6, 7205-7222.

De Bonitatibus, A., Latmiral, G., Latmiral, G., Mirabile, L., Palumbo, A., Sarpi, E., Scalera, A. Rilievi sismici per riflessione: struttuali, ecografici (fumarole) e batimetrici, nel golfo di Pozzuoli. **Boll. Soc. Natur. In Napoli**. 79, 97-113.

De Gori, P., Chiarabba, C. and Patanè, D., 2005. Q_P structure of Mount Etna: Constraints for the physics of the plumbing system. **J. Geophys. Res.**, 110, B05303, doi:10.1029/2003JB002875.

Della Vedova, B., Bellini, S., Pellis, G. and Squarci, P. 2001. Deep temperatures and surface heat flow distribution. In: Vai, G.B. and Martini, I. P. (eds). Anatomy of an orogeny: The Apennines and Adjacent Mediterranean Basin. Kluwer, Dordrecht, 65-67.

Dello Jacono, D., Zollo A., Vassallo, M., Vanorio, T. and Judenherc, S., 2009. Seismic images and rock properties of the very shallow structure of Campi Flegrei caldera (southern Italy). **Bull. Volc**., 71, 275-284, doi: 10.1007/s00445-008-0222-1.

de Lorenzo, S. , 1998. A model to study the Bias on Q estimates obtained by applying the rise time method to earthquake data. **Pure and Applied Geophysics**, 153, 419-438.

de Lorenzo, S., Zollo, A. and Mongelli, F., 2001. Source parameters and three-dimensional attenuation structure from the inversion of microearthquake pulse width data: Q_P imaging and inferences on the thermal state of Campi Flegrei caldera (Southern Italy). **J. Geophys. Res.**, 106, B8, 16,265-16,286.

de Lorenzo, S., Zollo, A., Zito, G., 2010. Source, attenuation, and site parameters of the 1997 Umbria-Marche seismic sequence from the inversion of P-wave spectra: a comparison between constant QP and frequency-dependent QP models. **J. Geophys. Res.**, 115,B090306, doi:10.1029/2009JB007004.

de Lorenzo, S., Romeo, A., Falco, L., Michele, M., Tallarico, A., 2014. A first look at the Gargano (southern Italy) seismicity as seen by the local scale OTRIONS seismic network. **Annals of Geophysics**, 57, 4, S0437, doi: 10.4401/ag-6594.

Del Pezzo, E., De Natale, G., Martini, M. and Zollo, A., 1987. Source parameters of microearthquakes at Phlegrean fields Flegrei (southern Italy) volcanic areas. **Phys. Earth Planet. Inter.**, 7, 25-42.

Del Pezzo, E., Simini, M., Ibanez, J. M., 1995. Separation of intrinsic and scattering Q for volcanic areas: a comparison between Etna and Campi Flegrei. **Journ. Volcan. Geoth. Res.**, 70, 3-4, 213-219.

De Martino, P., Tammaro, U., Obrizzo, F., 2014. GPS time series at Campi Flegrei caldera (2000-2013). **Annals of Geophysics**, 57, 2, S0213, doi:10.4401/ag-6431.

De Natale, G., Iannaccone, G., Martini, M. and Zollo, A., 1987. Seismic sources and attenuation properties at the Campi Flegrei Volcanic area. **Pure and Appl. Geophys.**, 125, 6, 883-917.

De Natale, G., Pingue, F., Allard, P. and Zollo, A., 1991. Geophysical and geochemical modelling of the 1982-1984 unrest phenomena at Campi Flegrei caldera (southern Italy). **Journ. Volcan. Geotherm. Res.,** 48, 199-222.

De Siena, L., Del Pezzo, E. and Bianco, F., 2010. Seismic attenuation imaging of Campi Flegrei: Evidence of gas reservoirs, hydrotermal basins and feeding systems. **J. Geophys. Res.**, 115, B09312, doi:10.1029/2009JB006938.

Di Renzo, V., Arienzo, I., Civetta, L., D'Antonio, M., Tonarini, S., Di Vito, M. A. and Orsi, G., 2011. The magmatic feeding system of the Campi Flegrei caldera: Architecture and temporal evolution. **Chemical geology**, 281, 227-241.

Di Vito, M. A., Isaia, R., Orsi, G., Southon, J., de Vita, S., D'Antonio, M., Pappalardo, L., Piochi, M., 1999. Volcanism and deformation since 12,000 years at the Campi Flegrei caldera (Italy). **Journ. Volcan. Geoth. Res.,** 91, 221-246.

Douglas, A., 1967. Joint epicenter determination. **Nature**, 215, 47-48.

Dvorak, J. J. and Berrino, G., 1991. Recent ground movements and seismic activity in Campi Flegrei, southern Italy: episodic growth of a resurgent dome. **J. Geophys. Res.,** 96, 2309-2323.

Dvorak, J. J. and Gasparini, P., 1991. History of earthquakes and vertical ground movement in Campi Flegrei caldera, southern Italy: Comparison of precursory event to the A.D. eruption of Monte Nuovo and activity since 1968. **Journ. Volc. Geoth. Res.,** 48, 77-92.

Eberhart-Phillips, D. 1986. Three-dimensional velocity structure in northern California coast ranges from inversion of local earthquake arrival times. **Bull. Seism. Soc. Am.**, 76, 4, 1025-1052.

Edwards, B., Rietbrock, A., Bommer, J. J. and Baptie, B., 2008. The acquisition of source, path, and site effects from microearthquake recordings using Q tomography: application to the United Kingdom. **Bull. Seism. Soc. Am.**, 98, 4, 1915-1935.

Evans, J. R. and Zucca, J. J., 1988. Active high-resolution seismic tomography of compressional wave velocity and attenuation structure at Medicine Lake Volcano, Northern California Cascade Range. **J. Geophys. Res**., 93, B12, 15016-15036.

Faccenna, C., Davy, P., Brun, J. P., Funiciello, R., Giardin, D., Mattei, M. and Nalpas, T., 1996. The dynamics of back-arc extension: an experimental approach to the openining of the Tyrrhenian Sea. **Geophys. J. Int.**, 126, 781-795.

Fedele, F., Giaccio, B., Isaia, R., Orsi, G., 2003. The Campanian Ignimbrite Eruption, Heinrich Event 4, and Paleolithic change in Europe: a high resolution investigation. In: Robock, A., Oppenheimer, C. (Eds.), **Volcanism and the Earth's Atmosphere:**

American Geophysical Union Geophysical Monograph, 139. American Geophysical Union, Washington, D.C., pp.301-325.

Fisher, R. V., Orsi, G., Ort, M. and Heiken, G., 1993. Mobility of a large volume pyroclastic flow emplacement of the Campanian Ignimbrite, Italy. **Journ. Volc. Geoth. Res.**, 56, 205-220.

Gaeta, F. S., Peluso, F., Arienzo, I., Castagnolo, D., De Natale, G., Milano, G., Albanese, C. and Mita, D. G., 2003. A physical appraisal of a new aspect of bradyseism: The miniuplifts. **J. Geophys. Res.**, 33, 2363, doi: 10.1029/2002JB001913.

Gilbert, F. and Backus, G. 1966. Propagator matrices in elastic wave and vibration problems. **Geophysics**, 31, 326-332.

Gladwin, M. T., and Stacey, F. D., 1974. Anelastic degradation of acoustic pulses in rock, **Phys. Earth. Planet. Inter.**, 8, 332-336.

Goldberg, D., Kan, T. K., and Castagna, J. P., 1984. Attenuation measurements from sonic log waveforms: 25th Ann. Logging Symp. Soc. Prof. Well Log Analysts, paper NN.

Got, J. L., Frechet, J. and Klein, F., 1994. Deep fault plane geometry inferred from multiplet relative relocation beneath the south flank of Kilauea. **J. Geophys. Res.**, 99, 11591-11621.

Hansen, S., Thurber, C. H., Mandernach, M., Haslinger, F. and Doran, C. 2004. Seismic velocity and attenuation structure of the east rift zone and south Flank of Kilauea Volcano, Hawaii. **Bull. Seism. Soc. Am.**, 94, 4, 1430-1440.

Hauksson, E., 2000. Crustal structure and seismicity distributions adjacent to the Pacific and North America plate boundary in southern California. **J. Geophys. Res.**, 105, 13,875-13,903.

Hobro, J. W. D., Singh, S. C. and Minshull, T. A., 2003. Three-dimensional tomographic inversion of combined reflection and refraction seismic traveltime data. **Geophys. J. Int.**, 152, 79-93.

Hole, J. A., Brocher, T. M., Klemperer, S. L., Parsons, T., Benz, H. M. and Furlong, K. P., 2000. Three-dimensional seismic velocity structure of the San Francisco Bay area. **J. Geophys. Res.**, 105, 13859-13874.

Ingram, J. D., Morris, C. F., MacKnight, E. E., and Parks, T. W., 1985. Direct phase determination of S-wave velocities from acoustic waveform logs: **Geophysics**, 50, 1746-1755.

Ito, H., DeVilbiss, J. and Nur, A., 1979.Compressional and shear waves in saturated rock during water-steam transition. **J. Geophys. Res.**, 84, 4731-4735.

Janert, K. P. 2009. Gnuplot in Action: Understanding data with Graphs, pp. 396, Manning Publications Co., Greenwich.

Johnston, D. H., Toksoz, M. N. and Timur, A. 1979. Attenuation of seismic waves in dry and saturated rocks: II. Mechanisms. **Geophysics**, 44, 4, 691-711.

Judenherc, S., and Zollo, A., 2004. The bay of Naples (southern Italy): Constraints on the volcanic structure inferred from a dense seismic survey. **J. Geophys. Res.**, 109, B10312.

Kennet, B. L. N., 1983. Seismic wave propagation in stratified media. **Cambridge University Press**, Cambridge.

Kissling, E., Husen, S. and Haslinger, 2001. Model parameterization in seismic tomography: a choice of consequence for the solution quality. **Phys. Earth. Planet. Int.**, 123, 89-101.

Kjartansson, E., 1979. Constant Q-wave propagation and attenuation. **J. Geophys. Res.**, 84, B9, 4737-4748.

Knopoff, L., 1964. Q. **Reviews of Geophysics**, 2, 625-660.

Latorre, D., Virieux, J., Monfret, T., Monteiller, V., Vanorio, T., Got, J. – L. and Lyon-Caen, H., 2004. A new seismic tomography of Aigon area (Gulf of Corinth-Greece) from a 1991 dataset. **Geophys. J. Int.**, 159, 1013-1031.

Le Meur, H., Virieux, J. and Podvin, P., 1997. Seismic tomography of the Gulf of Corinth: A comparison of methods. **Ann. Geophys**., 40, 1-25.

Lindsay, G., 1914. A study of the longitudinal vibration of waves, **Phys. Rev.**, 3, 397-438.

Marianelli, P., Sbrana, A. and Proto, M., 2006. Magma chamber of the Campi Flegrei supervolcano at the time of eruption of the Campanian Ignimbrite, **Geology**, 34, 937-940.

Mastrolorenzo, G., and Pappalardo, L., 2006. Magma degassing and crystallization processes during eruptions of high-risk Neapolitan-volcanoes: Evidence of common equilibrium rising processes in alkaline magmas. **Earth and Planet. Science Lett.**, 250, (1-2), 164-181, doi:10.1016/j.epsl.2006.07.040

Matheney, P. M., Nowack, R., 1995. Seismic attenuation values obtained from instantaneous-frequency matching and spectral ratios. **Geophys. J. Int.**, 123, 1-15.

McCann, C., Sothcott, J. and Assefa, S. B. 1997. Prediction of petrophysical properties from seismic quality factor measurements. Lovell, M. A. and Harvey, P. K. (eds), 1997. Developments in petrophysics, **Geological Society publication**, No. 122, pp. 121-130.

Menke, W., 1984. Geophysical data analysis: discrete inverse theory, **Academic Press, Inc.**

Michelini, A. and McEvilly, T. A., 1991. Seismological studies at Parkfield. I. Simultaneous inversion for velocity structure and hypocenters using cubic b-splines parameterization. **Bull. Seism. Soc. Am.**, 81, 2, 524-552.

Milia, A. and Torrente, M. M., 1997. Evoluzione tettonica della Penisola Sorrentina (margine peritirrenico campano). **Bollettino della Società Geologica Italiana**, 116, 487-502.

Milia, A., 2010. The stratigraphic signature of volcanism off Campi Flegrei (Bay of Naples, Italy). **In Groppelli, G. and Viereck-Goette, L., eds., Stratigraphy and Geology of Volcanic areas: Geological society of America, Special Paper 464**, pp. 157170, doi:10.1130/2010.2464(08).

Mirabile, L., Nicolich, R., Piermattei, R., Ranieri, G., 1989. Identificazione delle strutture tettonico-vulcaniche dell'area flegrea: sismica multicanale nel golfo di Pozzuoli. **ATTI VII CONVEGNO GNGTS 01/1989**; 2; 829-838.

Mitchell, B., 2010a. Prologue and invitation to participate in a forum on the frequency dependence of seismic Q. **Pure and Applied Geophysics**, 167, 1129; doi: 10.1007/s00024-010-0180-3.

Mitchell, B., 2010b. Epilogue. **Pure and Applied Geophysics**, 167, 1581; doi: 10.1007/s00024-010-0235-5.

Montagner, J. P. and Nataf, H. C., 1986.A simple method for inverting the azimuthal anisotropy of surface waves, **J. Geophys. Res.**, 91, 511-520.

Morozov, I., B., 2008. Geometrical attenuation, frequency dependence of Q, and the absorption band problem. **Geophys. J. International**, 175, 239-252.

Morozov, I. B., Zhang, C., Duenow, J. N., Morozova, E. A., and Smithson, S., 2008. Frequency dependence of regional coda Q: Part I. Numerical modeling and an example from Peaceful Nuclear Explosion. **Bull. Seism. Soc. Am**., 98, 2615-2628; doi: 10.1785/0120080037.

Morozov, I. B., 2009. Thirty years of confusion around "Scattering Q"?. **Seism. Res. Lett.**, 80, 1, 5-7.

Morozov, I. B., 2010. On the causes of frequency-dependent apparent seismological Q. **Pure and Applied Geophysics**, 167, 1131-1146.

Orsi, G., De Vita, S. and Di Vito, M., 1996. The restless, resurgent Campi Flegrei nested caldera (Italy): constraints on its evolution and configuration. **Journ. Volc. Geoth. Res.**, 74, 179-214.

Orsi, G., Petrazzuoli, S. M. and Wholetz, K., 1999. Mechanical and thermo-fluid behaviour during unrest at the Campi Flegrei caldera (Italy). **Journ. Volc. Geoth. Res.**, 91, 453-470.

Paige, C. C. and Saunders, M. A., 1982. LSQR: An algorithm for sparse linear equations and sparse least squares. Trans. Math. Software, 8, 43-71.

Pappalardo, L., Civetta, L., D'Antonio, M., Deino, A., Di Vito, M. A., Orsi, G., Carandente, A., de Vita, S., Isaia, R., Piochi, M., 1999. Chemical and Sr-isotopic evolution of the Phlegrean magmatic system before the Campanian Ignimbrite and the Neapolitan Yellow Tuff eruptions. **Journ. Volc. Geoth. Res**., 91, 141-166.

Peselnick, L., and Outerbridge, W. F., 1961. Internal friction in shear and shear modulus of Solenhofen limestone over a frequency range of 107 cycles per second. **J. Geophys. Res.**, 66, 581-588, 1961.

Podvin, P. and Lecomte, I., 1991. Finite difference computation of travel times in very contrasted velocity models: A massively parallel approach and its associated tools. **Geophys. J. Int.**, 105, 271-284.

Ponko, S. C. and Sanders, C. O., 1994. Inversion for P and S wave attenuation structure Long Valley caldera, California. **J. Geophys. Res.**, 99, B2, 2619-2635.

Rawlinson, N., Reading, A. M. and Kennet, B. L. N., 2006. Litospheric structure of Tasmania from a novel form of teleseismic tomography. **J. Geophys. Res.,** 111, B02301, doi:10.1029/2005JB/2005JB003803

Rawlinson, N., Pozgay, S., and Fishwick, S., 2010. Seismic tomography: a window into deep Earth. **Phys. Earth. Planet. Inter.**, 178, 101-135.

Reyners , M., Eberhart-Phillips, D. and Stuart, G., 1999. A three-dimensional image of shallow subduction: crustal structure of the Raukumura Peninsula, New Zealand. **Geophys. J. Int.**, 137, 873-890.

Rietbrock, A., 2001. P wave attenuation structure in the fault area of the 1995 Kobe earthquake. **J. Geophys. Res.**, 106, 4141-4154.

Rosi, M. and Sbrana, A., 1987. Phlegrean Fields, **Quad. Ric. Sci.**, 114, 175 pp.

Rosi, M., Vezzoli, L., Castelmenzano, A. and Greco, G., 1999. Plinian pumice fall deposit of the Campanian Ignimbrite eruption (Phlegrean Fields Italy). **Journ Volc. Geoth. Res.**, 91, 179-198.

Rowlands, D. P., White, R. S. and Haines, A. J., 2005. Seismic tomography of the Tongariro Volcanic Centre, New Zealand, **Geophys. J. Int.**, 163, 1180-1194.

Rubin, A., Gillard, D. and Got., J. L. 1998. A re-examination of seismicity associated with the January 1983 dike intrusion at Kilauea volcano, Hawaii. **J. Geophys. Res.**, 103, 10003-10015.

Sacchi, M., Pepe, M., Corradino, M., Insinga, D. D., Molisso, F. and Lubritto, C. 2014. The Neapolitan Yellow tuff caldera offshore the Campi Flegrei: Stratal architecture and kinematic reconstruction during the last 15 ky. **Marine Geology**, 354, 15-33.

Saccorotti, G., Petrosino, S., Bianco, F., Castellano, M., Galluzzo, D., La Rocca, M., Del Pezzo, E., Zaccarelli, L., Cusano, P., 2007. Seismicity associated with the 2004-2006 renewed ground uplift at Campi Flegrei Caldera, Italy. **Phys. Earth Planet. Inter.**, 165, 14-24.

Sams, M., and Goldberg, D., 1990. The validity of Q estimates from borehole data using spectral ratios. **Geophysics**, 55, 1, 97-101.

Sanders, C. O. and Nixon, L. D., 1995. S wave attenuation structure in Long Valley caldera, California, from three-component S-to-P amplitude ratio data. **J. Geophys. Res.**, 199, B7, 12,395-12,404.

Sanders, C. O., Ponko, S. C., Nixon, L. D. and Schwartz, E. A., 1995. Seismological evidence for magmatic and hydrothermal structure in Long Valley caldera from local earthquake attenuation and velocity tomography. **J. Geophys. Res.**, 100, B5, 8311-8326.

Satriano, C., Zollo, A., Capuano, P., Russo, G., Vanorio, T., Caielli, G., Lovisa, L. and Moretti, M., 2006. A 3D velocity model for earthquake location in Campi Flegrei area: application to the 1982-1984 uplift event. **In "Geophysical Exploration of Campi Flegrei (Southern Italy) Caldera's Interior: Data, Methods and Results".**

Shearer, P. M., 2009. Introduction to seismology, **Cambridge University Press.**

Shelly, D. R., Hill, D. P., Massin, F., Farrell, J., Smith, R. B., and Taira, T., 2013. A fluid-driven earthquake swarm on the margin of the Yellowstone caldera. **J. Geophys. Res. Solid Earth**, 118, 4872-4886. doi: 10.1002/jgrb.50362.

Sherburn, S., White, R. S. and Chadwick, M., 2006. Three-dimensional tomographic imaging of the Taranaki volcanoes, New Zealand. **Geophys. J. Int.**, 166, 957-969.

Spakman, W. and Nolet, G., 1988. Imaging algorithms, accuracy and resolution. **In Mathematical geophysics**, edited by N. Vlaar, pp. 155-187, Springer, New York.

Stein, S., and Wysession, M., 2003. An introduction to Seismology, Earthquakes and Earth Structure. **Blackwell Publishing**.

Taylor, S. R., Bonner, B. P. and Zandt, G., 1986. Attenuation and Scattering of Broadband P and S waves across North America. **J. Geophys. Res.**, 91, B7, 7309-7325.

Teng, T., 1968. Attenuation of body waves and the Q structure of the Mantle. **J. Geophys. Research**, 73, 6, 2195-2208.

Thurber, C. H., 1983. Earthquake locations and three-dimensional crustal structure in the Coyote Lake area, Central California. **J. Geophys. Res.**, 88, B10, 8226-8236.

Thurber, C. H., Ritsema, J. and Schubert, G., 2007. Theory and observations – Seismic tomography and Inverse methods. **In "Treatise of Geophysics"**, 2007, pp.323-360.

Todesco, M., Costa, A., Comastri, A., Colleoni, F., Spada, G. and Quareni, F., 2014. Vertical ground displacement at Campi Flegrei (Italy) in the fifth century: Rapid subsidence driven by pore pressure drop. **Geophys. Res. Lett.**, 41, 1471-1478. doi: 10.1002/2013GL059083.

Toomey, D. R. and Foulger, G. R., 1989. Tomographic inversion of Local earthquake data from the Hengill-Grensdalur Central Volcano Complex, Iceland. **J. Geophys. Res.**, 94, B12, 17,497-17,510.

Troise, C., De Natale, G., Pingue, F., Obrizzo, F., De Martino, P., Tammaro, U. and Boschi, E., 2007. Renewed ground uplift at Campi Flegrei caldera (Italy): New Insight on magmatic processes and forecast. **Geophys. Res. Lett.**, 33, L03301, doi: 10.1029/2006GL028545.

Tselentis, G. A., Paraskevopoulos, P., and Martakis, N., 2010. Intrinsic Qp seismic attenuation from the rise time of microearthquakes: a local scale application at Rio-Antirrio, Western Greece. **Geophysical prospecting**, 2010, 58, 845-859.

Tselentis, G. A., Martakis, N., Paraskevopoulos, P., and Lois, A., 2011. High resolution passive seismic tomography for 3D velocity, Poisson's ratio n, and P-wave quality QP in the Delvia hydrocarbon field, southern Albania. **Geophysics,** 76, 3, B89-B112.

Tusa, G., Brancato, A. and Gresta, S. 2006a. Source parameters of microearthquakes in Southeastern Sicily, Italy. **Bull. Seism. Soc. Am.**, 96, 3, 968-983, doi:10.1785/0120050071.

Tusa, G., Brancato, A., Gresta, S. and Malone, S. D. 2006b. Source parameters of microearthquakes at Mount St. Helens (USA). **Geophys. J. Int**, 166, 1193-1223, doi:10.1111/j.1365-246X.2006.03025.x

Udias, A., 1999. Principles of Seismology, **Cambridge University Press**.

Vanorio, T., Virieux, J., Capuano, P. and Russo, G., 2005. Three-dimensional seismic tomography from P wave and S wave microearthquake travel times and rock physics characterization of the Campi Flegrei caldera, **J. Geophys. Res.**, 110, B03201, doi:10.1029/2004JB003102.

Waldhauser, F., Ellsworth, W. L. and Cole, A., 1999. Slip parallel seismic lineations on the northern Hayward fault, California. **Geophys. Res. Lett.**, 26, 3525-3528.

Waldhauser, F. and Ellsworth, W. L., 2000. A double difference earthquake location algorithm: Method and Application to the Northern Hayward Fault, California. **Bull. Seism. Soc. Am.**, 90, 6, 1353-1368.

White, R. E., 1992. The accuracy of estimating Q from seismic data, **Geophysics**, 57,1508-1511.

Winker, K. W. and Nur, A., 1979. Pore fluids and seismic attenuation in rocks. **Geophys. Res. Lett.**, 6, 1, 1-4.

Wittlinger, G., Haessler, H., and Granet, M., 1983. Three-dimensional inversion of Q_P from low magnitude earthquakes analysis. **Annales Geophysicae**, 1, 6, 427-438.

Wohletz, K., Civetta, L. and Orsi, G., 1999. Thermal evolution of the Phlegrean magmatic system. **Journ. Volcan. Geoth. Res.,** 91, 381-414.

Xie, J., and Fehler, M., 2009. Comments on "Thirty years of confusion around scattering Q" by I.B. Morozov, **Seism. Res. Lett.**, 80, 646-647.

Xie, J. 2010. Can we improve estimates of seismological Q using a new geometrical spreading model? **Pure Appl. Geophys.**, 167, 1147-1162; doi: 10.1007/s00024-010-0188-8.

Yang, X. 2002. A numerical investigation of L_g geometric spreading, **Bull. Seism. Soc. Am.**, 92, 3067-3079.

Yang, X., Lay, T., Xie, X.-B and Thorne, M. S., 2007. Geometric spreading of P_n and S_n in a spherical Earth model, **Bull. Seism. Soc. Am.**, 97, 2053-2065, doi:10.1785/0120070031.

Yoshimitsu, N., Kawakata, H., Yamamoto, A., Ogasarawa, H. and Iio, Y., 2012. Temporal changes in attenuation of S waves through a fault zone in a South African gold mine. **Geophys. J. Int.**, 191, 1317-1324.

Zamora, M., Sartoris, G. and Chelini, W., 1994. Laboratory measurements of ultrasonic wave velocities in rocks from the Campi Flegrei volcanic system and their relation to other field data. **J. Geophys. Res.**, 99, B7, 553-561.

Zemanek, J. Jr., and Rudnick, I., 1961. Attenuation and dispersion of elastic waves in a cylindrical bar. **J. Acoust. Soc. Am.**, 33, 1283-1288, 1961.

Zhang, H. and Thurber, C. H., 2003. Double difference tomography: the method and its application to the Hayward fault, California. **Bull. Seism. Soc. Am.**, 93, 1875-1889.

Zhang, H. and Thurber, C. H., 2005. Adaptive mesh seismic tomography seismic tomography based on tetrahedral and Voronoi diagrams: Application to Parkfield, California. **J. Geophys. Res.**, 110, B04303, doi: doi:10.1029/2004JB003186.

Zhang, H., Thurber, C. H., Shelly, D., Ide, S., Beroza, G. and Hasegawa, A. 2004. High resolution subducting slab structure beneath Northern Honshu, Japan, revealed by double-difference tomography. **Geology**, 32, 361-364.

Zollo, A., and de Lorenzo, S., 2001. Source parameters and three-dimensional attenuation structure from the inversion of microearthquake pulse width data: Method and synthetic tests. **J. Geophys. Res.**, 106, B8, 16827-16306.

Zollo, A., Judenherc, S., Auger, E., D'Auria, L., Virieux, J., Capuano, P., Chiarabba, C., de Franco, R., Makris, J., Michelini, A. and Musacchio, G., 2003. Evidence for the buried rim of the Campi Flegrei caldera from 3-d active seismic imaging. **Geophys. Res. Lett.**, 30, 19, 2002, doi:10.1029/2003GL018173.

Zollo, A., Maerklin, N., Vassallo, M., Dello Jacono, D., Virieux, J. And Gasparini, P., 2008. Seismic reflections reveal a massive melt layer feeding Campi Flegrei caldera. **Geophys. Res. Lett.**, 35, L12306, doi:10.1029/2008GL034242.

Zollo, A., and Emolo, A., 2010. Terremoti ed onde. Metodi e pratiche della sismologia moderna. **Liguori Editore**.

Zollo, A., Orefice, A., and Convertito, V., 2014. Source parameters scaling and radiation efficiency of microearthquakes along the Irpinia fault zone in Southern Appennines, Italy. **J. Geophys. Res.**, 119, 3256–3275, doi:10.1002/2013JB010116.

Zucca, J. J., Hutchings, L. J. and Kasameyer, P. W., 1994. Seismic velocity and attenuation structure of the Geysers geothermal field, California. **Geothermics**, 23, 2, 111-126.

RINGRAZIAMENTI

Alla fine di quello che per me è stato soprattutto un percorso di crescita piuttosto che un percorso di studi è doveroso per me citare e ringraziare i tanti compagni che ho incontrato e che hanno condiviso con me l'intero o buona parte di questo viaggio.

Primo fra tutti, grazie a Salvatore de Lorenzo, per un motivo semplice: senza il suo incoraggiamento, probabilmente non avrei intrapreso questa esperienza, la più impegnativa ma anche la più stimolante della mia vita. Grazie per tutte le conoscenze che mi ha trasmesso in tutti questi anni, e grazie per aver compreso le difficoltà che ho avuto all'inizio del dottorato e durante, provando a darmi serenità. Grazie per avermi sostenuto nei momenti più duri, fra i quali l'agosto 2013…mai avrei sognato nella mia vita di essere all'università il 19 di agosto.

Grazie al prof. Zollo, per avermi permesso, in quanto responsabile del RISSC-Lab, di vivere questi tre anni in un gruppo di ricerca sismologica di assoluto valore.

Grazie al dott. Russo, per la sua pazienza, la sua enorme disponibilità nello spiegarmi cose che magari per un fisico sono banali, ma non necessariamente lo sono per un laureato in Geologia. Grazie per non avermi mai fatto sentire inadeguato di fronte ai problemi affrontati in questi anni. E' la persona arrivata dopo un anno di cammino e fondamentale solo io so quanto per arrivare a questo punto.

Grazie a tutti i membri del RISSC-Lab. Un grazie va a ciascuno abbia frequentato per un periodo più o meno lungo quelle stanze: nel caso di un dottorando fuori sede, le persone che abitano gli spazi nei quali si passano gran parte delle ore della giornata, inevitabilmente sono destinate a diventare un punto di riferimento. Un grazie particolare va ad una serie di persone:

grazie a Gaetano, per la passione incredibile che ha per quello che fa, che traspare in ogni sorriso con il quale affronta la giornata;

grazie a Sonia, perché apprezzai tantissimo la chiacchierata di accoglienza il secondo giorno a Napoli: può essere stata una cosa formale, ma per me fu molto importante;

grazie ad Ortensia, perché è stata in un certo senso la prima ad inserirmi nel laboratorio e per essere stato un riferimento tomografico fondamentale in questi tre anni;

grazie ad Antonella, per avermi iniziato a quel linguaggio perverso che è Bash e per il suo buongiorno sorridente all'inizio di ogni giornata;

grazie a Nitin, per le chiacchierate in inglese e perché l'ho sempre percepito come una persona molto vicina al mio percorso;
grazie a Claudio, per la sua incredibile simpatia senza la quale le pause pranzo non sarebbero le stesse;
grazie a Luca, riferimento informatico imprescindibile;
grazie a Sergio perché, in un laboratorio generalmente caratterizzato da ritmi frenetici come è il RISSC, è stata una persona fondamentale con il suo equilibrio, la sua calma, compostezza e serenità;
grazie a Simona, per la sua determinazione, la sua passione, che sono state inevitabilmente da stimolo in questi anni; grazie perché è importante sapere che a qualsiasi ora tu arrivi, qualcuno in laboratorio c'è gia; grazie per la vicinanza negli ultimi tempi e per aver letto e corretto, dall' I-Phone, la mia tesi;
grazie a Guido, perché avere un geologo come me in un ambiente di soli fisici è stato sentirsi come a casa; grazie per le tante discussioni fino a tardo pomeriggio, anche relative ai dubbi sul presente e sul futuro;
grazie a Piero, per le sue insistenze, più o meno velate, ad aprirmi di più di quanto avessi fatto nei primi due anni;
grazie a Tonino: non credo di conoscere un almanacco calcistico vivente come lui. Roba da pazzi. Ed è consolante sapere che c'è qualcuno messo peggio di me ☺;
grazie a Marcello, alla sua spontaneità, simpatia, e disponibilità a condividere le sue conoscenze (di qualsiasi tipo) e mandarini e finocchi con altre persone;
grazie a Grazia, perché sopporta con grandissima dignità 6-7 ragazzi messi insieme in una stessa stanza e perché il suo buongiorno squillante porta positività in laboratorio;
grazie ad Alessandro, perché se a suo tempo ho capito qualcosa del corso di Metodi Inversi è anche merito suo;
grazie a Maddalena, compagna nei pomeriggi passati in laboratorio a Bari, che altrimenti sarebbero stati decisamente più noiosi.

Grazie al prof. Virieux che, nel corso del mio stage a Grenoble, mi ha dato lo stimolo ad andare a fondo alle problematiche di questa tesi di dottorato;
grazie ad Alessandro, la persona con la quale ho maggiormente condiviso i corsi a Bologna e che, inaspettatamente ritrovato a Grenoble, ha contribuito ad alleviare la solitudine di quel periodo.

Alla fine, ma non per ultime, le persone da sempre a me vicine.
Grazie a Leonardo e Marianna, per non avermi mai fatto pesare, più di quanto non sia pesato a me, l'aver dovuto inevitabilmente sacrificare il gruppo giovanissimi, ora giovani, di AC;
grazie a tutta la mia famiglia, compresi cugini e zii, e in particolare ad Antonio, il cui aiuto è stato a dir poco fondamentale per superare l'esame di Matematica;
grazie a mamma e babbo, vicini come mai, nonostante la distanza fisica. Il loro supporto nei momenti più difficili, e sono stati tanti, è stato importantissimo per tenere duro. Grazie per le sveglie delle 4,30 i lunedì mattina, per i legumi cucinati, per essere riusciti ad inventare le condizioni perché la lontananza da casa mi pesasse il meno possibile.
Grazie, infine, alle persone a cui è dedicata questa tesi, che mi hanno visto cominciare questa esperienza, ma che, perlomeno fisicamente, non mi hanno visto terminare. Sono sicuro che nei momenti duri di questi tre anni, se ne avessero avuto la possibilità, avrebbero sicuramente rinfrancato il mio animo con un "Ad Maiora", "Ricordati che sei un Serlenga" e con qualche sorriso affettuoso.